Rita Peixoto Lopes de Figueiredo

mSkinColorCalib – Computer vision based-system for color calibration of mobile acquired skin lesion images

Thesis submited to the University of Coimbra
for the degree of Master in Biomedical Engineering

September 2017

· U C ·

UNIVERSIDADE DE COIMBRA

FCTUC FACULDADE DE CIÊNCIAS
E TECNOLOGIA
UNIVERSIDADE DE COIMBRA

Rita Figueiredo

mSkinColorCalib – Computer vision-based system for color calibration of mobile-acquired skin lesion images

Thesis submitted to the
University of Coimbra for the degree of
Master in Biomedical Engineering

Supervisors:
Doctor Maria João M. Vasconcelos (Fraunhofer Portugal)
Prof. Dr. Nuno C. Ferreira (University of Coimbra)

Coimbra, 2017

This work was developped in collaboration with:

Fraunhofer Portugal

Faculty of Sciences and Technology

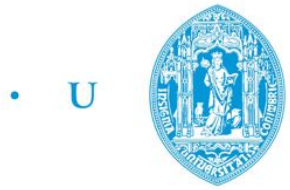

FCTUC FACULDADE DE CIÊNCIAS
E TECNOLOGIA
UNIVERSIDADE DE COIMBRA

Esta cópia da tese é fornecida na condição de que quem a consulta reconhece que os direitos de autor são pertença do autor da tese e que nenhuma citação ou informação obtida a partir dela pode ser publicada sem a referência apropriada.

This copy of the thesis has been supplied on condition that anyone who consults it is understood to recognize that its copyright rests with its author and that no quotation from the thesis and no information derived from it may be published without proper acknowledgement.

A ti, Filipe, que por seres tão bom foste chamado ao céu demasiado cedo...

Acknowledgments

E depois de um ano intenso parece que chegou a hora de agradecer a quem é devido, ou seja, a quem me aturou no meu pior.

Em primeiro lugar, e como não podia deixar de ser, fica um agradecimento à Doutora Maria Vasconcelos que foi incansável no decorrer deste ano. Para além de toda a sabedoria, de todos os conselhos dados a quem pouco ou nada pergunta (para mal dos meus pecados!), de todas as correções de todas as indicações... para além de tudo isto, também me soube acolher numa cidade que não era a minha, numa empresa desconhecida e que, acima de tudo, também soube que este ano não foi particularmente o mais fácil.

Ao Prof. Doutor Nuno deixo um agradecimento pela disponibilidade, por todas as burocracias da tese, informações de prazos e limites, correções de textos e de pósters nunca me faltou com nada.

Ao Luís Rosado e ao José Faria, investigadores da Fraunhofer, deixo um agradecimento por toda a ajuda no projeto, por toda a atenção e tempo que dispensaram a todas as minhas dúvidas.

À Laurinha, à Nini, à Minês, ao Marcelino, à minha mãe, à Mafaldinha e ao meu pai agradeço por terem servido de cobaias na minha tese. Aqui fica o vosso agradecimento prometido por terem tido tanto de sinais como de paciência.

Aos amigos que levo da Fraunhofer também deixo um agradecimento especial! Fazer uma tese sem companhia para almoço ou sem o café no bar da UPTEC não seria a mesma coisa. Não foi só a fazer a tese que aprendi, também levo muita bagagem nova da convivência convosco Marcos, Luís, Paulo e Tiago!

Aos meus amigos de sempre: Laura, Sofia, Inês, Bernardo, BP, Raul e Teles que embora não nos falemos como outrora (porque agora estou velha e uso palavras como outrora) sempre que estamos juntos sei que me conhecem como ninguém.

À Maria, à Mariana, à Rita, à Verónica, à Vila e à Xana agradeço por serem as pessoas genuínas que são que fizeram com que este percurso académico fosse mais divertido e mais fácil e por serem sempre as primeiras a oferecer ajuda quando me sabem stressada. Ao Rebelo agradeço o início atribulado com final feliz. À Minês agradeço isto tudo e muito mais. Obrigada por não me teres deixado fazer nada sozinha ao longo destes cinco anos: foste a companheira dos bons e dos maus momentos, habituaste-me (mal) a ter uma parceira para o que fosse e, com muita pena minha, essa parceria não seguiu para a tese! És a minha melhor definição de amiga.

Ao André, que neste último semestre presenciou o desespero em pessoa, nem sei se deva agradecer ou pedir desculpa! Obrigada por me teres sempre acalmado e tornado tudo divertido outra vez! Obrigada ainda ao teu avô, o maior cavalheiro que conheço, que me deu um tecto nos últimos seis meses e à Patrícia que sempre que me viu em baixo com a tese me fez acreditar que conseguia. À tua restante família fica também um agradecimento pelo privilégio que é conhecer quem te criou.

À mana Canina, "que faz o longe parecer perto", fica um agradecimento mais longínquo. Ainda que longe, quis sempre acompanhar todo o processo e esteve sempre pronta a dar conselhos sábios de quem passou pelo mesmo. És para mim um exemplo de vida. À Mafaldinha fica um agradecimento por todas as mudanças de humor que aturou, por todas as tabelas chatas que me ajudou a fazer e fica também o desejo que um dia possa ser eu a ajudar para que te tornes mestre.

Não podia deixar de acabar estes agradecimentos ao deixar um gigante OBRIGADA aos meus pais. E a vocês não consigo agradecer só por este ano. Que injusto era! Vocês que não só me possibilitaram tirar um curso, mas que mo deixaram fazer sempre com a diversão inerente a estudar em Coimbra. Vocês que me possibilitaram tirar um curso e ao mesmo tempo passear por esse mundo fora. Vocês que nunca me negaram nada. Obrigada por todos os cursos de computadores, por todos os anos de british, pelo curso, pelo mestrado no Porto em particular, pela pessoa que sou hoje no geral...

Resumo

Aplicações de teledermatologia móvel têm vindo a ganhar dimensão como uma ferramenta promissora no auxílio de médicos ao diagnóstico do cancro de pele. Estas aplicações dependem da extração de características da cor que são sensíveis tanto às condições de iluminação como ao dispositivo de aquisição da imagem.

Esta tese apresenta o desenvolvimento de um sistema de calibração da cor de imagens de lesões de pele capturadas com um dispositivo móvel. Através do uso de um gráfico de compensação de cores para estimar a relação entre as cores na imagem e as cores de referência, o sistema implementado reduz a influência do ambiente e da câmera usada.

A metodologia é dividida nas fases de pré-aquisição e de pós-aquisição. A primeira determina as configurações ótimas da câmara através da aquisição de imagens do gráfico de compensação de cores com diferentes configurações de câmara e calculando a diferença de cor média das amostras do gráfico. A última realiza a tarefa de calibração, que consiste em duas etapas: processo de criação de perfil e processo de aplicação do perfil. No processo de criação de perfil, uma imagem do gráfico de compensação de cores é adquirida e é estimada uma relação entre cores capturadas e cores de referência. Essa relação é incorporada num perfil de cor que é aplicado às imagens capturadas nas mesmas condições de luz que as do gráfico durante o processo de aplicação do perfil.

O desempenho deste sistema foi avaliado em dois conjuntos de experiências. O primeiro foi realizado em condições de luz conhecidas de cinco temperaturas de cores diferentes e com três dispositivos móveis diferentes, enquanto o segundo conjunto de experiências foi realizado sob condições de luz arbitrárias com os mesmos três dispositivos móveis. O desempenho foi avaliado com base na capacidade do sistema de aproximar as cores capturadas às cores de referência e, ainda, em termos da capacidade do sistema ser adaptado à calibração de imagens de lesões de pele.

Os resultados sugerem que o método implementado diminui as diferenças de cores

de imagens de lesões da pele, capturadas por diferentes dispositivos em diferentes ambientes. Para terminar esta dissertação, os resultados obtidos, bem como algumas considerações sobre possíveis melhorias e desenvolvimentos futuros, como a otimização do algoritmo implementado para reduzir o tempo de computação, são feitas.

Palavras-chave: *Calibração de cores, Teledermatologia móvel, Visão computacional, Dispositivos de câmera móvel, Aquisição de imagens com cor.*

Abstract

Mobile teledermatology (MT) applications have risen as a promising tool to assist healthcare professionals in the diagnosis of skin cancers. These applications rely on the extraction of color features, which are sensitive to both camera and lighting conditions.

This thesis introduces the development of a color calibration system targeted at skin lesion images captured with a mobile device. By using a color compensation chart to estimate the relationship between the colors in the image and the respective reference colors, the implemented system reduces the influence of not only the surrounding environment, as well as the one resulting from the camera used for such effect itself.

The methodology is based on a phased approach: the pre-acquisition stage and a post-acquisition stage. The former determines the optimal camera settings for image capture by acquiring images of the color compensation chart with different camera settings and calculating the average color difference of the patches; the latter accomplishes the calibration task itself which consists of two steps: the profile creation process and the profile application process. In the profile creation process an image of the color compensation chart is acquired, and a relationship between the captured colors and reference colors is estimated. This estimation is embedded in a color profile which is applied to images captured under the same light conditions as those of the chart during the profile application process.

The performance of this system was evaluated in two sets of experiments. The first set was performed under known light conditions of five different color temperatures and with three different mobile devices, whereas the second set of experiments took place under arbitrary light conditions with the same mobile devices. The performance was evaluated based on the system's ability to approximate captured colors to the reference colors and was also evaluated in its adaptability to calibrate skin lesion images.

The results obtained suggest that the implemented method can decrease the color

differences of skin lesion images captured by different devices under different environments. The conclusions achieved as well as some considerations on possible improvements and potential future developments - such as the optimization of the implemented algorithm in order to reduce the computation time - close this thesis dissertation.

Keywords: *Color calibration, Mobile Teledermatology, Computer vision, Mobile camera devices, Color image acquisition.*

List of Figures

1.1 Incidence and mortality of the twenty most frequent cancers in 2012 Europe . . . 2
1.2 Number of new skin cancers in Europe in 2020 . . . 2
1.3 Regional analysis of the existent vs. desirable human resources ratio of the Dermatology services in the Portuguese Healthcare System. . . . 3
1.4 Four lesions acquired by two different mobile devices. . . . 4
1.5 Gantt diagram. . . . 5

2.1 Visual differences between a melanoma, a nevomelanocytic nevi and a dysplastic nevi. . . . 8
2.2 Three different types of cutaneous melanomas. . . . 8
2.3 ABCDE rule for the classification of melanoma. . . . 9
2.4 Color spectrum seen by passing white light through a prism. . . . 12
2.5 Wavelengths comprising the visible range of the eletromagnetic spectrum. . . . 13
2.6 Simplified diagram of a cross section of the human eye. . . . 14
2.7 Primary and secondary colors of light and pigments. . . . 15
2.8 Chromacity diagram and color gamut. . . . 15
2.9 ColorChecker Classic. . . . 23
2.10 ColorChecker Digital SG. . . . 24

3.1 Methods' work-flow. . . . 30
3.2 Skin shades highlighted in red and periphery patches highlighted in yellow. . . . 31
3.3 Example of a non-uniformly illuminated skin lesion. . . . 31
3.4 Illustration of the suggested appearence-based method. . . . 32
3.5 Source image (a); result of the color quantization process for 25 (b) initial clusters; result of the color quantization process for 141 initial clusters(c). . . . 33

3.6 Result of the binarization process (a); result of the morphology operations (b);result of the regions removal by shape (c). 35
3.7 Patches grouped by area and coordinates 3.7a; Bounding Rectangle 3.7b; Final mask for source image 3.7c. 37
3.8 Query and source images 3.8a and keypoints detected for both 3.8b. . 39
3.9 Matches between source and query image 3.9a and color chart detection 3.9b. 40
3.11 Android applicaton main activity. 41
3.12 Android application settings activity (a) and pop-up menu for the AWB button (b). 42
3.13 Acquisition set-up. 44
3.14 Profile creation process. The image of the color compensation chart is captured. Then a four-step pre-correction is applied. Afterwards the tone response curves are estimated and the color space of the image is converted to the XYZ device independent color space. A relationship between the colors of the patches in the captured chart image and the internal reference colors is estimated 46
3.15 Patches used for brightness compensation. 47
3.16 Brightness map. 47
3.17 Gamma correction of lightness after correction of the white balance. . 48
3.18 Saturation enhancement of chroma after correction of white balance. . 48
3.19 Color patches used for TRC estimation. 49
3.20 Result of the TRC estimation process. 50
3.21 Profile application process. 53
3.22 mSkinColorCalib developed application. 54
3.23 Message shown to the user in profile creation process. 55
3.24 Dialog fragment shown to the user after profile creation. 56
3.25 Experiment 1's color chart acquisition set-up. 58

4.1 Two images acquired with different settings. 61
4.2 Charts acquired with the optimal settings for the different mobile devices. 62
4.3 Evaluation of Lesion 01 in Situation 1. 68
4.4 Evaluation of Lesion 02 in Situation 1 in L channel. 69
4.5 Calibration errors. 69
4.6 Evaluation of Lesions 01 and 02 in Situation 2 in L channel. 70
4.7 Example of the lesion segmentation performed. 71
4.8 Irregular skin surface of Lesion 13. 72

A.1 Location of the chromacity plane in XYZ color space. 95

List of Tables

2.1 Relation between color difference and human eye perception. 19
2.2 Performances obtained in Lee et al., 2006 25
2.3 Performances obtained in Lee et al., 2008 25

3.1 Routines available for the noise, AF and sharpness modes. 43
3.2 Tested settings for the 3 mobile devices. 57

4.1 Optimal settings for image acquisition. 62
4.2 Average of the color differences for the color charts obtained in 4.2.1. 63
4.3 Color charts stored in the profile creation process. 64
4.4 Average standard deviations obtained in Situation 3 for the 10 skin lesion images. 65
4.5 Lesion 01 before and after calibration for each mobile device and each color temperature. 66
4.6 Lesion 02 before and after calibration for each mobile device and each color temperature. 67
4.7 Evaluation of Lesion 01 in Situation 3. 70
4.8 Evaluation of Lesion 02 in Situation 3. 70
4.9 System performance under arbitrary light conditions. 72
4.10 Examples of charts acquired under arbitrary light conditions before and after calibration for each mobile phone device. 73
4.11 Average standard deviations obtained in Situation 1 for the 10 skin lesion images acquired under arbitrary light conditions. 73
4.12 Lesion 11 before and after calibration for each mobile device. 74
4.13 Lesion 12 before and after calibration for each mobile device. 75
4.14 Evaluation of Lesion 11 in Situation 1. 75
4.15 Evaluation of Lesion 12 in Situation 1. 75
4.16 Computation time across the mobile devices. 76

5.1 mSkinColorCalib color differences obtainedunder various color temperatures. 78
5.2 Performances obtained in Lee et al., 2006 and Lee et al., 2008 78
5.3 Performances obtained in Lee et al., 2006 78

B.1 ColorChecker Digital SG's colorimetric reference data. 99

C.1 Lesion 03. 102
C.2 Evaluation of Lesion 03 in Situation 3. 102
C.3 Lesion 04. 103
C.4 Evaluation of Lesion 04 in Situation 3. 103
C.5 Lesion 05. 104
C.6 Evaluation of Lesion 05 in Situation 3. 104
C.7 Lesion 06. 105
C.8 Evaluation of Lesion 06 in Situation 3. 105
C.9 Lesion 07. 106
C.10 Evaluation of Lesion 07 in Situation 3. 106
C.11 Lesion 08. 107
C.12 Evaluation of Lesion 08 in Situation 3. 107
C.13 Lesion 09. 108
C.14 Evaluation of Lesion 09 in Situation 3. 108
C.15 Lesion 09. 109
C.16 Evaluation of Lesion 10 in Situation 3. 109

D.1 Lesion 13. 111
D.2 Evaluation of Lesion 13 in Situation 1. 111
D.3 Lesion 14. 112
D.4 Evaluation of lesion 14 in Situation 1. 112
D.5 Lesion 15. 112
D.6 Evaluation of Lesion 15 in Situation 1. 113
D.7 Lesion 16. 113
D.8 Evaluation of Lesion 16 in Situation 1. 113
D.9 Lesion 17. 114
D.10 Evaluation of Lesion 17 in Situation 1. 114
D.11 Lesion 18. 115
D.12 Evaluation of Lesion 18 in Situation 1. 115
D.13 Lesion 19. 116
D.14 Evaluation of Lesion 19 in Situation 1. 116
D.15 Lesion 20. 117

D.16 Evaluation of Lesion 20 in Situation 1. 117

Bookmark name visible in a PDF viewer

Acronyms

AF Auto-Focus

CAT Chromatic Adaptation Transformation

CMS Color Management System

CIE *Commission Internationale de L'Éclairage*

ELM Epiluminescence Microscopy

EV Exposure Value

FCTUC Faculty of Sciences and Technology of the University of Coimbra

FED Fast Explicit Diffusion

ICT Information and Communication Technologies

ISO International Organizations for Standardization

IDE Integrated Development Environment

ICC International Color Consortium

JSON JavaScript Object Notation

MM Malignant Melanoma

MT Mobile Teledermatology

M-LDB Modified-Local Difference Binary

PCS Profile Connection Space

RANSAC Random Sample Consensus

SIFT Scale Invariant Feature Transform

SVD Singular Value Decomposition

SPD Spectral Power Distribution

SURF Speeded-Up Robust Features

TRC Tone Reproduction Curve

UV Ultraviolet

WB White Balance

Contents

List of Figures **xiii**

List of Tables **xvii**

1 Introduction **1**

1.1 Context . . . 1
1.2 Motivation . . . 1
1.3 Objectives . . . 4
1.4 Structure . . . 5

2 Theory **7**

2.1 Melanoma . . . 7
2.1.1 Classification Algorithms . . . 9
2.1.1.1 Non-Dermoscopic Methods . . . 9
2.1.1.2 Dermoscopic Methods . . . 10
2.2 Mobile Teledermatology . . . 10
2.3 Color . . . 12
2.3.1 Color spaces . . . 16
2.3.2 Acquisition parameters . . . 20
2.3.3 Color charts . . . 23
2.4 State-of-the-art . . . 24

3 Methods **29**

3.1 Color chart . . . 29
3.2 Color chart detection . . . 32
3.2.1 Appearance-based method . . . 32
3.2.2 Feature-based method . . . 37
3.3 Pre-acquisition processing . . . 41
3.4 Post-acquisition processing . . . 45

3.4.1 Profile creation . . . 45
3.4.1.1 Brightness compensation . . . 46
3.4.1.2 White balance correction . . . 47
3.4.1.3 Gamma correction . . . 47
3.4.1.4 Saturation Enhancement . . . 48
3.4.1.5 TRCs estimation . . . 49
3.4.1.6 Color space conversion . . . 51
3.4.1.7 Chromatic transformation . . . 52
3.4.2 Profile application . . . 53
3.5 Android implementation . . . 53
3.6 Test and evaluation . . . 56
3.6.1 Pre-acquisition processing . . . 56
3.6.2 Post-acquisition processing . . . 57

4 Results **61**
4.1 Pre-acquisition processing . . . 61
4.2 Post-acquisition processing . . . 62
4.2.1 Experiment 1 . . . 63
4.2.1.1 Ground truth comparison . . . 63
4.2.1.2 Skin lesions comparison . . . 65
4.2.2 Experiment 2 . . . 71
4.2.2.1 Ground truth comparison . . . 71
4.2.2.2 Skin lesions comparison . . . 73
4.2.3 Computation time . . . 75

5 Conclusions and Future Work **77**

Bibliography **81**

Appendices **91**
A Appendix I . . . 93
B Appendix II . . . 99
C Appendix III . . . 101
D Appendix IV . . . 111

1

Introduction

This chapter intends to provide a context to the problem that raised this dissertation. Motivation, main goals and objectives are described and the project's stakeholders are highlighted. Finally an explanation of this document's organization is presented.

1.1 Context

This document was developed on the scope of the Project discipline, during the academic year of 2016/2017. It corresponds to a dissertation to be submitted to the Faculty of Science and Technologies of the University of Coimbra (FCTUC) to obtain the Master Degree in Biomedical Engineering.

This project's origin was a result of a partnership between FCTUC and Fraunhofer Portugal, being the latter this theme's submitting entity. Fraunhofer Portugal is a Non-Profit Research Institution of Public Common Interest whose mission is to enhance people's living standards by offering them intuitive and useful technology solutions capable of facilitating their access to Information and Communication Technologies(ICT).

1.2 Motivation

Skin cancers represent nowadays the most common malignancies in the Caucasian population, with incidences that are reaching epidemic proportions [1]. According to the World Health Organization, the incidence of both non-melanoma and melanoma skin cancers has been increasing over the past decades. Currently, between 2 and 3 million non-melanoma skin cancers and 132,000 melanoma skin cancers are diagnosed globally each year [2].

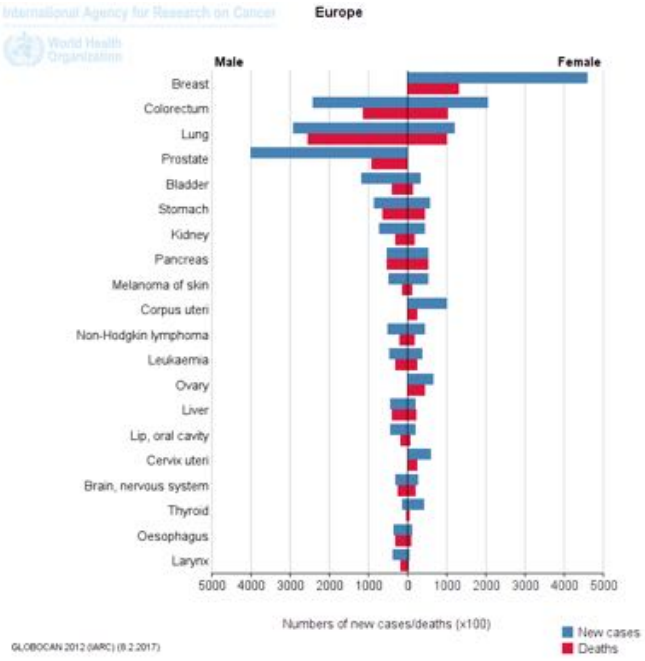

Figure 1.1: Incidence and mortality of the twenty most frequent cancers in 2012 Europe [3].

Malignant melanoma (MM) is one of the leading cancers among many white-skinned populations around the world. In 2012 melanoma was among the ten most common cancers in Europe, Figure 1.1. Moreover, the number of new skin cancers is expected to increase in 2020, for all ages and in both genders in European populations, Figure 1.2 [3]. This increase can be justified by a change of recreational behavior together with the increase in ultraviolet (UV) radiation [4]. As ozone levels are depleted, the atmosphere loses its protective filter function and more solar UV radiation reaches the Earth's surface. It is estimated a 10% decrease in ozone levels will result in an additional 300 000 non-melanoma and 4500 melanoma skin cancer cases [2].

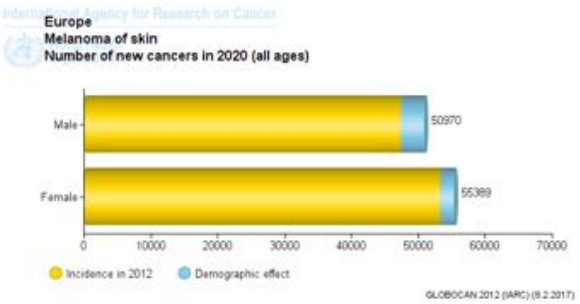

Figure 1.2: Number of new skin cancers in Europe in 2020 [3].

Furthermore, the Dermatology service in Portugal presented the largest response difficulties in 2015, with little more than 50% of the appointments performed, showing

also an inadequate distribution of dermatologists along the country (Figure 1.3) [5].

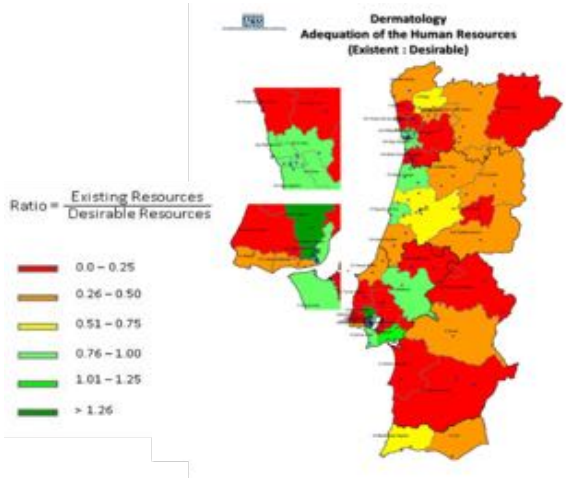

Figure 1.3: Regional analysis of the existent vs. desirable human resources ratio of the Dermatology services in the Portuguese Healthcare System [5].

These facts, plus the $8.1 billion a year cost for skin cancer treatment in the United States [6], show how critical it is for melanoma to be diagnosed early, before tumor invasion and life-threatening metastases have occurred [7].

Given these statistical indicators, there is a need for complementing existing technologies to have better screening methods of skin lesions [8]. Telemedicine is the rapid access to shared and remote medical expertise by ICT, no matter where the patient or relevant information is located [9]. This area's practicality has been reported in several studies with different applications [10–13].

Teledermatology refers to a telemedicine's subspeciality in the field of dermatology and one of the most common applications of telemedicine [14]. Professional teledermatology applications rely on high quality image acquisition devices and assume that the resulting image is optimal. However, when images are acquired with mobile devices they may contain several artifacts which could potentially impact image quality. Due to that, new challenges occur regarding preprocessing of macroscopic images acquired with mobile devices' cameras [8].

Accurate color features representation is an example of a difficult problem for digital imaging devices, because color images of unknown objects are captured under various unknown conditions such as illumination. Furthermore, color distributions of captured images are also dominated by characteristics of the imaging device [15]. Therefore, the challenge of creating a robust computer vision-based system that can perform color calibration of mobile-acquired images is of the utmost importance.

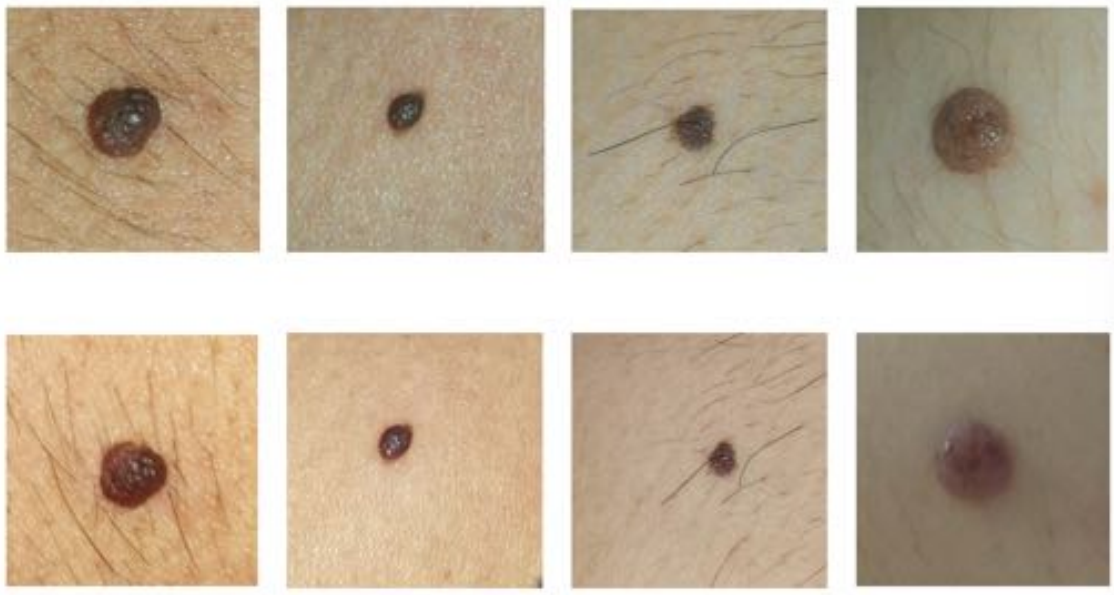

Figure 1.4: Same lesion acquired by different mobile devices (top /down rows) [16].

Figure 1.4 shows four skin lesions in each column acquired with two different mobile phone cameras, represented by the rows. The fact that the color differences of the same lesion acquired with different mobile phone devices are visible to the naked eye confirm the existence of a problem. These images were acquired at the Dermatology Department of Portuguese Institute of Oncology of Porto [16].

1.3 Objectives

The development of a computer-vision based system for color calibration of mobile acquired skin lesion images was this project's main goal.

In order to achieve such purpose, five tasks were considered in the beginning of this work. To a better understanding this project's schedule was performed through a Gantt diagram shown in Figure 1.5.

T1 - State of the art review regarding methodologies for color calibration (Section 2.4)

T2 - Thesis writing

T3 - Data acquisition

T4 - System development

T4.1 - Development of a methodology to acquire best camera settings (Section 3.3)

T4.2 - Development of a methodology for color calibration (Section 3.4)

T5 - Validation and Evaluation (Section 4)

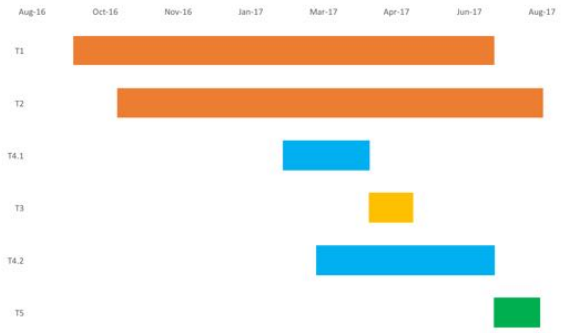

Figure 1.5: Gantt diagram.

1.4 Structure

This dissertation is structured in five main chapters.

Chapter 2: Theory provides a background on skin diseases and the algorithms to classify a melanoma. Moreover, an insight on mobile teledermatology is presented. The foundations of color are also reviewed in this chapter. Finally, a state-of-the-art chapter summarizes previous research on color calibration systems.

Chapter 3:Methods describes the methodologies used to perform the color calibration on the developed system.

Chapter 4: Results shows the performances achieved with the developed system.

Chapter 5: Conclusions and future work evaluates the results of the work, in confront with its objectives and foresees possible future work development.

2

Theory

This chapter is divided in four main sections. In Section 2.1 the theoretical basis of melanomas are explained and an overview of the melanoma classification algorithms is performed. Whereas Section 2.2 described the applications of mobile teledermatology. Section 2.3 reviews the color fundamentals, and explores the different color spaces (2.3.1), the acquisition parameters that have influence on color (2.3.2), and the different color charts available (2.3.3). Finally, Section 2.4 summarizes previous research developed on the color calibration of digital images.

2.1 Melanoma

Skin cancer is the uncontrolled growth of abnormal skin cells. It occurs when unrepaired DNA damage to skin cells triggers mutations, or genetic defects, that lead the skin cells to multiply rapidly [6].

Although pigmented lesions are among the most common findings in skin examinations, the challenge is to distinguish cutaneous melanomas, that account for the majority of deaths resulting from skin cancer, from the remainder, for example nevomelanocytic nevi or dysplastic nevi [7].

Nevomelanocytic nevi are benign proliferations of nevomelanocytes characterized by regularly shaped hyperpigmented macules or papules of a uniform color whereas dysplastic nevi are irregularly pigmented and shaped nevomelanocytic lesions. Figure 2.1a shows a superficial spreading melanoma, the most common type of melanoma; Figure 2.1b illustrates nevomelanocytic nevi and Figure 2.1c illustrates clinically atypical moles, i.e., a dysplastic nevi [7].

This distinction is a challenge because sometimes the minor differences in color and shape that distinguish a melanoma from a benign lesion can be difficult to recognize. Melanoma refers to an aggressive malignancy of the melanocytes, pigment-producing

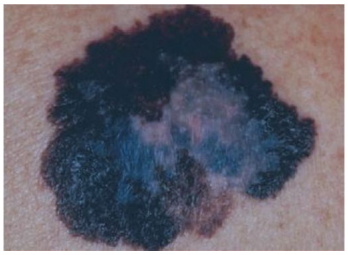

(a) Superficial spreading melanoma [7].

(b) Nevomelanocytic nevi [7].

(c) Dysplastic nevi (surrounded by the doctor) [7].

Figure 2.1: Visual differences between a melanoma, a nevomelanocytic nevi and a dysplastic nevi.

cells that originate from the neural crest and migrate to the skin, meninges, mucous membranes, upper esophagus, and eyes. Melanocytes in each of these locations have the potential for malignant transformation. There are four major types of cutaneous melanoma. The aforementioned superficial spreading melanoma, lentigo maligna melanoma shown in Figure 2.2a, acral lentiginous melanoma, Figure 2.2b and nodular melanoma, Figure 2.2c [7].

(a) Lentigo maligna melanoma [7].

(b) Acral lentiginous melanoma [7].

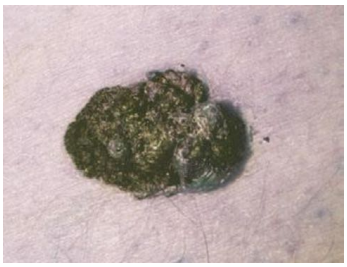

(c) Nodular melanoma [7].

Figure 2.2: Three different types of cutaneous melanomas.

Superficial spreading melanoma is the most common variant observed in the white population. Lentigo maligna melanoma usually is confined to chronically sun-damaged sites in older individuals. Acral lentiginous melanoma occurs on the palms, soles, nail beds, and mucous membranes. Although this type occurs in whites, it occurs most frequently (along with nodular melanoma) in blacks and East Asians. The fourth type, nodular melanoma, does not have a superficial growth phase and usually presents as a deeply invasive lesion that is capable of early metastasis. The strongest risk factors for melanoma are the presence of multiple benign or atypical nevi and a family or personal history of melanoma. Nevi have been referred to as precursor lesions because they can transform into melanomas [7].

2.1.1 Classification Algorithms

To identify a melanoma before tumor invasion and life-threatening metastases have occurred an early detection is essential. There are several classification algorithms for melanoma screening, grouped in two main methods: dermoscopic and non-dermoscopic methods [8].

2.1.1.1 Non-Dermoscopic Methods

The ABCD method was introduced in 1985 [17] and expanded to ABCDE in 2004 [18]. It represents an analytical method for the evaluation of melanocytic lesions created to alert both the general community and health care professionals to melanoma's features, namely: asymmetry (A), border irregularity (B), color variability (C), diameter greater than 6 mm (D) and evolution (E) [19]. Figure 2.3 clarifies the ABCDE algorithm.

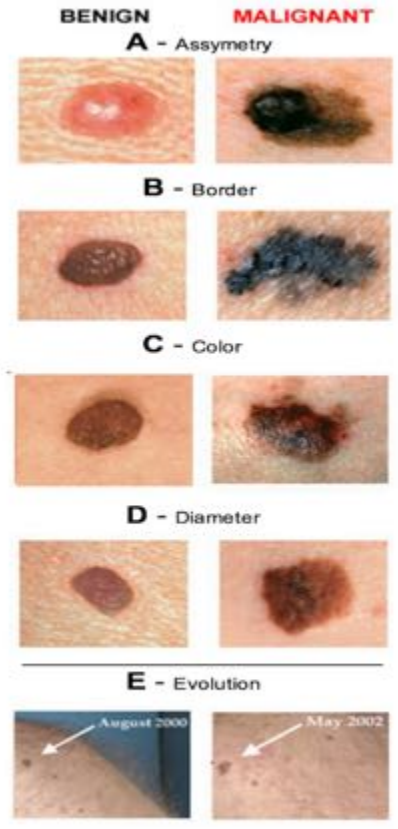

Figure 2.3: ABCDE rule for the classification of melanoma [6].

The ugly duck concept is another non-dermoscopic method introduced in 1998 by Grob et al. and was based on the observation that benign lesions from the same

individual tend to resemble one another whereas MM often deviates from this nevus pattern [20].

2.1.1.2 Dermoscopic Methods

Clinical diagnosis of skin lesions has been improved with the use of dermoscopy, a non-invasive technique that allows the in vivo evaluation of colors and microstructures of the epidermis, the dermo-epidermal junction and the papillary dermis not visible to the naked eye [21–23].

Dermoscopy is also referred as dermatoscopy, epiluminescence microscopy (ELM), incident light microscopy or skin surface microscopy [24]. This method requires a high quality lens for 10 to 14-times magnification and a lighting system, which enables the visualization of subsurface structures and patterns [8].

There are four main diagnosis methods from dermoscopic images: pattern analysis, Menzies method, 7-Point Checklist and ABCD rule, instead of the diameter in this case the D stands for differential structures. These methods were evaluated during the Consensus Net Meeting on Dermoscopy by experts from all over the world. A 2-step procedure was used to facilitate the diagnosis [25–27]:

- To decide whether the lesion is melanocytic or non-melanocytic.
- To decide whether the melanocytic lesion is benign, suspect, or malignant.

Despite the use of dermoscopy, the accuracy of expert dermatologists in diagnosing melanoma is still estimated to be about 75-84% [7, 28]. This issue highlights the demand for computer-aided diagnosis of melanoma, which provides quantitative and objective evaluation of the skin lesion, versus the subjective clinical assessment [8].

Moreover, for every classification method aforementioned color evaluation is for each method an important feature of analysis, reasserting the importance of color calibration in this context.

2.2 Mobile Teledermatology

The eHealth Action Plan 2012-2020 developed by the European Union aims at addressing ICT applied to health and healthcare systems stating they have the power to increase their efficiency, improve quality of life and unlock innovation in health markets [29].

With rising incidence rates of skin cancers, that can be explained by a combination of increased exposure to UV radiation, an increased longevity, ozone depletion, genetics and in some cases, immune suppression [30], arises the need to complement existing diagnostic techniques with teledermatology [8].

The term teledermatology was used for the first time by Perednia and Brown in 1995, to refer to the application of telecommunication technology to exchange medical data useful for skin disease diagnosis, treatment and prevention, when specialists and patients are separated in space or time. These authors carried a teledermatology project reaching high values of convergence between telematics examination and classical visits [31].

In recent years, virtual dermatological care has grown exponentially, making mobile teledermatology (MT) a common discipline in telemedicine, bringing dermatological healthcare to undeserved areas and populations in a cost-effective manner [32].

Several studies show the feasibility and reliability of the MT assessment. A study conducted in [33] shows that there is a good diagnostic agreement when comparing a teledermatology diagnosis and in-person clinical diagnosis or histopathology with traditional face-to-face consultations. Also, this technology provides patient access to dermatological services in an efficient and convenient manner, providers can effectively assess cases and provide recommendations within a reasonable time frame to the patient or referring provider [34].

Teledermatology has two established modalities: store-and-forward (asynchronous) and live interaction (synchronous). Store-and-forward teledermatology involves the transmission of digital images and clinical information to dermatologists for later review [8]. On the other hand, the live interaction modality consists of a real-time video interaction between the primary care provider and the teledermatologist [35].

Most MT programs have preferred the store-and-forward modality over the live interaction video due to its technological flexibility and lower cost of service delivery [36].

As indicated in a recent study, store-and-forward MT is cost effective in terms of significantly decreasing the need for in-person visits. The study also indicated that a reduction in the number of in-person visits allowed for shorter travel times for patients, decreased time away from work, and faster delivery of care [37]. Real-time interactive teledermatology has been found to be more costly than store-and-forward dermatology due to the need for expensive video-conference equipment and more consultation time [38].

However, despite the advantages of MT, concerns on self-provided photographs have been revealed given that several factors may directly impact the reliability of teledermatology including proper imaging [39].

Optimal acquisition and display of color medical images is critical to the diagnostic process as it impacts accuracy, discrimination, and consistency. As a matter of fact, teleclinicians emphasize the importance of accurate color in diagnosis [40].

Nevertheless, accurate color representation is a difficult problem for digital imaging devices, because color images of unknown objects are captured under various unknown conditions such as illuminations. Furthermore, color distributions of captured images are also dominated by characteristics of the imaging device [15].

Although some technical telemedicine guidelines for the standardization of acquisition and display devices do exist, they rarely incorporate color calibration issues [40] which is why, in this document, an attempt to solve this problem is presented.

2.3 Color

This section contains a description on the fundamentals of color. Afterwards, subsections concerning color spaces, color charts and acquisition parameters are presented.

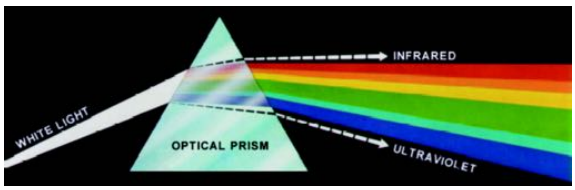

Figure 2.4: Color spectrum seen by passing white light through a prism [41].

In 1666, Sir Isaac Newton discovered that when a beam of sunlight passes through a glass prism, the emerging beam of light is not white but consists instead of a continuous spectrum of colors ranging from violet at one end to red at the other as depicted in Figure 2.4 [41].

Three basic quantities are used to describe the quality of a chromatic light source: brightness, intensity and luminance [42].

Brightness is defined by the International Color Consortium (ICC) or, more commonly, *Commission Internationale de L'Éclairage* (CIE), as the attribute of a visual sensation according to which an area appears to emit more or less light. It is, there-

fore, a subjective descriptor that embodies the achromatic notion of intensity and is one of the key factors in describing color sensation [42].

Radiant intensity refers to radiant power in a particular direction. Formally, it is the rate at which radiant energy is transferred, per unit solid angle. However, in physics, radiant intensity and radiance are integrated across a wide range of wavelengths. In color science, the interest lies in power only in the visible band. Radiant intensity, weighted by the spectral sensitivity associated with the brightness sensation of vision, is luminous intensity. It is expressed in units of candelas (cd) [42].

Due to the complexity of brightness perception, the CIE defined a more tractable quantity called luminance, which is luminous intensity per unit projected area. It is expressed in candelas per meter squared ($cd \cdot m^{-2}$). This quantity is radiant power weighted by a spectral sensitivity function that is characteristic of vision. Luminance, denoted Y, is proportional to power, in that sense it resembles intensity. However, the spectral composition of luminance is related to the brightness sensitivity of human vision. Luminance should be expressed in a unit such as candelas per square meter, the unit of luminous intensity in the International System of Units (SI) [43], but in practice it is often normalized to 1 or 100 units with respect to the luminance of a specified or implied white reference [42].

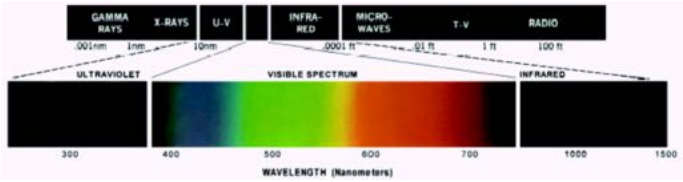

Figure 2.5: Wavelengths comprising the visible range of the electromagnetic spectrum [41].

Color is thus the perceptual result of light in the visible region of the spectrum, having a narrow brand of frequencies in the electromagnetic spectrum, its wavelengths ranging from 400 nm to 700 nm, incident upon the retina. Figure 2.5 represents the aforementioned wavelengths comprising the visible range of the eletromagnetic spectrum. Physical power, or radiance, is expressed in a spectral power distribution (SPD) [44].

SPD is a function of wavelength and describes the amount of optical radiation across part of a spectrum. SPD usually describes optical radiation emitted by a light source, but generally, it can be applied to describe optical radiation reflected by an object, or transmitted from a transparent/semi-transparent object [38]. SPD exists in the physical world, but colour exists only in the eye and the brain [44].

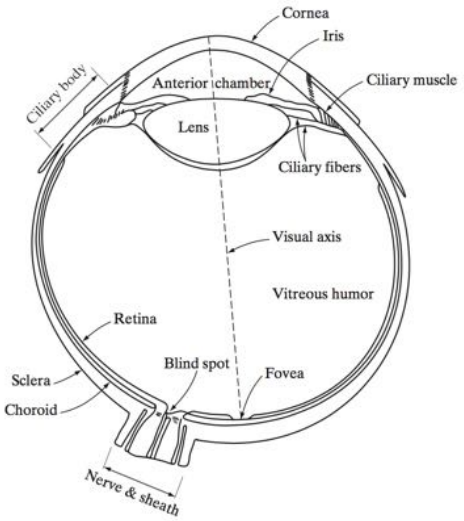

Figure 2.6: Simplified diagram of a cross section of the human eye [41].

Figure 2.6 shows a simplified horizontal cross section of the human eye. Three membranes enclose the eye: the cornea and sclera outer cover, the choroid and the retina.

The innermost membrane of the eye is the retina, which lines the inside of the wall's entire posterior portion. When the eye is properly focused, light from an object outside the eye is imaged on the retina. Pattern vision is afforded by the distribution of discrete light receptors over the surface of the retina. There are two classes of receptors: cones and rods. The former are located primarily in the central portion of the retina, called the fovea, and are highly sensitive to color. Rods serve to give a general, overall picture of the field of view. They are not involved in color vision and are sensitive to low levels of illumination [41].

The photoreceptor cone cells are divided into three principal sensing categories: cones sensitive to red light, to green light and to blue light. Because of these absorption characteristics of the human eyes, colors are seen as variable combinations of the primary colors Red (R), green (G) and blue (B) and these three numerical components are necessary to describe a colour, provided that appropriate spectral weighting functions are used [42].

The primary colors can be added to produce the secondary colors of light. Magenta appears as a combination of red plus blue. On the other hand, cyan is obtained by adding green plus blue, and finally yellow consists on red plus green [41]. Primary and secondary colors are depicted in Figure 2.7.

In 1931 the ICC has defined a chromacity diagram, a system to compute a triple

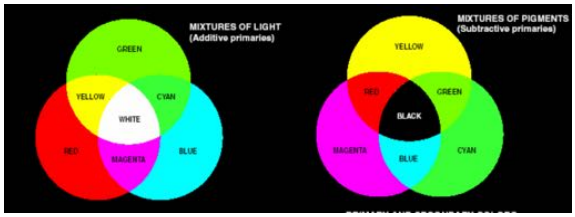

Figure 2.7: Primary and secondary colors of light and pigments [41].

of numerical components that can be considered the mathematical coordinates of a color space [42].

The diagram is illustrated in Figure 2.8a. The colors on the border are pure spectral powers. A straight line between any two points on the diagram shows all the colors that can be produced by mixing those colors. Different points on the line represent different mixtures of the two colors at the end points of the line. Any color inside the diagram can be made in different ways, but only the colors round the edge of the diagram are unique colors. Extending this idea to mixtures of 3 colors a triangle is obtained, called the gamut, presented in Figure 2.8b [41].

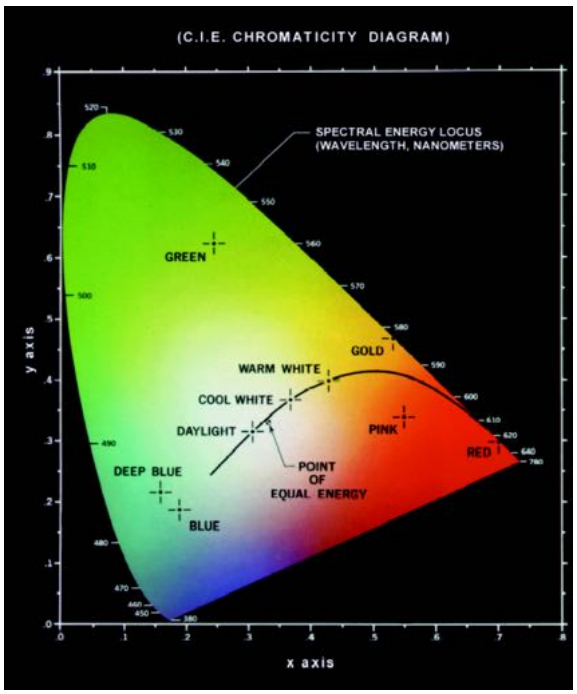

(a) Chromacity diagram [41].

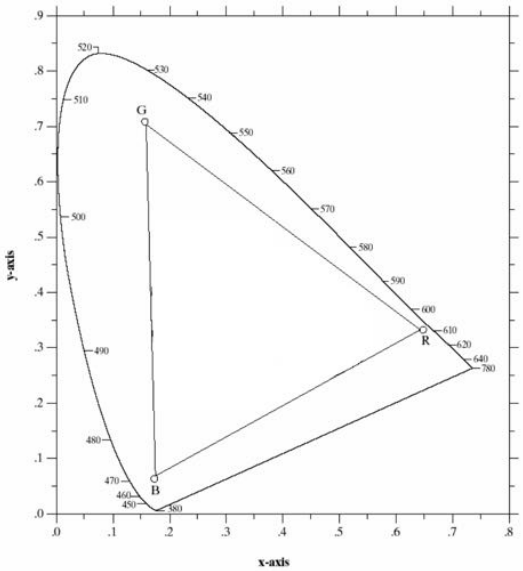

(b) Typical color gamut of color monitors (triangle) adapted from [41].

Figure 2.8: Chromacity diagram and color gamut.

The area inside the gamut shows all the colors that can be achieved from mixing the 3 colors in the corners. The edges of the gamut are the colors that result from mixing the two colors at the end of the line. Color displays such as TVs and

computer monitors use three different colors of pixel to generate all the other colors that can be displayed. The colors red, green and violet are in the corners of the chromacity diagram, so using these three colors covers the largest possible area of the chromacity diagram, but it still does not cover the entire diagram. Nevertheless, it is technically difficult to produce screens which generate pure spectral colors and real displays use red, green and blue pixel colors instead which are colors inside the chromacity diagram, covering an even smaller area of the diagram. For this reason, to fully specify the display there is a need to define the chromacity coordintes of the red, green and blue that it uses. Standardizing color is a difficult task, the color red on different monitors can be quite different. The point of equal energy is a mixture of red, green and blue – the color white [41].

Even though there are several color models, with different information contained in the three numbers that specify a color, there is no single color system that fits all needs of color users. The systems useful today for colour specification will be explained in the subsequent subsection [42].

2.3.1 Color spaces

Color spaces can dramatically influence the results of the processing, so the choice of an appropriate color space is an important decision. The knowledge of various color spaces can ease the choice of the appropriate color space [45].

The color spaces CIE RGB (Red-Green-Blue) and CIE XYZ (Y matches closely to luminance, while X and Z give color information) were the first mathematically defined color spaces. The former is a set of CIE color-matching curves based on many experiments with average observers and based on pure light sources at specific Red-Green-Blue wavelengths where the resulting spectral curves are called the CIE standard primaries [8]. The value of these three components is the sum of the respective sensitivity functions and the incoming light:

$$R(S) = \int \bar{r}(\lambda)S(\lambda)d\lambda \tag{2.1}$$

$$G(S) = \int \bar{g}(\lambda)S(\lambda)d\lambda \tag{2.2}$$

$$B(S) = \int \bar{b}(\lambda)S(\lambda)d\lambda \tag{2.3}$$

where S(λ) is the light spectrum, R(λ), G(λ) and B(λ) are the sensitivity functions for the R, G and B sensors respectively. This transformation from the spectral power distribution to a three-dimensional vector is a powerful compression technique with a compression ratio of more than 10:1 [44]. A side effect of this transformation is a loss of information which leads to the existence of so-called metamers. These are colours with different spectra but with same perceptual values [45].

From the above equations it can be observed that the RGB values depend on the specific sensitivity function of the capturing device, thus the RGB colour space is device-dependant color space. Printing and displaying devices work on an RGB fashion basis. And they also have their specific sensitivity functions which makes the term controlled environment even more difficult to achieve [45].

Even though the RGB colour space is the basic colour space it presents problems. The main disadvantage of the RGB colour space in applications with natural images is a high correlation between its components. Moreover, its psychological non-intuitivity is another problem because a human has problems with the visualization of a colour defined with the R, G and B attributes. Another problem is the perceptual non-uniformity, i.e., the low correlation between the perceived difference of two colours and the Euclidian distance in the RGB space [45].

On the other hand, the CIE XYZ is derived from CIE RGB, where XYZ are extrapolations of RGB created to avoid negative numbers, since the chromaticity would be outside the color triangle defined by the primary colors, and are called tristimulus values [8].

These values can describe any colour that can be subject to perception by an average human observer (the CIE 1931 standard colorimetric observer). These primaries are nonreal, i.e. they cannot be realized by actual colour stimuli. A very important attribute of the CIE XYZ color space is that it is device independent. Every color space that has a transformation from the CIE XYZ color space can also be regarded as being device independent. The CIE XYZ colour space is usually used as a reference colour space and is as such an intermediate device-independent colour space [45].

The coordinate systems CIE XYZ and CIE RGB are related to each other by linear equations. The linear transformation from CIE RGB to a new system CIE XYZ can be found in Appendix A.1.

However, when performinc color space conversions reference whites must be used consistently. Mismatched reference whites must be accounted using a chromatic

adaptation algorithm.

The ICC specification allows the use of different linear (matrix-based) chromatic adaptation transformations (CAT). Nevertheless, the use of different CATs will produce different results, which may be undesirable. Therefore, it is recommended that the linear Bradford CAT is used when there is no reason to use a different CAT. The linear Bradford CAT has been widely implemented in the digital imaging industry, with demonstrated excellent visual performance [46]. The conversion equations that account for the chromatic adaptation matrix for a linear CAT can be found in Appendix A.2.

In 1976 the CIE proposed two colour spaces (CIE Lab and CIE Luv) whose main goal was to provide a perceptually equal space [45]. L* represents the lightness of the color whereas a* and b* represent the color differences in terms of redness-greenness and yellowness-blueness, respectively. On the other hand, u* and v* also represent differences in the chromaticity coordinates, but are not associated to color names as a and b [8]. This means that the Euclidian distance between two colors in the CIELab/CIELuv colour space is strongly correlated with the human visual perception, To achieve this property there were two main constraints to take into account [45]:

- Chromatic adaptation;
- Non-linear visual response.

The main difference between the two colour spaces is in the chromatic adaptation model implemented. The CIE Lab colour space normalizes its values by the division with the white point while the CIELuv colour space normalizes its values by the subtraction of the white point. The transformations from CIE XYZ to CIE Luv and from CIE XYZ to CIE LAB can be found in Appendix A.3.

These color spaces are device independent, since they are based on the CIE system, however they are unintuitive. CIE L*u*v* and CIE L*a*b* are absolute color spaces, thus including more color information than other color spaces and even more than the human eye can perceive [44].

Color difference refers to numerical differences between color specifications. The perception of color differences in XYZ or RGB is highly non-uniform. The study of perceptual uniformity concerns numerical differences that correspond to color differences at the threshold of perceptibility, called just noticeable differences (JNDs) [42].

In 1976 the CIE recommended two color difference formulae to calculate the perceptually linear colour differences between two colours, based in the Euclidean distance as shown in the equations:

$$\Delta E^*_{ab} = \sqrt{(\Delta L^*)^2 + (\Delta a^*)^2 + (\Delta b^*)^2}$$
$$\Delta E^*_{uv} = \sqrt{(\Delta L^*)^2 + (\Delta u^*)^2 + (\Delta v^*)^2} \tag{2.4}$$

Even though there have been some improvements along the years in the color difference calculation, with the most recent being ΔE_{2000}, the most commonly used is still the ΔE_{ab} from 1976 provided in Equation 2.4 [47]. Moreover, the CIE provided Table 2.1 as a reference for understanding how the human eye perceives color difference.

Table 2.1: Relation between color difference and human eye perception [48].

ΔE	Perception
<= 1.0	Not perceptible by human eyes.
1 - 2	Perceptible through close observation.
2 - 10	Perceptible at a glance.
11 - 49	Colors are more similar than opposite.
100	Colors are exact opposite.

In 1976, Microsoft and Hewlett-Packard (HP) created a a standard color space, sRGB, for use within the Microsoft operating systems, HP products, the Internet, and all other interested vendors. The aim of this color space was to complement the color management strategies by enabling a method of handling color in the operating systems, device drivers and the Internet that utilized a simple and robust device independent color definition [48].

Other color spaces include HSL (Hue, Saturation and Lightness), HSI (Intensity)and HSV (Value) HSB which are linear transforms from RGB and are therefore device dependent and non–linear [42].

According to the CIE [48], hue is the attribute of a visual sensation according to which an area appears to be similar to one of the perceived colours, red, yellow, green and blue, or a combination of two of them. Roughly speaking, if the dominant wavelength of an SPD shifts, the hue of the associated color will shift. Saturation is the colourfulness of an area judged in proportion to its brightness. Saturation runs

from neutral grey through pastel to saturated colors. Roughly speaking, the more an SPD is concentrated at one wavelength, the more saturated will be the associated color [42].

The advantage of these systems lies in the intuitive manner of specifying color making them a good choice in user interfaces. Moreover, the small correlation between the three components also constitutes an advantage. Nevertheless, these color spaces are flawed with respect to the properties of color vision. Since perceptually-based systems like L*u*v* and L*a*b* are available, the use of these color spaces is discouraged by the ICC [42].

Different color spaces are better for different applications, since some colors are perceptually linear or just more intuitive to use [44].

2.3.2 Acquisition parameters

The acquisition of an image with a digital camera is a relevant aspect to color imaging. Conditions impacting color quality include lighting and camera settings, namely exposure, white balance and sharpness [40].

Exposure is the the amount of light per unit area of a camera's sensor. This amount is determined by three camera settings [49]:

- Aperture;
- ISO speed;
- shutter speed.

The challenge is to conjugate these settings in order to avoid both over and underexposure. The former consists of a washed-out image with detail loss due to an excessive light amount. The later will result in a dark image with no shadow detail [50].

Different combinations of the above three settings can achieve the same exposure. The problem lies in knowing which trade-offs to make, since each setting also influences other image properties. For example, aperture affects depth of field, shutter speed affects motion blur and ISO speed affects image noise [49].

Aperture's size adjustment controls the intensity of light passed by the lens. It is specified in terms of an f-value. The area of the opening increases as the f-value decreases. When the f-value halves, the light-collecting area quadruples [49].

Depth of field is the range of distance over which objects appear in sharp objects and is determined by the lenses' aperture. Lower f-values correlate with shallower depth of field [49].

Shutter speed consists in the precise amount of time the camera's sensor is opened to incoming light from the camera lens. A faster shutter speed means a shorter exposure time and this variable correlates exactly 1:1 with the amount of light entering the camera [49,50]. Shutter speed is a powerful tool for freezing, associated with a fast shutter speed, or exaggerating the appearance of motion, associated slow shutter speed [49].

ISO speed determines the sensitivity of a camera to the incoming light which is given as an International Organizations for Standardization (ISO) number. Similar to shutter speed, it also correlates 1:1 with the amount of light in the sensor and the higher the speed the more sensitive a camera is to light. However, it also increases the amount of digital noise present in your photo. Common ISO speeds include 100, 200, 400 and 800, although many cameras also permit lower or higher values [49].

White balance (WB) is the process of removing unrealistic color casts, so that objects which appear white in person are rendered white in your photo. Proper camera white balance has to take into account the color temperature of a light source, which refers to the relative warmth or coolness of white light. As opposed to our eyes, digital cameras have great difficulty with auto white balance (AWB) — and can create unsightly blue, orange, or even green color casts. One way to describe the color of a light source is by its color temperature. The color temperature scale is calibrated in degrees Kelvin(K) and ranges from the lower color temperatures of reddish light to the higher color temperatures of bluish light. Daylight contains proportionately more light toward the blue end of the spectrum. Incandescent light contains more toward the red end, thus daylight is described as cooler, on the other hand incandescent light is described as warmer [49,51]. Most digital cameras contain a variety of pre-set WBs with different color temperatures assumed as scene illumination [49].

Sharpness describes the clarity of detail in a photo and the two fundamental factors that contribute to the perceived sharpness of an image are acutance and resolution. Acutance describes how quickly image information transitions at an edge, and so high acutance results in sharp transitions and detail with clearly defined borders, whereas resolution accounts for the camera's ability to distinguish between closely spaced elements. The resolution is limited by the digital sensor. On the other hand, acutance depends on the lens. Images require both high acutance and resolution to be perceived as sharp. Thus, the main causes of an image not being sharp are

camera shake, poor focus and a small lens aperture [49, 50].

A camera's auto-focus (AF) adjusts the camera lens to establish sharp focus. AF works either by using contrast sensors within the camera(passive AF) or by emitting a signal to illuminate or estimate distance to the point of interest (active AF). Passive AF can be performed using either the contrast detection or phase detection methods, but both rely on contrast for achieving accurate autofocus [49, 50].

AF sensors are the engine behind achieving accurate focus, and are organized in various arrays across the image's field of view. Each sensor measures relative focus by assessing changes in contrast at a respective point in the image where maximal contrast is assumed to correspond to maximal sharpness. The most important factors influencing AF are the light level, subject contrast and camera or subject motion. The robustness and flexibility of autofocus is primarily a result of the number, position and type of autofocus points made available by a given camera model. Also, the number and accuracy of autofocus points can also change depending on the maximum aperture of the lens used [49].

Digital cameras are equipped with different focus modes for different situations based on the adaptation of the lenses' position for each situation [49].

Image noise is the digital equivalent of film grain for analogue cameras. It appears as random speckles on an otherwise smooth surface and can significantly degrade image quality. As previously mentioned, higher ISO amplifies the signal received from the light photons. However, this amplification of the signal also amplifies the background electrical noise that is present in any electrical system. Each sensor's cavity generates electrical noise that can contaminate its neighbor.Thus, a camera with a larger image sensor is preferred because cavities can be physically further apart and, consequently, be less affected by that contamination. Camera manufacturers have incorporated in their firmware noise reduction algorithms which work only to a certain extent: the removal of noise is frequently accomplished at the expense of fine image detail [49].

Concerning camera settings, mobile phones' manufacturers are seeking default procedure to test the quality of mobile phones' cameras. In [52] an approach to test mobile phone cameras was proposed. Several camera parameters are adjusted and afterwards the image is acquired in a controlled environment in a way that the acquisition conditions represent the typical conditions present in the real world use of the camera phone.

2.3.3 Color charts

In 1976 a color-rendition chart was proposed to fill the need to evaluate a color-reproduction process [53].

In color-related fields, a color chart is a physical arrangement of standardized color samples, used for color comparisons and measurements to investigate the color reproduction performance of an imaging system. Color charts are used to calibrate and to profile graphic devices, such as digital cameras and scanners [54].

The color-rendition chart developed in 1976 is nowadays named ColorChecker Classic. Represented in Figure 2.9, the ColorChecker Classic includes a patented array of 24 scientifically prepared natural, chromatic, primary and greyscale squares. Many of the squares represent natural objects, such as human skin, foliage and blue sky. Since they exemplify the color of their counterparts and reflect light the same way in all parts of the visible spectrum, the squares will match the colors of representative samples of natural objects under any illumination, and with any color reproduction process. Each solid patch is formulated individually to produce a pure, flat, rich color. Given the fact that it represents the primary colors red, green, blue and the secondary, cyan, magenta and yellow (RGBCMY) it is ideally suited for the print production process [55].

Figure 2.9: ColorChecker Classic [55].

On the other hand, Figure 2.10 consists of the ColorChecker Digital SG designed to digital photography. It is constituted by an array of 140 colors chosen for its location in color space to expand the color gamut. The 44 patches on the periphery of the target are a pattern of three neutral patches (white, grey, and black) designed to evaluate the uniformity of the Iiluminance and the light color temperature over the target. Also, there are 24 patches from the original ColorChecker, 17-step grey scale and 14 patches were specifically selected to simulate the appearance of various skin shades (in addition to the two of the original ColorChecker). These additional skin-tone reference colors deliver accuracy and consistency over a wide variety of skin

tones, and grey scale steps provide accurate control of camera balance to maintain a neutral aspect, regardless of light source. The ColorChecker Digital SG represents a larger gamut that the traditional ColorChecker and and provides greater refinement of image color reproduction.

Figure 2.10: ColorChecker Digital SG [55].

Other color charts include the IT8 Scanner, which has 288 patches but is designed to characterise scanners; the TE233 a color chart, designed for measuring the color reproduction of high definition (HD) cameras with 24 colors, however only 4 skin tones or the DTV Color Rendition Test Chart which consists of 36 color patches and a 9-step grey scale designed to evaluate the color rendition of high definition television (HDTV) cameras [56].

2.4 State-of-the-art

Throughout the years there have been several attempts to address the color calibration issue.

In [57] an imaging system with calibrated color image acquisition for use in dermatology is proposed. The calibration procedure is based on 24 patches with known color properties and results in a number of settings called a profile which takes 5 minutes to perform. In this imaging system the sRGB color space was used as the device independent color space for the calibration. The relationship between the input RGB color and the sRGB color space was modeled through a polynomial transform. Transforms with different complexities - 3, 6, 8, 9 and 11 terms - were compared. The coefficients of the transforms were determined by the comparison of the RGB values of the patches as measured by the system and those measured with a spectrophotometer. The set of linear equations were solved in a least squares sense, through singular value decomposition (SVD). The best accuracy was obtained for the least complex polynomial transform, the 3 by 3 linear transform computed with SVD. The accuracy result was a ΔE_{ab} of 6.21.

On the other hand, [15] proposed a color correction system, using a color compensation chart, which adopted the concepts of color management system (CMS) and profile connection space (PCS). The color correction algorithm of the proposed system consists of two steps: the profile creation process and the profile application process. The former estimates the relationship between the colors of the patches in the captured chart image and the internal reference colors. The system creates an ICC color profile, and embeds the relationship in the profile. The latter, uses the created profile as the source profile to correct the colors of other images captured under the same conditions as that of the chart image. The profile creation process is divided in four main steps: Tone reproduction curves (TRC) estimation, by applying curve regression to fit RGB colors of eight grey patches to those of the internal reference chart; color space conversion from RGB to XYZ; correction of the image color in the PCS by linear transformation estimated by SVD; and, finally, ICC color profile creation with the relationship to correct the image color embedded. The performances obtained for this system under various light sources are presented in Table 2.2.

Table 2.2: Color differences obtained in [15] under various color temperatures.

	6500 K	4150 K	2300 K	3100 K	2865 K
$\Delta E_{ab}^{ORIGINAL}$	4,24	8,1	28,4	17,6	21,9
$\Delta E_{ab}^{PROPOSED}$	5,82	6,91	14,7	9,01	8,51

In [58] a color reproduction system for images captured by digital camera is presented with the same work-flow as that of [15]. Albeit, the first accounts for two improvements regarding the profile creation process:

1. A brightness compensation was included before the TRCs estimation to compensate the error caused by non-uniform brightness of the chart.

2. An optimization of the correction matrix was performed to refine the correction matrix via Newton's method.

Experimental results show this system to have better performance than that of [15]. These results are shown in Table 2.3

Table 2.3: Color differences obtained in [58] under various color temperatures.

	6500 K	4150K	2300K	3100K	2865K
$\Delta E_{ab}^{ORIGINAL}$	6,41	8,10	28,40	17,60	21,90
$\Delta E_{ab}^{PROPOSED}$	4,27	6,40	10,70	7,25	7,12

Moreover, [59] also proposed the same algorithm for color correction of images cap-

tured by digital camera as in [58] with the modification of the color space used for the PCS. Here, the CIE LAB was used as the device independent color space, thus the image correction was performed in this color space. However, only the CIE XYZ encoding of the PCS can be used with the ICC color profile and therefore, the correction matrix had to be transformed to XYZ color space. Regardless, experimental results show no improvements in this system when compared to [58].

In [60] a method to assess skin color from digital images is presented. Uncalibrated images taken under unknown illuminants with uncalibrated digital cameras were color corrected by a 3 x 4 linear transform that maps the mean patch camera color values onto the reference target values. The correction matrix was computed so to minimize the least square error and provided a 3 x 3 color transform plus a per-component offset. A $\Delta E_{ab} \simeq$ of 5 was achieved under unknown light conditions.

Furthermore, in [61] a study was conducted to evaluate whether a customised color space transform combined with data fitting by the Least Absolute Shrinkage and Selection Operator (LASSO) regression offered a viable option for the reduction of calibration errors down to acceptable values without requiring high order non-linear terms. The results show that the application of the LASSO regression was successful at eliminating noticeable color differences, achieving a ΔE_{ab} of 2.1 under unknown light conditions. Despite this result, this methodology suggests a color space transform that does not follow the recommendations provided by the ICC.

Gong et al., 2015 [62] presented a color calibration method between individual digital cameras. This method is based on the prediction of color information via colorimetric characterization modelling. The relationships between LAB values of the ColorChecker and digital inputs for digital cameras were described mathematically by a forward and inverse colorimetric characterization modelling. Thus, through the proposed procedure a digital camera could achieve the same color information as that of a target digital camera when capturing the same scene under the same environment. In this method, an image of the ColorChecker is recorded by the test camera and the target camera, and a forward colorimetric characterization modelling for the test camera is performed which maps the conversion from RGB towards LAB. Then, an inverse colorimetric conversion from LAB to RGB is performed for the target camera. Through these two models, a prediction of the device independent information can be performed by the forward characterization, and then that information can be converted to the RGB digital inputs, which are the same as those of the target camera, through the inverse characterization. The performance of this system used the ΔE_{00} metric so a direct comparison between the previous methods cannot

be performed. However, color differences of less than 2 ΔE_{00} units were achieved. Moreover, the performance achieved with the ColorChecker Digital SG was compared to the performance obtained with ColorChecker Classic, and ColorChcecker Digital SG achieved higher accuracies.

In [63] a system to perform color calibration of an RGB camera mounted in front of a microscope with strong color distortion was proposed. This system corresponds to a microscope imaging system with several optical elements that modify the light spectrum and distort the observed colors. Thus, the proposed color calibration process accounts for a pre-processing of the camera images in addition to the color calibration task. The pre-processing was divided in a white balance correction, gamma correction and saturation enhancement. This system's performance was calculated by the average ΔE_{94} color distance between the ground truth colors and camera colors after pre-processing and color calibration, and color differences of 2.32 units were achieved. However, a direct comparison cannot be performed given that the metric is not the same.

Several papers describe the use of deep learning as a feasible tool for color calibration [64, 65]. In [64] a modified learning algorithm that trains the Radial Basis Function Networks (RBFN) model for the colorimetric characterization of color printers is proposed. On the other hand, in [65] a convolutional neural network was trained to solve the problem of color constancy as an illumination classification problem. The deep learning architecture was designed so that the output of the network could be directly used for computing the color of illumination. Although experimental results show that the method outperformed previous color constancy methods, it still shows some failure cases, such as when the assumption of a single illuminant is violated, which assumes an important role for the use case: a system that is to be used in non-controlled lighting conditions. Furthermore, other implications arise from the deep learning approaches usage. The color calibration to be developed in the course of this thesis is to be implemented in mobile devices and deep learning techniques are computational heavier and more difficult to implement, besides it has been demonstrated that it has similar performances when compared to polynomial approaches [66].

Although there have been many approaches to solve the color calibration problem, both targeted and non-targeted to skin applications, most solutions only take into account post-acquisition processing of the image. In [62] the ColorChecker Classic was compared with the ColorChecker Digital SG and better performances were obtained when the latter was used instead of the former. In [63] a set of pre-

correction methods are introduced. The approaches suggested in [15, 58, 59] are the approaches that best fit the ICC recommendations for color transformations. Besides, the comparison between [58, 59] shows no significant difference whether XYZ or LAB are used as the device independent color spaces.

3

Methods

The methodology developed to calibrate color was divided in two main stages: a pre-acquisition stage, where the best parameters for image capture are studied, and a post-acquisition stage, which accomplishes the calibration process itself. The final system consists of an android application that acquires images with the camera settings studied in the first step and performs the calibration task over the acquired image. The calibration task is performed in two main stages: a profile creation process and a profile application process. The implemented method is illustrated in Figure 3.1.

A color chart that consists of the ground truth colors is required for both of the stages and subsequently its detection and color patches extraction. The justification for the color chart used in this work is presented in the first section, followed by a color chart detection section, with the detection algorithms description. Then, the pre-acquisition step is explained, followed by the post-acquisition section. The android implementation section describes the steps to implement the created system in an android environment and shows the final application. Finally, the tests carried to evaluate the performance of the system are described.

3.1 Color chart

The ColorChecker Digital SG was selected to be the ground truth reference colors in this system. This chart provides the reference colors for the estimation of the relationship between the colors in the image and the actual colors.

This chart was selected because it contains 14 skin shades instead of 2 of the ColorChecker Classic (highlighted in red in Figure 3.2). This way, the created model is expected to more easily adapt to various skin shades, which is useful regarding that the system will be used with skin lesion images. Besides, in [62] the performances

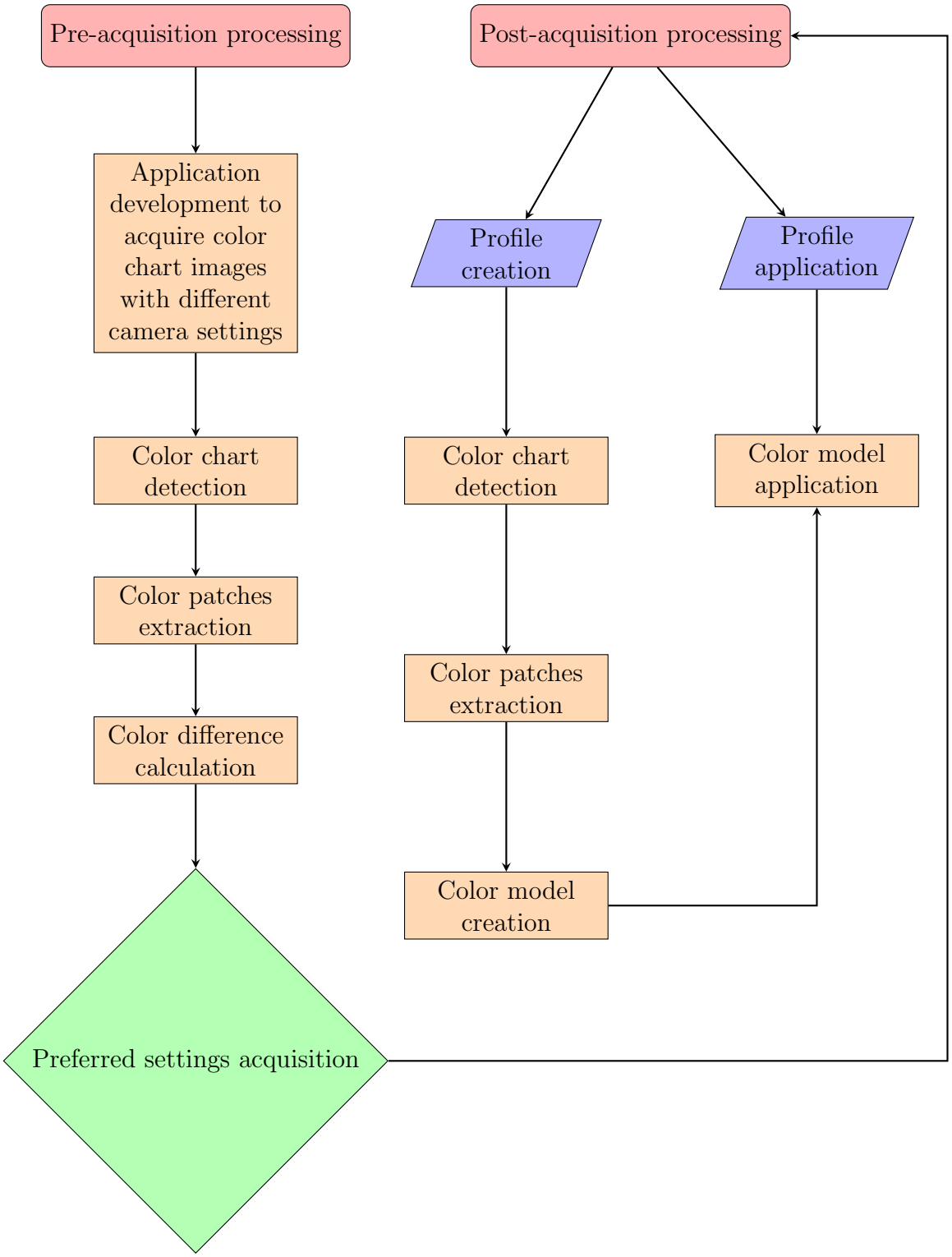

Figure 3.1: Methods' work-flow.

of a calibration system using a ColorChecker Classic target were compared with ColorChecker Digital SG and better performances were obtained with the latter.

Figure 3.2: Skin shades highlighted in red and periphery patches highlighted in yellow.

Moreover, the fact that it had 44 patches on the periphery, highlighted yellow in Figure 3.2, to account for illuminace differences along the image being acquired was also an important factor in color chart selection since the light source can modify a lesion's color. Figure 3.3 [16] shows a skin lesion non-uniformly illuminated which causes some lesion areas to appear white.

Figure 3.3: Example of a non-uniformly illuminated skin lesion.

Finally, the extended color gamut was also held in account because this system is addressed for mobile phone devices and the 140 patches were chosen specifically for its location in the color space to capture the full capabilities of digital cameras. The selected chart has thus 140 patches with colorimetric reference data provided by xRite [55] measured with the i1Pro 2 spectrophotometer under the D50 illuminant. These values are presented in Appendix B.1.

3.2 Color chart detection

An algorithm to automatically detect the color chart patches was developed since both pre and pos-acquisition processes required the color extraction of the patches. Two approaches towards this goal are presented. However, the first approach, which corresponds to the appearance-based method (discussed in Section 3.2.1), was not successful. The last approach presented, the feature-based method (described in Section 3.2.2), was the implemented in the final system.

Appearance-based methods make direct use of pixel intensities to establish dense inter-frame correspondences, leading to a higher demand of computation power. Feature-based methods deploy image abstraction strategies which identify distinguishing key points from image intensities and extract their vector representations. In the feature space, a matching process is performed to establish a set of inter-frame point correspondences [67].

3.2.1 Appearance-based method

The appearence-based algorithm implemented is illustrated in the flowchart in Figure 3.4 and was adapted from [68].

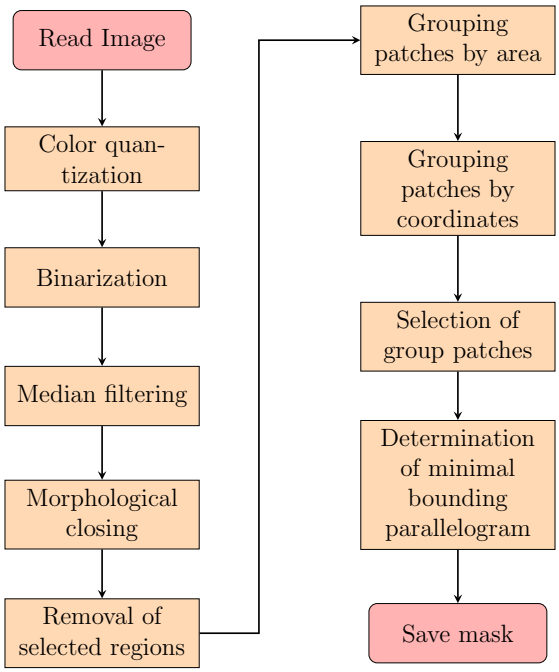

Figure 3.4: Illustration of the suggested appearence-based method.

(a) Source image for chart detection.

(b) Color quantization of the source image with 25 clusters.

(c) Color quantization of the source image with 141 clusters.

Figure 3.5: Source image (a); result of the color quantization process for 25 (b) initial clusters; result of the color quantization process for 141 initial clusters(c).

Figure 3.5a represents the source image used in this section as an example to demonstrate each step of this algorithm.

The first step was the color quantization to reduce the number of colors in the image and eliminate small differences in color values between image regions with similar colors, hence grouping those patches. It was performed with k-means clustering method with 25 initial clusters.

The k-means procedure starts with k groups each of which consist of a single random point, called centroids, and thereafter each point belonging to a given data set is associated to the nearest centroid. When no point is pending, the first step is completed and an early grouping is performed. The centroids of the k groups are adjusted in order to take account of the new points. Thus at each stage the k-means are the means of the groups they represent, hence the term k-means. The k centroids change their location step by step until no more changes are done. This algorithm aims at minimizing an objective function, in this case a squared error function in Equation 3.1, where $\left\| x_i^{(j)} - c_j \right\|$ is a distance measure between a data point $x_i^{(j)}$ and

the cluster centre c_j.

$$J = \sum_{j=1}^{k} \sum_{i=1}^{k} \left\| x_i^{(j)} - c_j \right\|^2 \tag{3.1}$$

In [68] the number of initial clusters was set to 25, whether if the segmentation was regarding ColorChecker Classic or ColorChecker Digital SG. The number of initial clusters was chosen to ensure that even small number of pixels of chart patches would not be included to the cluster containing the pixels in colour of the chart's frame. Therefore, the number and values of initial cluster centres did not have to match the number of patches of the color chart. However, an initial number of 141 clusters was also tested, to account for the 140 patches and the chart's frame.

Figure 3.5b shows the result of color quantization applied to the source image with 25 initial clusters, whereas Figure 3.5c depicts the result for 141 color clusters. A final number of 25 clusters was implemented given that it involves less computation time and performs better, since 141 clusters did not reduce the number of colors in the source image.

Thus, the color quantization algorithm is composed of the following steps:

1. Selection of 25 random colors as initial cluster centres;
2. distances between color pixel values and selected cluster centres calculation;
3. assignment of the color pixel value to the nearest cluster centre;
4. calculation of the new cluster centres as arithmetic mean values of colors assigned to color clusters.

The next step was the binarization process that assigned each color a separate binary image. The new binary images are formed by the formula in Equation 3.2:

$$I_k = \begin{cases} 1 & I(x,y) = [R_k,G_k,B_k] \\ 0 & I(x,y) \neq [R_k,G_k,B_k] \end{cases} \tag{3.2}$$

where $I_k(x,y)$ is the binary image for k-th cluster centre, $I(x,y)$ is the color value of pixel of quantized image in coordinates (x,y) and $[R_k,G_k,B_k]$ is the final color value of k-th cluster centre. Figure 3.6a shows the result of the binarization.

To improve the binary images two operations were performed. First, a 5x5 median filtering was applied to remove noise. The median filtering takes the median of all

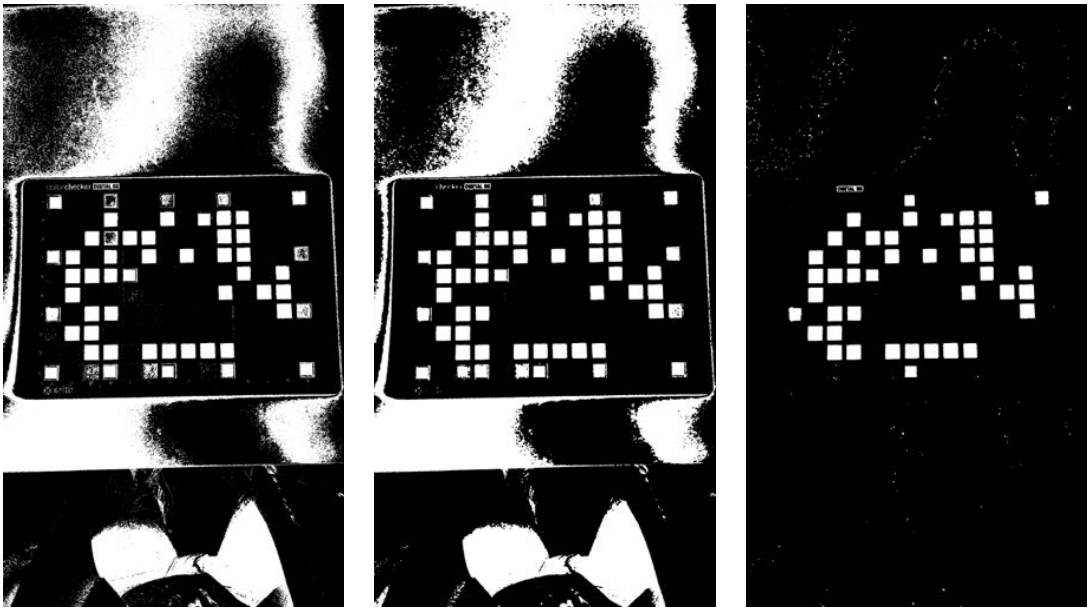

(a) Binarization of the quantized image.

(b) Morphology operations applied to the binary image.

(c) Removal of regions by shape.

Figure 3.6: Result of the binarization process (a); result of the morphology operations (b);result of the regions removal by shape (c).

the pixels under kernel area and replaces the central element this median value, which means that in a 5x5 window size means the central pixel will have the value of the 13th largest pixel value. The main objective of this filter is to force pixels with different values to resemble the remaining, which is highly effective in removing salt-and-pepper noise [41]. Then, a morphological closing operation with the same window size is applied to fill small holes in regions. A closing operation corresponds to a dilation operation followed by an erosion operation and they intend to smooth the image through the addition of pixels to it. In the former, the dilation operation, the kernel slides through the image and a pixel in the original image is only considered 1 if at least one pixel under the kernel is 1, thus it increases the white region in the image or size of foreground object increases. On the other hand, in the latter, the erosion operation, a pixel in the original image will be considered 1 only if all the pixels under the kernel are 1, otherwise it is eroded, i.e., made to zero [41]. Figure 3.6b shows the result of both operations in binarized image.

Afterwards, the shape of the regions is compared to the shape of color patches. The square shape of the chart patches is distorted due to the acquisition process and image processing in the previous steps of the algorithm. To evaluate the regions' shapes two conditions were established:

1. the Euler number must be 1. The Euler number corresponds to a scalar whose value is the number of objects in the image minus the total number of holes in those objects. Objects are considered connected sets of pixels having a value of 1. Thus, an Euler number of 1 corresponds to an image without holes [69].

2. the circularity factor, defined as $\frac{4\pi A}{P^2}$, where A is the region's area and P is the perimeter, must be in the range specified by Equation 3.3 [70]:

$$0.65 < \frac{4\pi A}{P^2} < 0.95 \tag{3.3}$$

The regions that did not meet above conditions were removed, which can be observed in Figure 3.6c.

However, the previous stages did not remove all the regions that were not potential patches. In order to detect the color chart, the size and location of color patches were also used. For this purpose, a hierarchical clustering algorithm was performed, which works by grouping data objects into a tree of clusters [71]. The grouping is based on differences in areas between potential patches as shown in Equation 3.4, where ΔA_{ij} is the absolute difference between i-th and j-th areas, A_i and A_j are the areas of i-th and j-th potential patches.

$$\Delta A_{ij} = \left| A_i - A_j \right| \tag{3.4}$$

First, the patches with the smallest absolute differences between areas are joined. Patches are joined to groups as long as the relative differences between the mean areas of both groups are less than 30%, Equation 3.5 where $\bar{A}_m$ and $\bar{A}_n$ are the mean areas of m-th and n-th groups.

$$\begin{aligned} \left| \frac{\bar{A_n} - \bar{A_m}}{\bar{A_n}} \right| &< 0.3 \\ \left| \frac{\bar{A_n} - \bar{A_m}}{\bar{A_m}} \right| &< 0.3 \end{aligned} \tag{3.5}$$

The patch grouping process ends, when a group can no longer be created. The obtained groups of patches with similar area are then grouped based on the coordinates in the image. The goal of this step is to remove the elements of group which do not belong to chart patches. This grouping is also achieved through hierarchical clustering using the Euclidean distance between coordinates of centroids of two

groups. Similarly to the previous clustering method, the groups are first joined by the smallest distance between their centroids. The grouping results are depicted in Figure 3.7a.

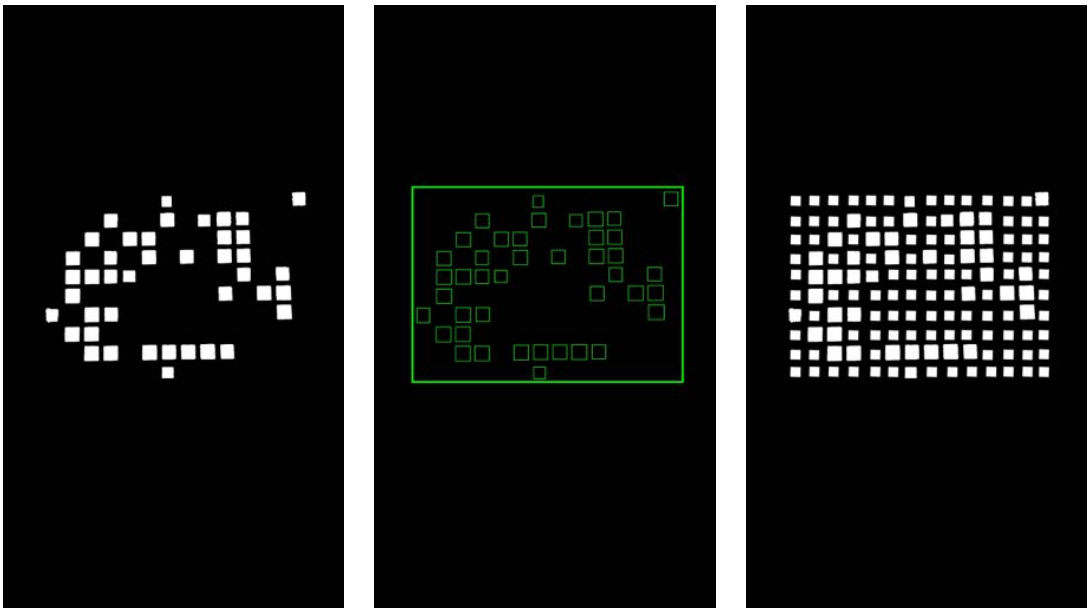

(a) Patches grouped by area and coordinates.

(b) Bounding Rectangle.

(c) Final mask for source image.

Figure 3.7: Patches grouped by area and coordinates 3.7a; Bounding Rectangle 3.7b; Final mask for source image 3.7c.

After the color patches grouping, the minimum-area bounding rectangle for the specified point set was determined, which allowed to know the four vertices of both the chart and of each of the patches found, as shown in Figure 3.7b.

The missing patches are designed based on the minimum area of the detected patches and its location was based on the minimum distance between located patches. Figure 3.7c shows the final mask developed for the source image.

As can be observed, this algorithm faced many difficulties in color chart detection due to deformation of shape and was therefore discarded since color chart detection and color extraction were vital to the calibration process, hence a robust algorithm was essential.

3.2.2 Feature-based method

As previously mentioned, feature-based methods have advantages when compared to appearance-based methods, thus the former were selected as the robust algorithm

to detect color chart in the system developed. The basic idea of a feature-based algorithm is to first detect interest regions - keypoints - that are covariant to a class of transformations. Then, for each detected regions, an invariant feature vector representation - descriptors - for image data around the detected keypoint is built. Feature descriptors extracted from the image can be based on second-order statistics, parametric models, coefficients obtained from an image transform, or even a combination of these measures [72].

In the literature, a large variety of feature extraction methods have been proposed to compute reliable descriptors. Among these descriptors, the scale invariant feature transform (SIFT) descriptor [73] and the speeded-up robust features (SURF) descriptor [74] for computing distinctive invariant local features quickly are the most popular and widely used in several applications [72]. However, both these algorithms are patented local feature detectors, thus not feasible for commercial applications. In [75] a quantitative comparison of 10 different feature descriptors is performed. Although the results show the most accurate feature for matching methods to be the SURF algorithm, KAZE [76] and A-KAZE [77] are also suggested as two very accurate algorithms that can compete with SURF. Moreover, a study in [78] also showed that A-KAZE is at least as accurate as KAZE while being significantly faster. For these reasons, the chart's detection in this system is performed using A-KAZE feature detector and descriptor, and a brief explanation of the A-KAZE's algorithm is provided.

A-KAZE detects and describes features in non-linear spaces thanks to the use of non-linear diffusion filtering, which makes blurring locally adaptive to the image data. Thus, it preserves the boundaries and causes the blurring of small details [77].

KAZE and A-KAZE differ mainly on the discretization scheme used to find an approximation of the solution to the non-linear diffusion equation. To obtain low-computationally demanding features, taking advantage of the benefits of non-linear diffusion filtering, the latter uses a mathematical framework called Fast Explicit Diffusion (FED) to approximate the solution. The FED is embedded in a pyramidal framework with a strategy to decrease the feature detection in non-linear scale spaces time consumption [77].

Feature description is performed through Modified-Local Difference Binary (M-LDB) that exploits gradient and intensity information from the non-linear scale space. The LDB descriptor uses binary tests between the average of subdivisions instead of single pixels, as well as the mean of the horizontal and vertical derivatives in the areas being compared. The averages of those subdivisions are very fast to

compute using integral images if the descriptor is upright. However, considering the rotation of the keypoints to perform the mean of all points in a rotated subdivision is expensive. M-LDB performs the rotation invariance by estimating the main orientation of the keypoint and, instead of calculating the average of all pixels inside each subdivision of the grid, the grids are sub-sampled in steps that are a fuction of the scale of the feature [77].

The process of finding frame-to-frame correspondences between descriptors can be formulated as the search of the nearest neighbor from one set of descriptors for every element of another set and it is called the "matching" procedure. On of the algorithms to perform this matching is the Brute-force matcher, which looks for each descriptor in the first set and the closest descriptor in the second set by trying each one (exhaustive search). The closest descriptor is found for the minimal hamming distance, the number of bits that are different from two descriptors [79].

The result of descriptor matching is a list of correspondences between two sets of descriptors. The first set of descriptors is usually called the train set, which corresponds to the pattern image. The second set is called the query set and belongs to the image that is searched for in the pattern [79].

Thus, for chart detection in this system a query image and the image with the chart to be detected were provided to the system and the objective was to find the query image in the acquired image. A-KAZE detected the keypoints for both images and computed their descriptors. The source image and query image are shown in Figure 3.8a and the keypoints for both images are shown in Figure 3.8b.

(a) Query image (left) and source image (right).

(b) Keypoints detected for query image (left) and for source image (right).

Figure 3.8: Query and source images 3.8a and keypoints detected for both 3.8b.

The descriptors of both images were then matched with brute force matcher, with resource to the hamming distance metric. This result of the matching procedure is illustrated in Figure 3.9a. Afterwards, the transformation between matched keypoints is found, which corresponds to a homography transformation matrix, and

thus the color chart detection in the source image is performed, Figure 3.9b.

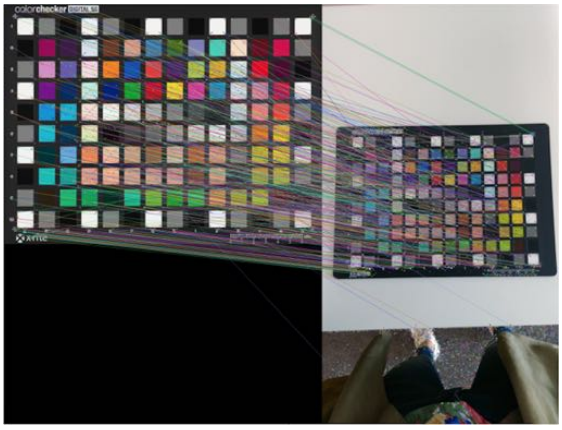

(a) Matches for the descriptors of both images.

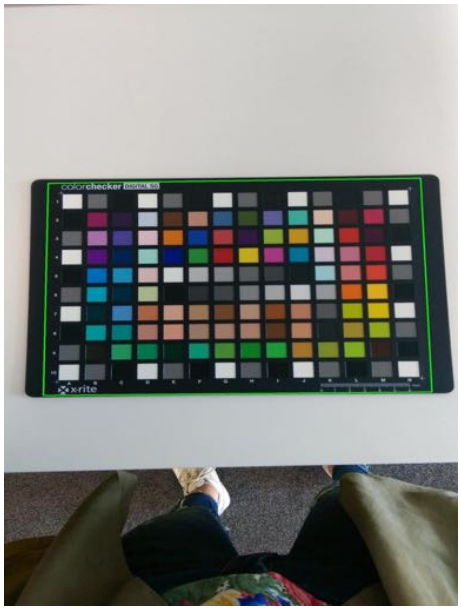

(b) Detection of the color chart in the source image.

Figure 3.9: Matches between source and query image 3.9a and color chart detection 3.9b.

This transformation is estimated using the random sample consensus (RANSAC) method to find the best homography matrix by probing subsets of input points and marking each correspondence as either inlier or outlier, depending on the reprojection error for the calculated homography matrix. The perspective of the object is thus corrected to that of the query image (Figure 3.10a) so that a mask, previously designed and provided to the system(Figure 3.10b), correctly overlaps the patches, Figure 3.10c. All color chart detections required for this system's development were performed via this algorithm.

(a) Perspective correction of the source image.

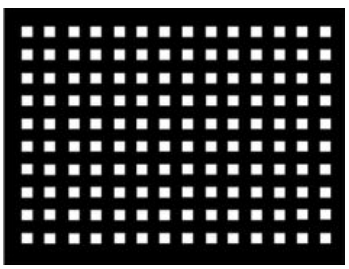

(b) Mask designed.

(c) Superposition of the mask over the corrected perspective of the source image.

3.3 Pre-acquisition processing

The pre-processing method is based on the development of an android application to acquire color chart images with different camera parameters. Figure 3.11 shows the app developed which allowed to select the acquisition settings and save both image and a .txt file to keep record of the settings with which the images were acquired.

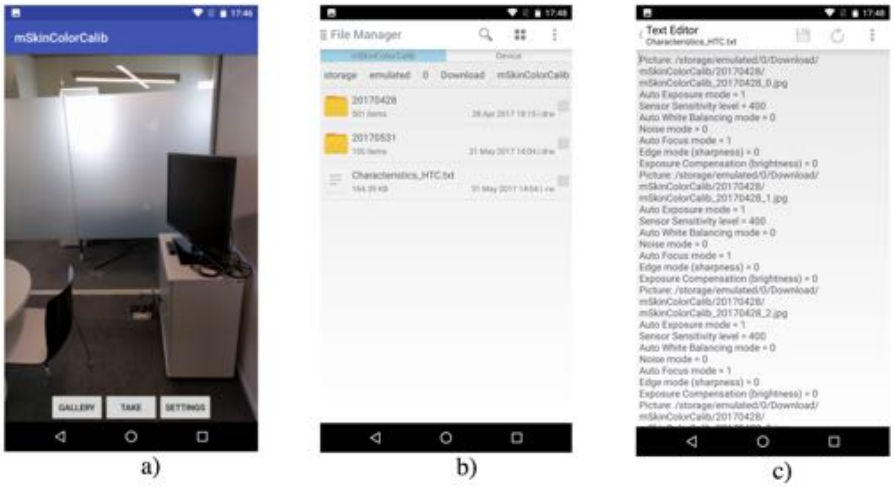

Figure 3.11: a) Android application main activity; b) Folders with images and a .txt file saved in external storage; c) Acquisition settings recorded in .txt file.

Figure 3.12a corresponds to the activity in which the settings were selected. The first switch button corresponds to the auto-exposure, which was necessary to include because ISO speed can only be modified if the auto exposure is disabled. On the other hand, the exposure is only possible to change if the auto-exposure is enabled.

The Iso a seek-bar allows to set the ISO speed. The bar range adapts to the supported range of each camera device. As mentioned before, this control is only effective if the auto exposure control mode is disabled, otherwise the auto-exposure algorithm will override this value.

The AWB button represents the auto white balance modes available for the specific mobile device. When the button is pressed a pop-up menu appears with the options available for the device, which is shown in Figure 3.12b. The possible routines for the AWB mode are:

- Off - the auto white balance routine is disabled;
- Auto - each of the white balance routines can be enabled based on temperature sensors.

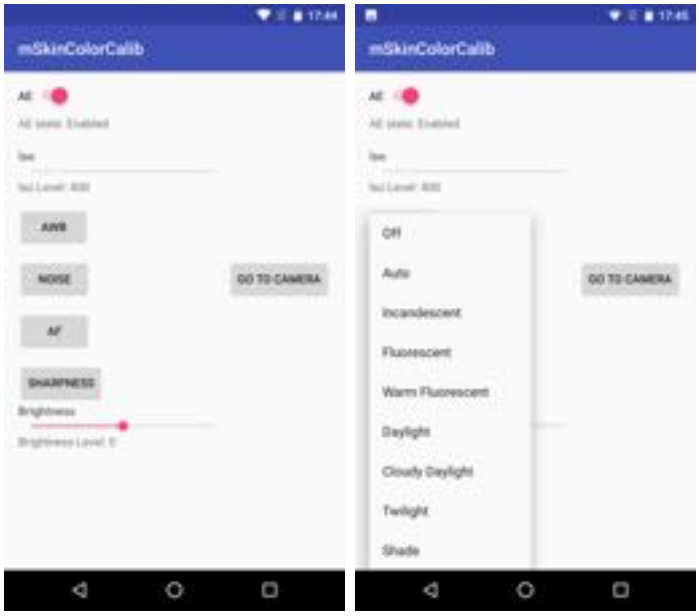

(a) Android application settings activity. **(b)** Pop-up menu for the AWB button.

Figure 3.12: Android application settings activity (a) and pop-up menu for the AWB button (b).

- Incandescent - the camera device uses incandescent light as the assumed scene illumination for white balance. The exact white balance transforms are performed by the camera device but they will approximately match the CIE standard illuminant A.
- Fluorescent - the camera device uses fluorescent light as the assumed scene illumination for white balance. The exact white balance transforms are performed by the camera device but they will approximately match the CIE standard illuminant F2.
- Warm fluorescent - the camera device uses warm fluorescent light as the assumed scene illumination for white balance. The exact white balance transforms are performed by the camera device but they will approximately match the CIE standard illuminant F4.
- Daylight - the camera device uses daylight light as the assumed scene illumination for white balance. The exact white balance transforms are performed by the camera device but they will approximately match the CIE standard illuminant D65.
- Cloudy daylight - the camera device uses cloudy daylight light as the assumed scene illumination for white balance.

- Twilight - the camera device uses twilight light as the assumed scene illumination for white balance.
- Shade - the camera device uses shade light as the assumed scene illumination for white balance.

The noise, AF and sharpness buttons work similarly to the AWB button. When pressed a pop-up menu is also shown with the options available in the targeted device. The noise button stands for the noise reduction algorithms, whereas the AF button stands for the auto-focus modes available for each device. On the other hand, the sharpness button corresponds to the edge enhancement modes that are supported by the camera device, which improves sharpness and details in the captured image. In Table 3.1 the possible values for the noise, AF and sharpness routines are described.

Table 3.1: Routines available for the noise, AF and sharpness modes.

	Off	Auto	Fast	High Quality	Minimal	Zero shutter lag	Macro	Continuous Picture	EDOF
Noise	Routine disabled.	Non-existent routine.	Noise filtering applied without reducing capture rate.	Highest quality noise filtering applied even if it slows capture rate.	Noise reduction applied without reducing frame rate.	Noise reduction is applied at different levels, based on resolution.	Non-existent routine.	Non-existent routine.	Non-existent routine.
AF	Routine disabled.	Basic automatic focus mode.	Non-existent routine.	Non-existent routine.	Non-existent routine.	Non-existent routine.	Mode optimized for focusing objects close to the camera.	Algorithm that modified the lens position continually to provide constant focus.	Camera produces images with extended depth of field.
Sharpness	Routine disabled.	Non-existent routine.	Edge enhancement applied without reducing capture rate.	Highest quality enhancement filtering algorithms even if it slows capture rate.	Edge enhancement applied without reducing frame rate.	Edge enhancement is applied at different levels, based on resolution.	Non-existent routine.	Non-existent routine.	Non-existent routine.

Finally, the brightness seek-bar allows to set the exposure compensation range in EV units. The range of the bar adapts to the supported range of each camera device, and for devices that support exposure compensation the minimum value is always at least -2 EV and the maximum value at least 2 EV. As mentioned before, this routine is only available if the AE is enabled.

Figure 3.13 shows the setup in which the images were acquired: the distance between color chart and mobile phone were maintained the same so that the color chart would be equally illuminated through the various acquisitions (Figure 3.13a). The light source illuminating the room was also kept constant as there were no windows

only the same artificial light (Figure 3.13b). Thus, the only parameter object to modification were the acquisition settings.

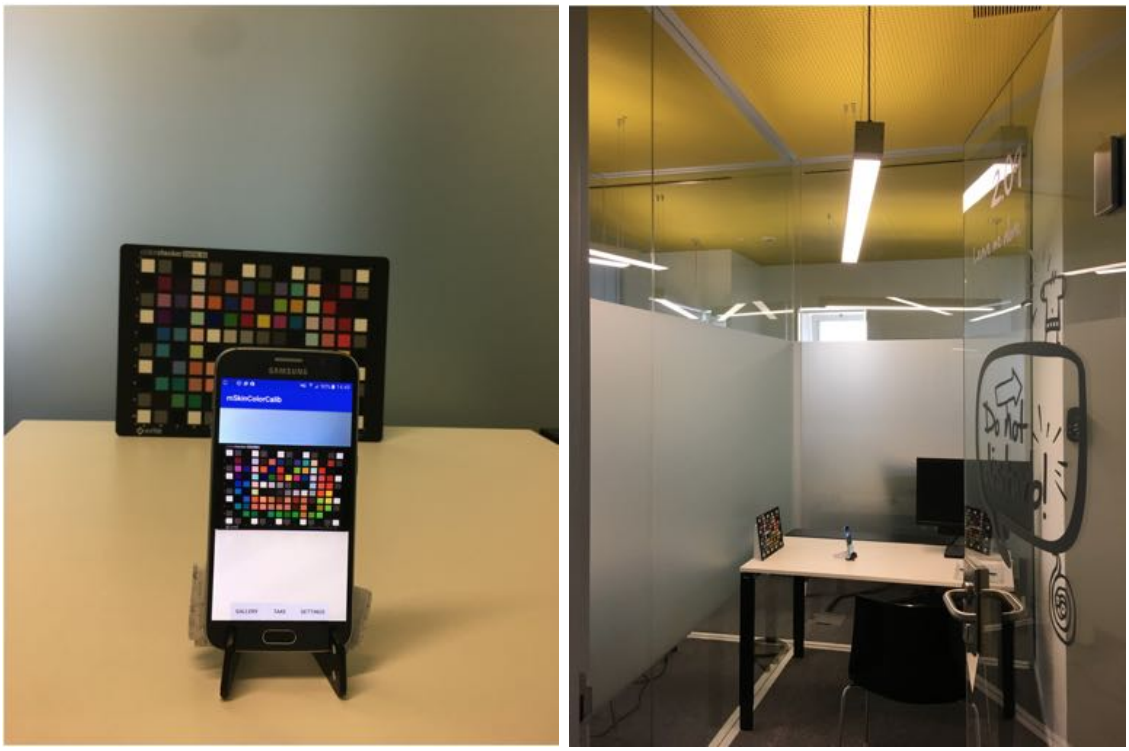

(a) Distance maintained between device and chart.

(b) Light source conditions.

Figure 3.13: Acquisition set-up.

This app was installed in 3 different mobile phone devices: Samsung S6, Nexus 5x and HTC One M8. In section 3.6.1 the settings tested in each mobile phone are described.

The color chart detection algorithm explained in the previous Section (Section 3.2.2) was applied to the images acquired with each mobile phone, and the mean color of every patches was extracted. Then, the color difference of every patch is estimated through the ΔE_{ab} formula:

$$\Delta E_{ab} = \sqrt{(\Delta L^*)^2 + (\Delta a^*)^2 + (\Delta b^*)^2}$$
$$\Delta L^* = L_1^* - L_2^*, \Delta a^* = a_1^* - a_2^*, \Delta b^* = b_1^* - b_2^* \tag{3.6}$$

where L_1^*, a_1^* and b_1^* represent the captured color, and L_2^*, a_2^* and b_2^* represent the

reference color. Then, the color difference of every patch is averaged and this average represents the color difference of the image. All color differences calculated along this thesis used the average of the ΔE_{ab} color difference of each patch.

The settings that correspond to the image with the minimum color difference are the optimal settings to acquisition. In the final system, if the mobile phone in which the system was installed is one of the above, the acquisition settings are automatically set to the optimal parameters.

3.4 Post-acquisition processing

The algorithm developed in the post-acquisition processing is divided in two steps: a profile creation process and a profile application process. This system is based in the articles [15, 58, 59] for the reasons stated in the literature review, namely the fact that these algorithms were based in the CIE recommendations and that they take advantage of the color chart's features.

3.4.1 Profile creation

The flowchart in figure 3.14 shows the profile creation process. Even though this system is based in articles [15,58,59], three correction steps, white balance correction; gamma correction and saturation enhancement, were added based in article [63].

Thus, in the developed profile creation system first, the image of the color compensation chart is captured. Then a four-step pre-correction is applied: brightness compensation (Section 3.4.1.1), white balance correction (Section 3.4.1.2), gamma correction (Section 3.4.1.3) and saturation enhancement (Section 3.4.1.4). Afterwards the tone response curves are estimated (Section 3.4.1.5) and the RGB color space of the image is converted to a device independent color space (Section 3.4.1.6). Finally, a relationship between the colors of the patches in the captured chart image and the internal reference colors is estimated (Section 3.4.1.7).

After the estimation, the system creates a color profile, and embeds the relationship in the profile. The created profile is used as the source profile to correct the colors of the other images which are captured under the same condition as that of the chart image. The color profile consists of JavaScript Object Notation (JSON) files with the relationships saved in the profile creation process and accessed in the profile application process.

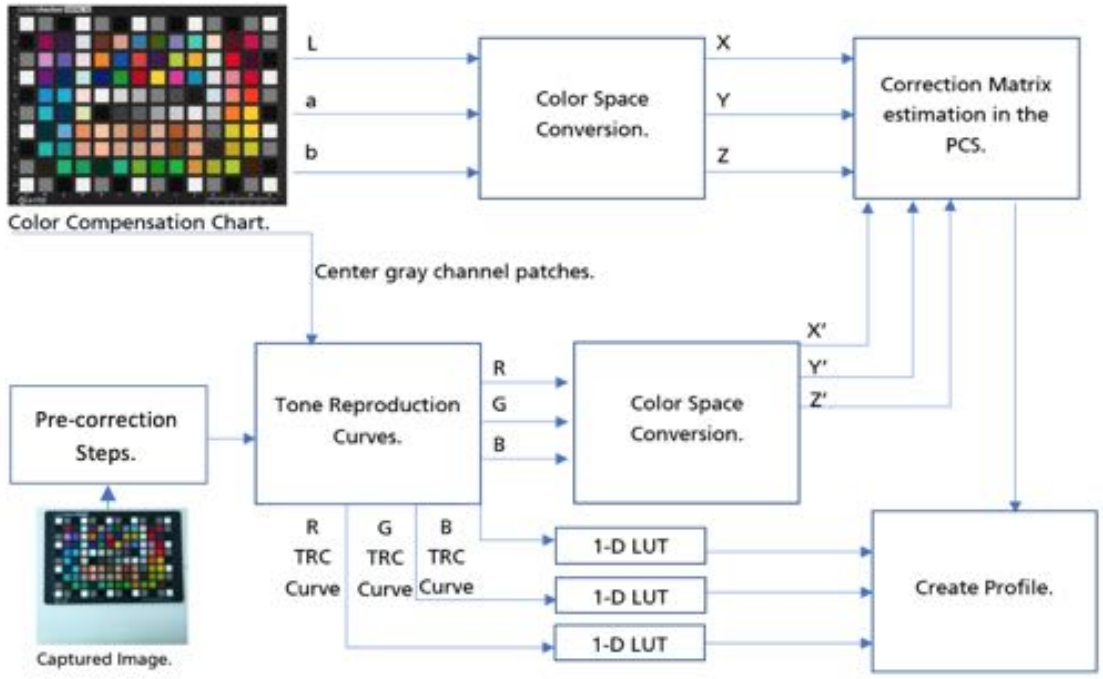

Figure 3.14: Profile creation process. The image of the color compensation chart is captured. Then a four-step pre-correction is applied. Afterwards the tone response curves are estimated and the color space of the image is converted to the XYZ device independent color space. A relationship between the colors of the patches in the captured chart image and the internal reference colors is estimated

3.4.1.1 Brightness compensation

Because of the environmental conditions such as illumination and shadow, brightness may change along the surface of the color chart, and some areas may appear to be brighter or darker. Therefore, the first pre-correction step corresponds to the brightness non-uniformity compensation. The gray patches located on the periphery of the target, Figure 3.15, are used. The colors are converted into HSI color, and the normalized intensities are considered as the brightness values. From the intensity values of the 4 patches, the intermediate brightness values are estimated using bilinear interpolation.

Then the minimum intensity of the 4 patches is subtracted from the brightness values. Figure 3.16 represents the relative brightness map for the color pathes of the source image. The brightness values are then adjusted based on the relative brightness map so that the intensities of the sample colors are flattened. After the brightness compensation, the sample colors are converted back into the RGB colors for the next step. The 4 coefficients obtained from bilinear interpolation and the minimum brightness value of the 4 patches are written to a JSON file.

Figure 3.15: Patches used for brightness compensation.

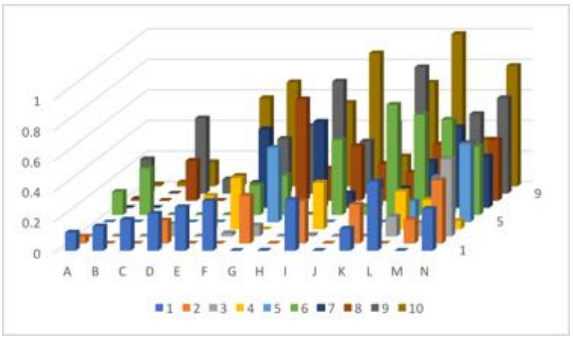

Figure 3.16: The brightness map which consists of the relative brightness values (left axis). The right axis corresponds to the color chart rows, whereas the bottom axis corresponds to the color chart columns.

3.4.1.2 White balance correction

The white balance correction was performed after the brightness compensation so that any white patch could be used as reference. This step was computed by the multiplication of each RGB value of a source color by the ratios $R_{A1}^{test}/R_{A1}^{cam}$, $G_{A1}^{test}/G_{A1}^{cam}$ and $B_{A1}^{test}/B_{A1}^{cam}$ respectively, where X_{A1}^{test} denotes the target R, G or B value of the white in the position A1 of the color chart, and X_{A1}^{cam} denotes source R, G and B value of the same patch issued from camera. These ratios are saved in the profile.

3.4.1.3 Gamma correction

After the white balance correction the ground truth colors and the camera RGB values were converted into colors of the CIE LAB. The gamma correction consisted in the plot of the lightness component of the ground truth versus the light component of the white balance corrected camera color. The points were fitted to a second-order polynomial function. The application of this polynomial function to the L

components of the camera colors made the lightness of every color closer to that of the corresponding ground truth, thus correcting the gamma value. Figure 3.17 shows an example of the 140 obtained points fitted to a second-order polynomial function. The function obtained is encoded in the profile.

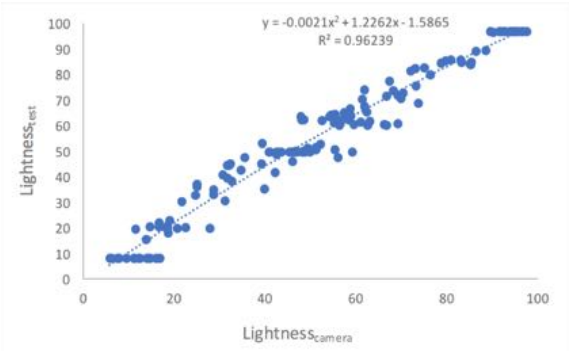

Figure 3.17: Gamma correction of lightness after correction of the white balance.

3.4.1.4 Saturation Enhancement

For each patch j the chroma component is calculated by Equation 3.7 and a C_j^{cam} value is obtained. Then, the chroma component of the ground truth color was plotted versus C_j^{cam}. These two variables correlate linearly, thus, in order to enhance the saturation the equation of the straight line was applied to the chroma components of all colors captured by the camera. An example of these correlations is shown in Figure 3.18.

$$C = \sqrt{a^2 + b^2} \tag{3.7}$$

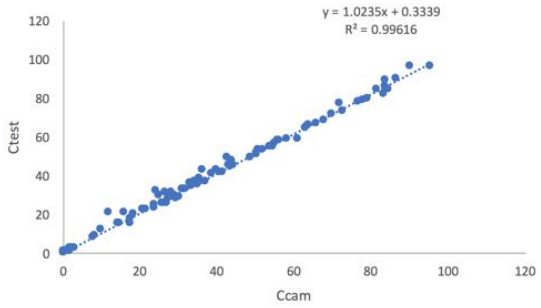

Figure 3.18: Saturation enhancement of chroma after correction of the white balance.The x-axis corresponds to the C_j^{cam} values whereas the y-axis represents the C_j^{test} values.

3.4.1.5 TRCs estimation

Posterior to the pre-correction steps the TRCs were estimated. The 12 gray patches located in the center area of the chart are used for the TRC estimation process, Figure 3.19 highlights the patches used in the TRC estimation step.

Figure 3.19: Color patches used for TRC estimation.

The use of standard image formats such as JPEG accounts for the problem that raw data is processed by a non-linear converter and transformed into standard file format. Therefore, a correction function that can compensate for the non-linearity problem is considered. The proposed system estimates the input/output non-linearity using the 12 neutral patches located in the center area of the target chart. For each of the R, G, and B channels independently, the non-linear mappings that fit the input colors by means of the 12 patches to the reference values are estimated. The correction function g_k corresponds to a non-linear mapping which transforms the input colors $x_{R^{cam}}$, $x_{G^{cam}}$ and $x_{B^{cam}}$ to the reference sample colors $y_{R^{test}}$, $y_{G^{test}}$ and $y_{B^{test}}$ as in Equation 3.8.

$$\begin{aligned} y_{R^{test}} &= g_R(x_{R^{cam}}), \\ y_{G^{test}} &= g_G(x_{G^{cam}}), \\ y_{B^{test}} &= g_B(x_{B^{cam}}) \end{aligned} \tag{3.8}$$

The non-linear mapping $g_{j,k}$ is modelled using the following curve regression:

$$\begin{aligned} g_k(x_k) &= a_{1,k}f_1(x_k) + a_{2,k}f_2(x_k) + a_{3,k}f_3(x_k) + a_{4,k}f_4(x_k), \\ f_1(x_k) &= 1, f_2(x_k) = x, f_3(x_k) = \sin(x_k), f_4(x_k) = \exp(x_k) \end{aligned} \tag{3.9}$$

Here, $a_{n,k}$ are the undetermined coefficients for each channel, and x_k are the normalized responses by the 12 patches. The coefficients of Equation 3.9 are determined to minimize the sum of the square - E_k - of the differences between $g_k(x_k)$ of the 12 patches and their reference values $y_{k,j}$. The E_k is given by 3.10.

$$E_k = \sum_{j=1}^{12} \Big[e_{k,j}\Big]^2 = \sum_{j=1}^{12} \Big[y_{k,j} - \textstyle\sum_{n=1}^{4} a_{n,k} f_n(x_j)\Big]^2 \tag{3.10}$$

Figure 3.20 shows the result of the TRC estimation process for the source image. Figure 3.20a represents three tone mapping curves for each of R, G, and B channels, and Figure 3.20b compares the red TRC with the color of patches before TRC estimation and, also, with the ground truth colors of the color chart for the 12 patches.

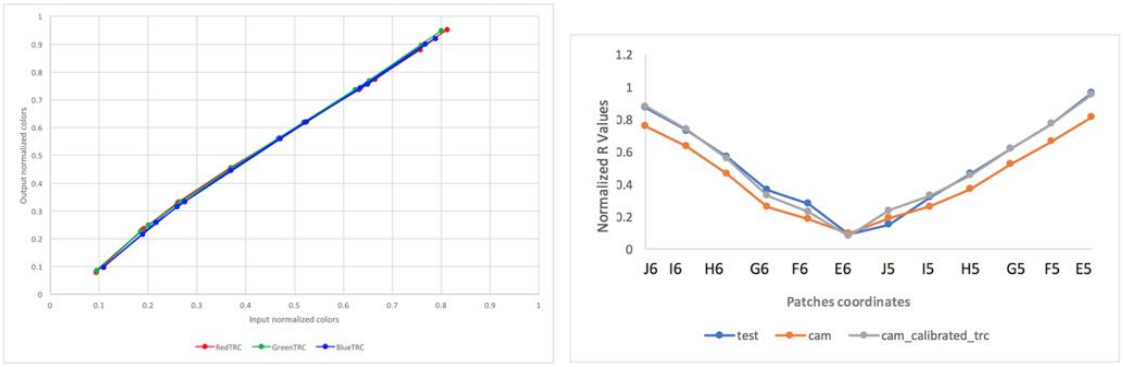

(a) Curve comparison between the test color patches, the camera acquired color patches, and the corrected color patches.

(b) TRCs for the Red channel.

Figure 3.20: Result of the TRC estimation process.

The 4 coefficients extracted for each channel are then applied in a 1-D lookup table each, established to map the input color normalized to be in the range of 0.0 to 1.0 to the output color in the RGB color space. In this system, the output function is sampled at 256 points in the range of [0,256]. These lookup tables are embedded in the profile.

3.4.1.6 Color space conversion

The following stage was the color space conversion. As mentioned before, the system adopts the concepts of PCS and CMS. They were defined by ICC to provide a reference color space as a common interface for color specification between different devices. The PCS is based on CIELAB or CIEXYZ, relative to the illuminant D50. In this system, XYZ color space was introduced for the PCS. Therefore, RGB colors of the patches in the image are converted into those of XYZ color space before the estimation of the transformation.

The devices' color space is the sRGB, thus the color space conversion is obtained as shown in Equation 3.11,in which M_{conv} maps the input RGB color to XYZ value [46].

$$\begin{bmatrix} X \\ Y \\ Z \end{bmatrix} = M_{conv} \begin{bmatrix} y_R \\ y_G \\ y_B \end{bmatrix} = \begin{bmatrix} 0.412424 & 0.357579 & 0.180464 \\ 0.212656 & 0.715158 & 0.072186 \\ 0.019332 & 0.119193 & 0.950444 \end{bmatrix} \begin{bmatrix} y_R \\ y_G \\ y_B \end{bmatrix} \tag{3.11}$$

However, the reference white of sRGB is the D65 which is different from the PCS white, D50. In such case, a chromatic adaptation transformation is required in order to compensate for the mismatch of the reference white. The linear Bradford model for the chromatic adaptation transformation is shown in Equation 3.12 [46].

$$\begin{bmatrix} X \\ Y \\ Z \end{bmatrix}_{D50} = M_{adapt} \begin{bmatrix} X' \\ Y' \\ Z' \end{bmatrix}_{D65} = \begin{bmatrix} 1.047835 & 0.022897 & -0.050147 \\ 0.029556 & 0.990481 & -0.017056 \\ -0.009238 & 0.015050 & 0.752034 \end{bmatrix} \begin{bmatrix} X' \\ Y' \\ Z' \end{bmatrix}_{D65} \tag{3.12}$$

Thus, the color space conversion for the proposed system is obtained as the multiplication of matrices M_{conv} by M_{adapt}, as shown in Equation 3.13.

$$\begin{bmatrix} X \\ Y \\ Z \end{bmatrix}_{D50} = M_{CVS} \begin{bmatrix} y_R \\ y_G \\ y_B \end{bmatrix} = M_{conv} \times M_{adapt} \begin{bmatrix} y_R \\ y_G \\ y_B \end{bmatrix} = \begin{bmatrix} 0.436052 & 0.385082 & 0.143087 \\ 0.222492 & 0.716886 & 0.060621 \\ 0.013929 & 0.097097 & 0.714185 \end{bmatrix} \begin{bmatrix} y_R \\ y_G \\ y_B \end{bmatrix} \tag{3.13}$$

3.4.1.7 Chromatic transformation

The last step in the profile creation process is the correction of the image color in the PCS.

The colors of the image are corrected by the linear transformation which maps the colors of the image into those of the reference colors in the PCS as shown in Equation 3.14.

$$M_{XYZ} = M_{Crr} M'_{XYZ} <=> \begin{bmatrix} X_1 & X_2 & & X_N \\ Y_1 & Y_2 & ... & Y_N \\ Z_1 & Z_2 & & Z_N \end{bmatrix} = \begin{bmatrix} m_{11} & m_{12} & m_{13} \\ m_{21} & m_{22} & m_{23} \\ m_{31} & m_{32} & m_{33} \end{bmatrix} \begin{bmatrix} X'_1 & X'_2 & & X'_N \\ Y'_1 & Y'_2 & ... & Y'_N \\ Z'_1 & Z'_2 & & Z'_N \end{bmatrix} \tag{3.14}$$

where X_j, Y_j, and Z_j denote the colors of the reference chart, and X'_j, Y'_j, and Z'_j are those of the color patches in the chart image. M_{Crr} is the transformation matrix which maps the colors of the image into those of the reference colors, which is estimated by SVD as follows:

$$\begin{bmatrix} X_1 \\ X_2 \\ ... \\ X_N \end{bmatrix} = \begin{bmatrix} X'_1 & Y'_1 & Z'_1 \\ X'_2 & Y'_2 & Z'_2 \\ & ... & \\ X'_N & Y'_N & Z'_N \end{bmatrix} \begin{bmatrix} m_{11} \\ m_{12} \\ m_{13} \end{bmatrix} \tag{3.15}$$

$$\begin{bmatrix} Y_1 \\ Y_2 \\ ... \\ Y_N \end{bmatrix} = \begin{bmatrix} X'_1 & Y'_1 & Z'_1 \\ X'_2 & Y'_2 & Z'_2 \\ & ... & \\ X'_N & Y'_N & Z'_N \end{bmatrix} \begin{bmatrix} m_{21} \\ m_{22} \\ m_{23} \end{bmatrix} \tag{3.16}$$

$$\begin{bmatrix} Z_1 \\ Z_2 \\ ... \\ Z_N \end{bmatrix} = \begin{bmatrix} X'_1 & Y'_1 & Z'_1 \\ X'_2 & Y'_2 & Z'_2 \\ & ... & \\ X'_N & Y'_N & Z'_N \end{bmatrix} \begin{bmatrix} m_{31} \\ m_{32} \\ m_{33} \end{bmatrix} \tag{3.17}$$

The M_{Crr} matrix is embedded in the profile.

3.4.2 Profile application

In the profile application process the image colors are corrected by the relationship acquired in the profile creation process. The workflow is depicted in Figure 3.21 and represents the inverse from the profile connection space: the image is first pre-corrected: the coefficients gathered in the brightness compensation step are applied to the image pixels and the minimum brightness intensity is subtracted, then the pixels are multiplied by the ratios stored in the white balancing correction and the functions stored in the gamma correcion and saturation enhancement are also applied. Afterwards, the tone reproduction is applied to the color of the input image. And the color is corrected by the matrix embedded in the created color profile. The calibrated image is converted back to the RGB color space and stored.

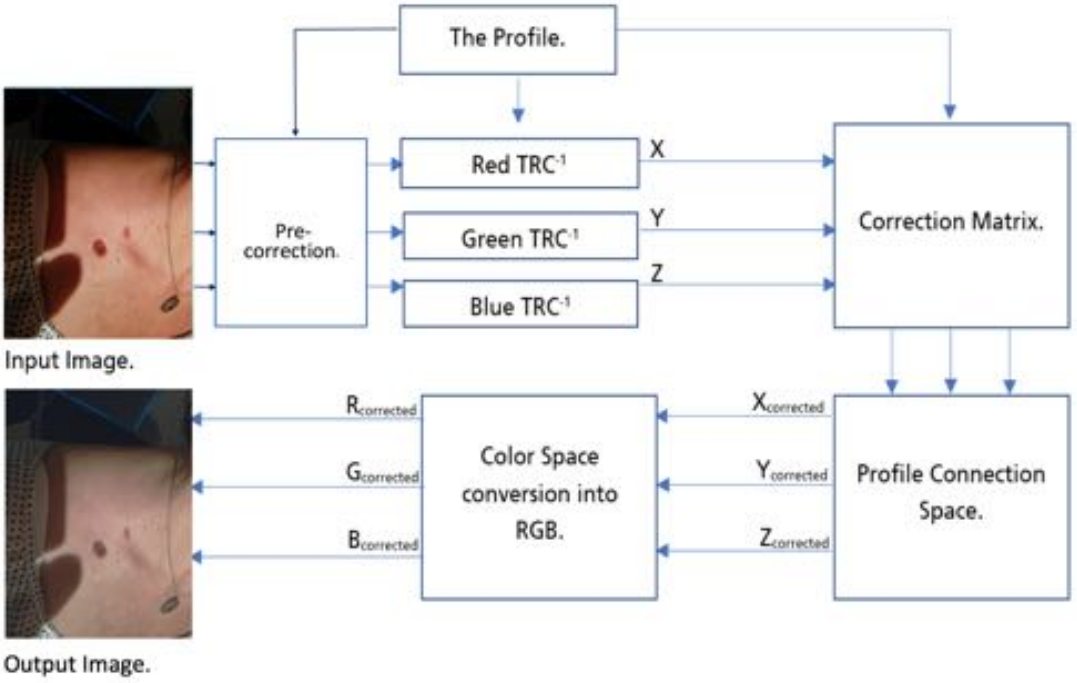

Figure 3.21: Profile application process.

3.5 Android implementation

This system was developed in C++ with resource to the OpenCV library. However, as the objective of this thesis was to develop a mobile solution that would calibrate color, this system was then implemented in an android application.

To perform this step, the code was passed to the application with resource to android

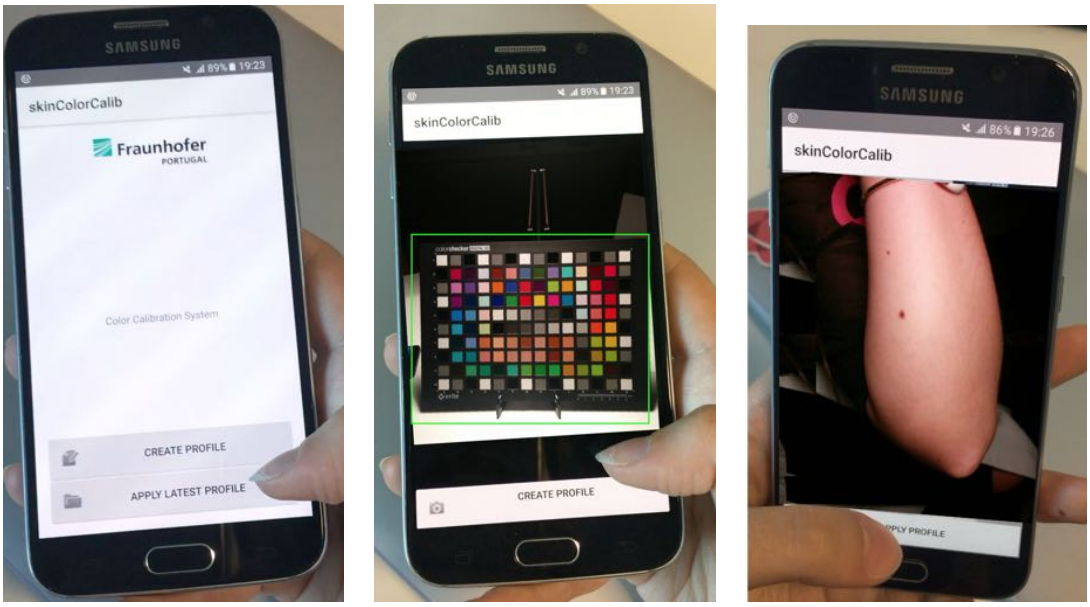

(a) Mobile application welcoming activity.

(b) Mobile application profile creation activity.

(c) Mobile application profile application activity.

Figure 3.22: mSkinColorCalib developed application.

native development kit (NDK) which allows to implement parts of the app in native code, in this case in C++ language, and OpenCV software development kit (SDK) which enables the development of Android applications with use of OpenCV library.

The profile creation process requires the color chart detection to be executed. In turn, the color chart detection to be executed requires a query image and a mask to be available in the system, thus both these images were saved in the application's assets and loaded to cache when the profile creation function was called. Moreover, the JSON files with the relationship between the camera colors and the ground truth colors of the chart are stored in the external memory of the mobile device in the profile creation process, whereas the profile application process reads those files from the external memory.

The application developed consists of three main activities: the welcome activity, which allows to select between profile creation and last profile created application, (Figure 3.22a) the profile creation activity, where the chart is captured and a profile is created (Figure 3.22b) and a profile application activity, in which the last saved profile is used to calibrate images acquired in this activity (Figure 3.22c).

To calibrate skin lesion images with this system the first step is to create a profile in the same conditions as those of the skin lesion images' acquisition, thus the normal

first operation is to press the profile creation button. Then, the mobile device camera opens. The system first reads the mobile devices' model in which the application is being used and if the mobile phone is one of the tested in the pre-acquisition processing stage, the acquisition settings are set to those obtained as the optimal parameters for those models, otherwise the settings are the default ones.

Figure 3.22b shows the profile creation activity in which the camera is overlapping with a green rectangle and a text view with the indication to position the color chart in the centre of the green rectangle. When the acquisition button is pressed, a progress bar is shown with the information depicted in Figure 3.23 while in background the system performs the color chart detection, color patches extraction, color chart pre-correction steps, TRCs estimation, color space conversion and the chromatic transformation. The color chart creation process saves to external memory the color chart before and after the application of the calibration correction.

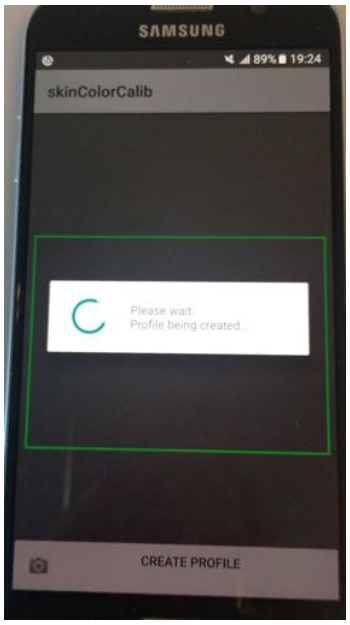

Figure 3.23: Message shown to the user in profile creation process.

Moreover, 4 JSON files with the information of the relationship between acquired and ground truth colors are also saved to external memory: one JSON file with information concerning the brightness map; one with information concerning the remaining pre-correction steps; one containing the 1-D lookup tables from TRC estimation; and one with the correction matrix computed from the chromatic transformation.

When all the previously mentioned files are stored, the profile is created and a dialog fragment is shown with a message to the user, Figure 3.24. If the "PROCEED" to

apply profile button is pressed, the profile application activity is started.

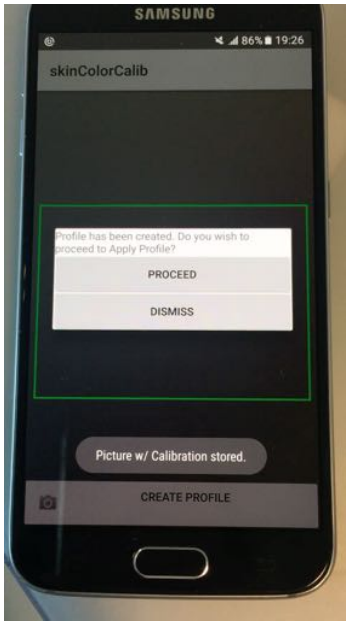

Figure 3.24: Dialog fragment shown to the user after profile creation.

The profile application activity is shown in Figure 3.22c. As in the previous activity, when the acquisition button is pressed a progress bar also appears with the same information, while in background the system performs the pre-corrections of the skin lesion, the TRC mapping and, finally, the chromatic transformation. Posterior to the profile application process both image before and after calibration are stored to the external storage and a new image with the same profile can be acquired.

3.6 Test and evaluation

3.6.1 Pre-acquisition processing

Three mobile phones were tested in the pre-acquisition processing: Samsung S6, Nexus 5x and HTC One M8.

The tested values for each mobile device are shown in Table 3.2. Even though all settings were compared not all correspondent images were acquired, images which had color differences visible to the naked eye, were empirically excluded.

As explained in Section 3.3, color chart detections and color extraction were performed in the acquired images with the different devices. Then, the color difference

Table 3.2: Tested settings for the 3 mobile devices.

	ISO	AE	AWB	Sharpness	Noise	AF
Samsung S6	200; 800;1600;4800	-4; -3: -2; -1; 0; 1; 2; 3; 4	Off Auto Incandescent Fluorescent Warm Fluorescent Daylight Cloudy daylight Twilight Shade	Off Fast High Quality Minimal Zero Shutter Lag	Off Fast High Quality Minimal Zero Shutter Lag	Off Auto Macro Continuous Picture
Nexus 5X	200;800;1600;4800	-12; -10; -8; -6; -4; -2; 0; 2; 4; 6; 8; 10; 12	Off Auto Incandescent Fluorescent Warm Fluorescent Daylight Cloudy daylight Twilight Shade	Off Fast High Quality Minimal Zero Shutter Lag	Fast High Quality Minimal Zero Shutter Lag	Off Auto Macro Continuous Picture
HTC One M8	200; 400; 800; 1600	-2; -1; 0; 1; 2	Off Auto Incandescent Fluorescent Daylight Cloudy daylight	Off Fast	Off Fast	Off Auto Macro

of each patch was estimated with the ΔE_{ab} color difference formula, and the average of the color difference of every patch was calculated. For each mobile device, the minimum average of the color difference was found and the camera settings that originated this value were set to the optimal parameters for acquisition in this system.

3.6.2 Post-acquisition processing

To evaluate the performance of the developed system, two sets of experiments were conducted.

The first experiment was carried under five lighting sources with different color temperatures: 2200 Kelvin(K), 2800K, 3000K, 4000K, 6500K and three different mobile phone devices: Samsung S6, Nexus 5X and HTC One M8. This set of experiments is from now on referred to as Experiment 1 or Exp1 and was performed with the objective to evaluate the calibration system's performance under different color temperatures. Figure 3.25 shows the acquisition set-up in which the images were acquired. Lamps with different light temperatures were used to change the light conditions.

The second experiment was conducted under arbitrary light conditions, with the

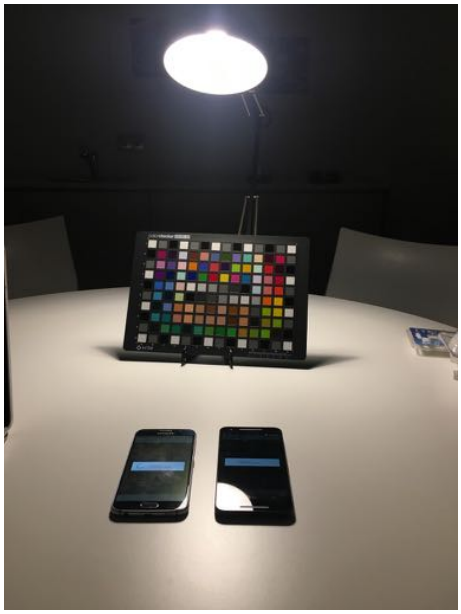

Figure 3.25: Experiment 1's color chart acquisition set-up.

same 3 mobile phones, with the objective of evaluating the system in its normal use conditions. This set of experiments is from now on referred to as Experiment 2 or Exp2.

Both Experiment 1 and Experiment 2 evaluated the system's ability to approximate the acquired colors to the ground truth colors of the chart, which is denominated as the "Ground truth comparison". This evaluation is performed through the average of the ΔE_{ab} color difference of every patch, which is considered as the accuracy of this system. The accuracies of this system obtained under both known and arbitrary light conditions are compared to the results obtained in the literature.

Moreover, Experiment 1 and Experiment 2 also evaluated the ability of the system to calibrate skin lesion images, which is denominated as "Skin lesions comparison". To evaluate the performance of the system in this context, the mean and standard deviation of the color of both lesion and skin are extracted, before and after calibration. Afterwards, 3 situations are evaluated in Experiment 1, whereas in Experiment 2 only Situation 1 is evaluated. The situations are the following:

- Situation 1 - calculation of the mean and standard deviation of both the lesion's color and skin's color, among the 3 different mobile phone devices, but in the same light condition, before and after calibration;
- Situation 2 - calculation of the mean and standard deviation of both the lesion's color and skin's color, among the different light conditions but the same mobile phone device, before and after calibration;

- Situation 3 - calculation of the mean and standard deviation of both the lesion's color and the skin's color, among the different lighting conditions and the different mobile devices, before and after calibration.

Situation 1 was performed with the objective to test if the system is able to minimize the color differences when different mobile phones were used for the acquisition. On the other hand, situation 2 aims to prove the system minimizes color differences when the acquisitions is performed under different lighting conditions. Finally, the parameters in situation 3 were calculated with the objective to evaluate if the system minimizes color differences independently to the lighting conditions and mobile device used for acquisitions.

In Exp 1, the average of the standard deviation values obtained in Situation 3 for all skin lesion images acquired is considered as a measure of the applicability of this system to the color calibration of skin lesion images since it provides the comparison between the amount of color variations between images acquired with different devices under different light conditions. Whereas in Exp 2, the average of the standard deviation values obtained in situation 2 is considered as the measure of this system's applicability to the calibration of skin lesion images under arbitrary light conditions, since it provides the comparison between the amount of color variations between images acquired with different devices under arbitrary light conditions.

In Experiment 1, 10 skin lesion images were acquired in 3 different sets of acquisition. Thus, 3 color profiles were created for each mobile phone. The color charts created in the profile creation process were used to calculate the accuracy of the system in the "Ground truth comparison" section. The 10 skin lesions images were used to calculate this system's ability to calibrate skin lesion images under known light conditions in the "Skin lesions comparison" Section.

On the other hand, in Experiment 2, 100 color charts were acquired under arbitrary light conditions and those charts were used to calculate the accuracy of the system in the "Ground truth comparison" section. 10 skin lesions were also acquired under arbitrary light conditions and used to calculate this system's ability to calibrate skin lesion images under aribtrary light conditons in the "Skin lesions comparison" Section. In Exp2, the average of the standard deviation values obtained in Situation 1 for all skin lesion images acquired is considered as the measure of applicability of this system to calibrate skin lesion images.

The segmentation of both skin and lesion from skin lesion images acquired was performed manually. In order to assure that the amount of pixels extracted was

representative of the full sample, cropped skin images were not accepted with less than 5000 pixels, whereas lesion images were not accepted when inferior to 3000 pixels. In both Experiments 1 and 2, the skin and lesion's color was extracted in the CIE LAB color space, since RGB is not perceptually uniform. Each of the LAB components presented were scaled to the range of [0,255].

4

Results

This chapter presents the performance results for the color calibration of mobile acquired skin lesion images system developed. In the first section, the results for the pre-acquisition processing are presented and the optimal settings that were implemented in the post-acquisition stage are introduced. Afterwards, the performance of the calibration system is presented, which is divided in Experiment 1, Experiment 2 and a subsection regarding the computation time of the system developed. Both Experiment 1 and 2 are divided in a Ground truth comparison section, and a Skin lesion comparison section. The computation time subsection contains an assessment on the time length of the proposed algorithm for each calibration task.

4.1 Pre-acquisition processing

This section's objective was to acquire the optimal acquisition settings for each mobile phone. Even though for some parameters the acquired color chart images were visually different from the real colors, for other set of parameters the changes were almost imperceptible. Figure 4.1 shows an example of 2 images acquired with different settings with Samsung S6 in which the differences are almost imperceptible.

Samsung S6, Nexus 5X and HTC One M8 mobile devices are from now on referred to as S6, 5X and HTC, respectively.

Figure 4.1: Two images acquired with different settings.

Thus, for each color chart image acquired the minimum average of the ΔE_{ab} color difference was calculated as described in Section 3.3. Figure 4.2 shows the color charts that originated the minimum ΔE_{ab} color differences achieved. The minimum average color differences achieved were $\Delta E_{ab} = 10.50$, $\Delta E_{ab} = 12.25$ and $\Delta E_{ab} = 11.36$, respectively for S6, 5X and HTC.

(a) Color chart acquired with S6. **(b)** Color chart acquired with 5X. **(c)** Color chart acquired with HTC.

Figure 4.2: Charts acquired with the optimal settings for the different mobile devices.

On the other hand, Table 4.1 shows the settings with which the color charts in Figure 4.2 were acquired. These parameters were set as the acquisition settings in the post-acquisition processing.

Table 4.1: Optimal settings for image acquisition.

Mobile device	AWB mode	ISO level	Exposure level	AF mode	Edge mode	Noise Reduction mode
Samsung S6	Incandescent	800	2	Continuous Picture	Fast	Fast
Nexus 5x	Fluorescent	200	2	Continuous Picture	Fast	Fast
HTC One M8	Twilight	400	0	Continuous Picture	Fast	Fast

4.2 Post-acquisition processing

The post-acquisition processing results are divided in Experiment 1 and Experiment 2. As explained in Section 3.6.2, Experiment 1 is conducted under five different lighting sources, whereas Experiment 2 was conducted under arbitrary light conditions. Both these experiments were evaluated in the three mobile phones used in the previous stage.

In both experiments the performance of the calibration system is evaluated according to the approximation of the acquired colors to the ground truth colors of the chart, in

the "Ground truth comparison" Section. Moreover, the applicability of the system to skin lesion images is also studied, in the "Skin lesion comparison" Section.

4.2.1 Experiment 1

Experiment 1 is divided in 2 sections: Section 4.2.1.1 which corresponds to the ground truth comparison, and Section 4.2.1.2 which corresponds to the skin lesion comparison.

4.2.1.1 Ground truth comparison

The results for one of the profile creation processes are shown in Table 4.3 where each row represents a different color temperature and each column represents a diferent mobile device. The three first columns depict the color charts acquired with the different mobile devices before calibration (columns entitled "PRO"), whereas the last three columns show the same color charts after calibration applied (columns entitled "POS"). The remaining tables shown in Exp.1 present the same format. The color differences between the acquired charts and ground truth colors are represented in below each image.

Table 4.2 shows the average of the color differences for the total charts stored along the profile creation processes in Exp 1.

Table 4.2: Average of the color differences for the color charts obtained in 4.2.1.

T(K)	ΔE_{ab} S6 PRE	ΔE_{ab} 5X PRE	ΔE_{ab} HTC PRE	ΔE_{ab} S6 POS	ΔE_{ab} 5X POS	ΔE_{ab} HTC POS
2200	21,52	22,30	17,44	9,45	9,77	9,73
2800	22,17	23,28	15,65	9,10	8,68	7,75
3000	20,57	19,81	14,96	8,39	9,73	8,48
4000	16,38	19,24	13,90	8,25	9,05	8,28
6500	15,67	18,92	12,99	8,30	9,05	7,98

Through the assessment of Table 4.2 some conclusions can be achieved. First of all, the system created calibrates color in all lighting conditions and for each mobile phone, since for all the situations presented the color difference is smaller for the calibrated charts.

Moreover, these results show that the calibration performance does not improve with a particular light source, thus the system is independent from the lighting conditions. Table 4.2 also suggested that the HTC mobile device had better calibration performances given that it achieved smaller ΔE_{ab} color differences. In Chapter 5, these results are compared to those of the literature.

Table 4.3: Color charts stored in the profile creation process.

T (K)	PRE S6	PRE 5X	PRE HTC	POS S6	POS 5X	POS HTC
2200	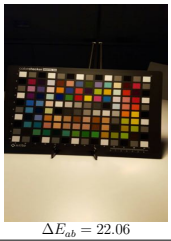 $\Delta E_{ab} = 22.06$	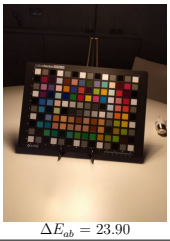 $\Delta E_{ab} = 23.90$	$\Delta E_{ab} = 18.44$	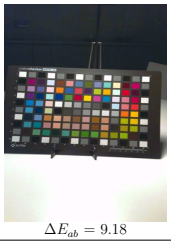 $\Delta E_{ab} = 9.18$	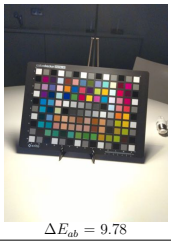 $\Delta E_{ab} = 9.78$	$\Delta E_{ab} = 9.99$
2800	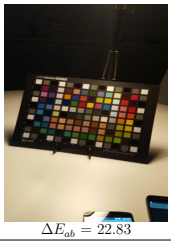 $\Delta E_{ab} = 22.83$	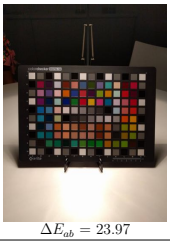 $\Delta E_{ab} = 23.97$	$\Delta E_{ab} = 15.62$	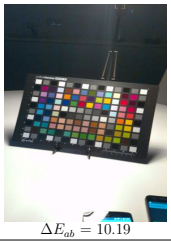 $\Delta E_{ab} = 10.19$	$\Delta E_{ab} = 9.09$	$\Delta E_{ab} = 7.90$
3000	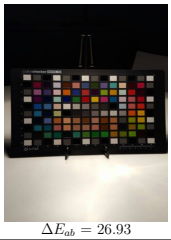 $\Delta E_{ab} = 26.93$	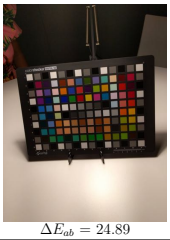 $\Delta E_{ab} = 24.89$	$\Delta E_{ab} = 16.59$	$\Delta E_{ab} = 8.23$	$\Delta E_{ab} = 10.08$	$\Delta E_{ab} = 8.64$
4000	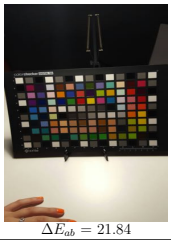 $\Delta E_{ab} = 21.84$	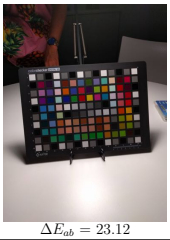 $\Delta E_{ab} = 23.12$	$\Delta E_{ab} = 16.70$	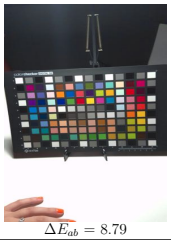 $\Delta E_{ab} = 8.79$	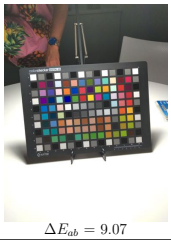 $\Delta E_{ab} = 9.07$	$\Delta E_{ab} = 8.41$
6500	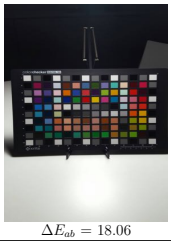 $\Delta E_{ab} = 18.06$	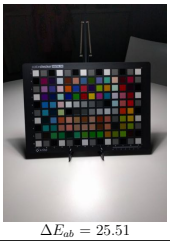 $\Delta E_{ab} = 25.51$	$\Delta E_{ab} = 14.69$	$\Delta E_{ab} = 8.32$	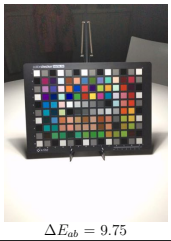 $\Delta E_{ab} = 9.75$	$\Delta E_{ab} = 8.40$

4.2.1.2 Skin lesions comparison

Table 4.4 represents the average of the standard deviations obtained in Situation 3 for the 10 skin lesion images, before and after calibration. This value represents the measure of the applicability of this system to the color calibration of skin lesion images under different light conditions and with different mobile devices. $\bar{\sigma}_X$ represents the average of the standard deviations, where X stands for each of the LAB components, which are calculated for both lesion and skin, before and after calibration.

Table 4.4: Average standard deviations obtained in Situation 3 for the 10 skin lesion images.

		PRE	POS
Lesion	$\bar{\sigma_L}$	3,71	2,89
	$\bar{\sigma_a}$	1,51	1,00
	$\bar{\sigma_b}$	1,74	1,26
Skin	$\bar{\sigma_L}$	5,06	3,85
	$\bar{\sigma_a}$	1,82	1,70
	$\bar{\sigma_b}$	2,34	1,74

The average results show that the system decreases the amount of color variation of images acquired under different mobile devices and under different lighting conditions given that the average of the standard deviation decreases posterior to the calibration being applied. Moreover, they show that there is an increased variability in the L values, when compared to the a and b channels, especially for skin colors.

Evaluations of Situations 1, 2 and 3 are shown for 2 lesions. The remaining images acquired in this set of experiments, as well as their respective results for Situation 3, are presented in Appendix C.1.

Hence, Tables 4.5 and 4.6 show 2 lesions before and after calibration, for each mobile device and for each color temperature. The first lesion presented is from now on mentioned as Lesion 01 and the second as Lesion 02. These 2 examples are shown because the calibration performed in Lesion 01 represents an example of a calibration well performed, whereas Lesion 02 represents a case in which the developed system faced difficulties.

Table 4.5: Lesion 01 before and after calibration for each mobile device and each color temperature.

T (K)	PRE S6	PRE 5X	PRE HTC	POS S6	POS 5X	POS HTC
2200	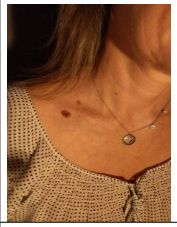			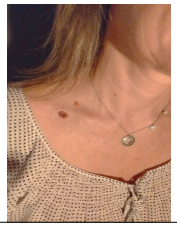	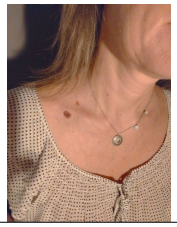	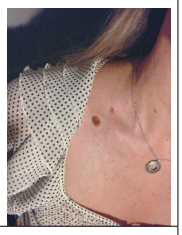
2800	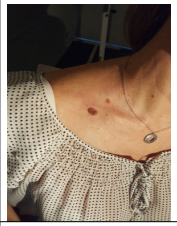			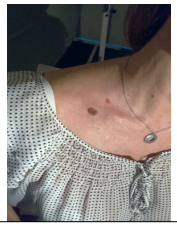		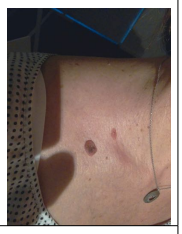
3000				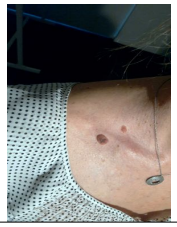		
4000	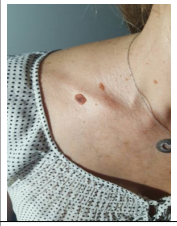		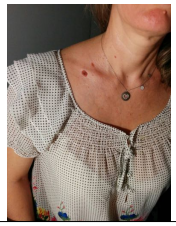			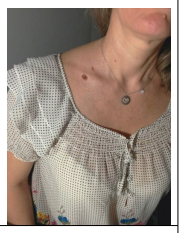
6500			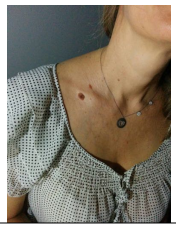	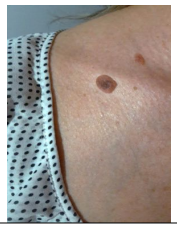	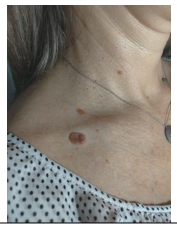	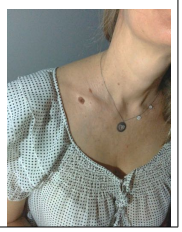

Table 4.6: Lesion 02 before and after calibration for each mobile device and each color temperature.

T (K)	PRE S6	PRE 5X	PRE HTC	POS S6	POS 5X	POS HTC
2200					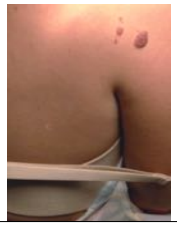	
2800						
3000						
4000						
6500						

Through the visual observation of Tables 4.5 and 4.6 it is possible to discern improvements in images posterior to the profile application process.

Figure 4.3 represents the evaluation of Lesion 01 in Situation 1. This evaluation is shown in the form of an error bar graph for each of the LAB components. Thus, 4.3a represents the "L" component, whereas 4.3b represents the "a" channel, and finally 4.3c represents the "b" channel. In each of these figures, blue color stands for the values acquired for skin before calibration, orange represents the values for skin after calibration, yellow stands for the lesion before calibration and purple represents the lesion after calibration.

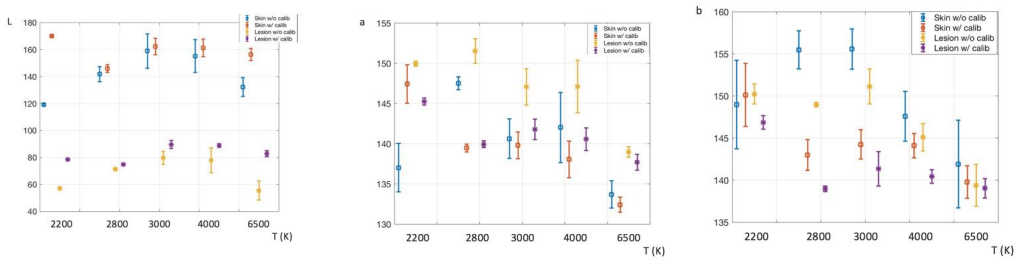

(a) Evaluation of Lesion 01 in Situation 1 in L channel.

(b) Evaluation of Lesion 01 in Situation 1 in a channel.

(c) Evaluation of Lesion 01 in Situation 1 in b channel.

Figure 4.3: Evaluation of Lesion 01 in Situation 1. (a) channel L; (b) channel a; (c) channel b. Blue represents skin without calibration; Orange represents skin with calibration; Yellow represents lesion before calibration; Purple represents lesion after calibration.

These results show that the mean LAB colors across the different mobile devices after profile applied have smaller standard deviations than those of the mean LAB colors across different devices before the profile was applied, for each of the color temperatures tested and for each of the channels. Furthermore, the L channel observation showed that the variability of the mean value with temperature decreases after calibration, turning the L values more homogeneous. Moreover, it can also be observed that the L channel presents a clear distinction between the skin colors and the lesion colors, as opposed to the a and b channels, which present minor variations and no apparent differences between lesion and skin colors. For this reason, only the L value is shown in following analysis.

Despite the fact that results suggest the system to decrease standard deviations of the average colors acquired with multiple devices, a few cases showed to have larger standard deviations after the profile was applied rather than before application. One example is the calibration of Lesion 02's skin color under a 6500K color temperature light. Figure 4.4 represents the evaluation of Situation 1 in Lesion 02 for the L channel.

As it can be observed, at a color temperature of 6500K, the standard deviations of the average colors acquired with multiple devices after profile being applied show increased values when compared to those before profile being applied. Even though this calibration error has occurred, the standard deviations for the remaining temperatures are all smaller when calibration is applied. Moreover, the variability of the mean L values with temperature also decreases. Figure 4.5 shows, in more detail, the two lesions for which the system faces problems in the calibration. Figures 4.5a

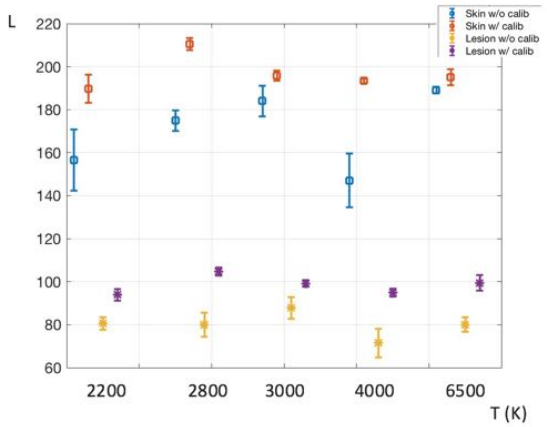

Figure 4.4: Evaluation of Lesion 02 in Situation 1 in L channel.

and 4.5b show Lesion 02 acquired by S6 under a color temperature of 6500K. On the other hand, Figures 4.5c and 4.5d show Lesion 06 acquired with 5X under a color temperature of 2200K, before and after calibration.

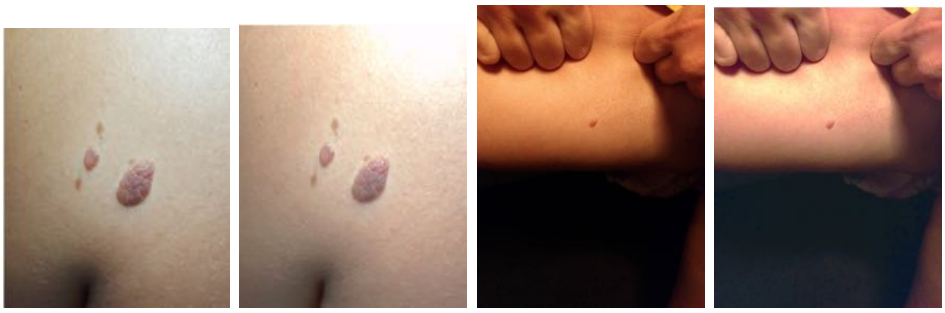

(a) Lesion 02 before profile applied.

(b) Lesion 02 after applied.

(c) Lesion 06 before profile applied.

(d) Lesion 06 after profile applied.

Figure 4.5: Calibration errors. Figures (a) and (b) represent Lesion 01 before and after the profile was applied. Figures (c) and (d) represent Lesion 06 before and after profile was applied.

Figure 4.6 shows the evaluation of Situation 2 for Lesions 01 and 02. The top row corresponds to Lesion 01, whereas the bottom row corresponds to Lesion 02 and the columns represent the L, a and b channels, respectively.

The assessment of Situation 2 shows similar results to those of Situation 1: smaller standard deviations are achieved when the profile is applied to skin lesion images. It can also be observed that, even though there was a calibration error when applying the developed system in Lesion 02 with S6 under 6500K, the standard deviation of the average colors acquired under the 5 different lighting conditions with S6 are nonetheless smaller after calibration is performed. The variability of the mean L val-

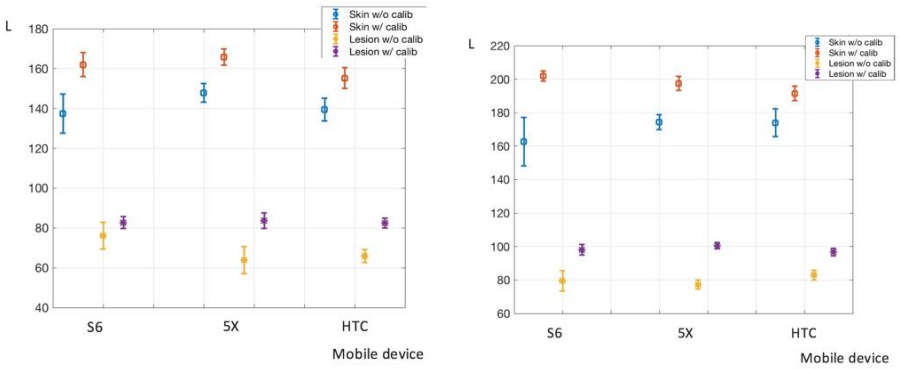

(a) Evaluation of Lesion 01 in Situation 2 in L channel.

(b) Evaluation of Lesion 02 in Situation 2 in L channel.

Figure 4.6: Evaluation of Lesions 01 and 02 in Situation 2 in L channel. (a) Lesion 01, channel L; (b) Lesion 02, channel L. Blue represents skin without calibration; Orange represents skin with calibration; Yellow represents lesion before calibration; Purple represents lesion after calibration.

ues across mobile devices also shows decreased values when calibration is performed, especially for lesion colors.

Finally, the performances obtained for Situation 3 concerning Lesions 01 and 02 are presented in Tables 4.7 and 4.8, respectively. These tables represent the mean LAB colors and standard deviations across all lighting conditions and all mobile devices. The first columns represent the values acquired before color profile was applied, whereas the second column represents the values after color profile was applied.

Table 4.7: Evaluation of Lesion 01 in Situation 3.

		PRE	POS
Lesion	$\bar{L} \pm \sigma_L$	68,30±3,46	82,93±1,68
	$\bar{a} \pm \sigma_a$	146,95±1,36	141,06±0,76
	$\bar{b} \pm \sigma_b$	146,99±1,32	141,35±0,89
Skin	$\bar{L} \pm \sigma_L$	147,87±4,23	161,02±3,37
	$\bar{a} \pm \sigma_a$	142,68±1,81	139,45±1,44
	$\bar{b} \pm \sigma_b$	152,78±2,46	144,27±1,24

Table 4.8: Evaluation of Lesion 02 in Situation 3.

		PRE	POS
Lesion	$\bar{L} \pm \sigma_L$	79,92±2,33	98,43±1,39
	$\bar{a} \pm \sigma_a$	144,96±1,66	144,43±0,82
	$\bar{b} \pm \sigma_b$	144,31±2,14	137,88±1,16
Skin	$\bar{L} \pm \sigma_L$	170,35±5,55	196,96±2,37
	$\bar{a} \pm \sigma_a$	140,20±2,58	138,16±1,77
	$\bar{b} \pm \sigma_b$	153,13±3,31	146,61±1,85

The assesment of Tables 4.7 and 4.8 showed that when the color profile created by the system is applied, the 10 skin lesion images acquired across different mobile phones and different light conditions had smaller standard deviations when compared to skin lesion images acquired under different light conditions and different mobile phones, without the color profile application, even for the case when calibration errors occurred.

Figure 4.7 shows Lesion 01's segmentation as an example of the manual segmentation

performed on lesion images. Concerning the skin segment extracted from images to evaluate its color, an attempt of cropping the same segment through the various acquisitions was made. The mean color values for the L channel extracted from each of the images is also provided in Figure 4.7.

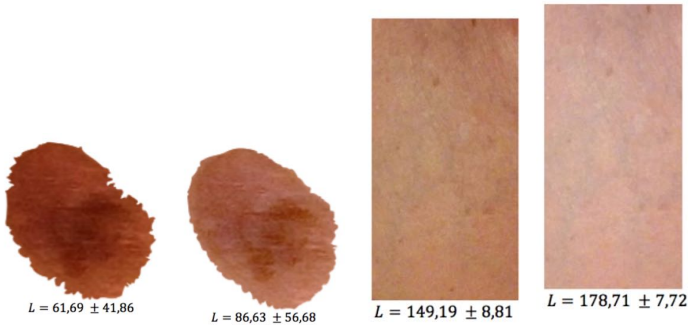

(a) Lesion segmentation before calibration. **(b)** Lesion segmentation after calibration. **(c)** Skin segmentation before calibration. **(d)** Skin segmentation after calibration.

Figure 4.7: Example of the lesion segmentation performed.

As can be observed, the extracted colors revealed to have large standard deviation values. Moreover, those standard deviations increase with color calibration. This fact was attributed to the unevenness of skin. Figure 4.8 shows Lesion 13, an example in which the skin's surface is irregular, causing visible color differences. It is also possible to observe that Figure 4.8b, which represents Lesion 13 after calibration, has a more clear distinction between veins and skin.

4.2.2 Experiment 2

Similarly to Experiment 1, Experiment 2 is also divided in 2 Sections: Section 4.2.2.1 which corresponds to the ground truth comparison, and Section 4.2.2.2 which corresponds to the skin lesion comparison.

4.2.2.1 Ground truth comparison

As mentioned before, 100 color charts were acquired under arbitrary light conditions with each mobile phone, Samsung S6, Nexus 5X and HTC One M8. Table 4.9 represents the average ΔE_{ab} color differences achieved across the 100 color charts acquired with each mobile device. These values are considered as the performance of the system under arbitrary light conditions. Thus, the performance of the system,

(a) Lesion 13 before calibration.

(b) Lesion 13 after calibration.

Figure 4.8: Irregular skin surface of Lesion 13.

under arbitrary conditions, for the Samsung S6 was 6,37, whereas for 5X was 6,15 and, finally, for HTC the performance obtained was 5,84 was achieved.

Table 4.9: System performance under arbitrary light conditions.

	S6	5X	HTC
ΔE_{ab}	6,37	6,15	5,84

The performances obtained under arbitrary light conditions are compared to the results obtained in the literature in Chapter 5.

Table 4.10 shows 3 examples of color charts acquired under arbitrary light conditions for each mobile phone, before and after color calibration is applied. The color differences between each chart and ground truth colors are also presented in Table 4.10.

Table 4.10: Examples of charts acquired under arbitrary light conditions before and after calibration for each mobile phone device.

	Example 1		Example 2		Example 3	
	PRE	POS	PRE	POS	PRE	POS
S6	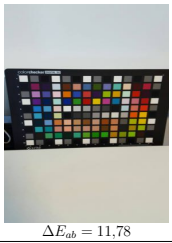 $\Delta E_{ab} = 11{,}78$	$\Delta E_{ab} = 7{,}12$	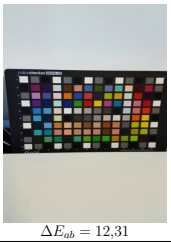 $\Delta E_{ab} = 12{,}31$	$\Delta E_{ab} = 7{,}11$	$\Delta E_{ab} = 17{,}56$	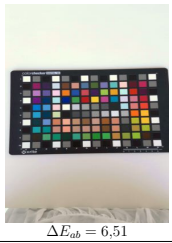 $\Delta E_{ab} = 6{,}51$
5X	$\Delta E_{ab} = 12{,}56$	$\Delta E_{ab} = 7{,}55$	$\Delta E_{ab} = 14{,}74$	$\Delta E_{ab} = 5{,}61$	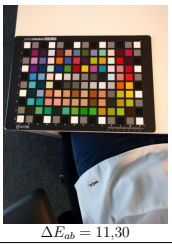 $\Delta E_{ab} = 11{,}30$	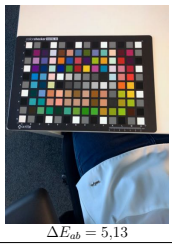 $\Delta E_{ab} = 5{,}13$
HTC	$\Delta E_{ab} = 14{,}24$	$\Delta E_{ab} = 6{,}04$	$\Delta E_{ab} = 17{,}54$	$\Delta E_{ab} = 6{,}87$	$\Delta E_{ab} = 17{,}54$	$\Delta E_{ab} = 6{,}87$

4.2.2.2 Skin lesions comparison

Table 4.11 shows the average of the standard deviations obtained in Situation 1 for all the 10 skin lesion images acquired under arbitrary conditions. This value represents the measure of the applicability of this system to the color calibration of skin lesion images under arbitrary light conditions, with different mobile devices.

Table 4.11: Average standard deviations obtained in Situation 1 for the 10 skin lesion images acquired under arbitrary light conditions.

		PRE	POS
Lesion	$\bar{\sigma_L}$	8,46	5,53
	$\bar{\sigma_a}$	1,66	1,16
	$\bar{\sigma_b}$	2,47	1,26
Skin	$\bar{\sigma_L}$	7,99	5,40
	$\bar{\sigma_a}$	2,14	1,63
	$\bar{\sigma_b}$	3,65	2,85

The average results show that the standard deviation under arbitrary conditions decreases after the calibration is performed under arbitrary conditions. Moreover, these results also suggest that the L values are more susceptible to changes, given

that the average standard deviations for the L channel is higher that for the a and b channels. Finally, the comparison of Table 4.11 with Table 4.4 also shows higher average standard deviations for the results obtained in Experiment 2.

The assessment of Situation 1 for 2 of the skin lesion images acquired are shown. The remaining images acquired in Experiment 2 are presented in Appendix D.1, as well as the results for Situation 1 for each of them.

Thus, Tables 4.12 and 4.13 represent 2 of the skin lesion images acquired in this set of experiments under arbitrary light conditions. The columns represent the different mobile devices, whereas the rows represent images before and after calibration. These skin lesion images are from now on referred to as Lesion 11 and Lesion 12.

Table 4.12: Lesion 11 before and after calibration for each mobile device.

	S6	5X	HTC
PRE			
POS		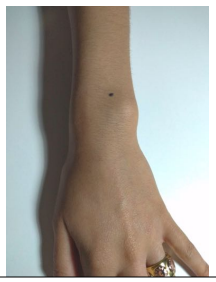	

Table 4.13: Lesion 12 before and after calibration for each mobile device.

	S6	5X	HTC
PRE			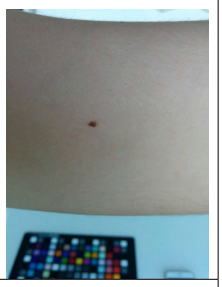
POS	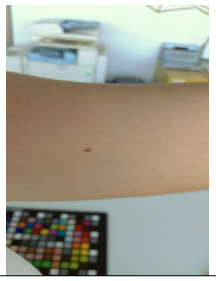		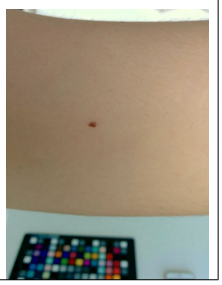

On the other hand, Tables 4.14 and 4.15 represent the analysis of Lesions 11 and 12 for Situation 1. The results obtained for Situation 1 for both Lesions 11 and 12, also show decreased standard deviations for calibrated images acquired across different mobile devices than the images before calibration applied.

Table 4.14: Evaluation of Lesion 11 in Situation 1.

		PRE	POS
Lesion	$\bar{L} \pm \sigma_L$	35,42 ±10,15	68,08 ± 6,33
	$\bar{a} \pm \sigma_a$	129,32 ± 0,42	129,37 ± 0,39
	$\bar{b} \pm \sigma_b$	131,44 ± 1,98	132,35 ±1,83
Skin	$\bar{L} \pm \sigma_L$	119,12 ± 12,27	141,43 ± 6,25
	$\bar{a} \pm \sigma_a$	137,04 ± 1,75	136,15 ± 1,27
	$\bar{b} \pm \sigma_b$	148,99 ± 3,19	145,81 ± 0,36

Table 4.15: Evaluation of Lesion 12 in Situation 1.

		PRE	POS
Lesion	$\bar{L} \pm \sigma_L$	42,14 ± 3,04	51,76 ± 1,99
	$\bar{a} \pm \sigma_a$	137,01 ± 1,15	136,88 ± 0,97
	$\bar{b} \pm \sigma_b$	134,28 ± 1,38	138,45 ± 1,07
Skin	$\bar{L} \pm \sigma_L$	119,00 ± 6,76	133,55 ± 3,98
	$\bar{a} \pm \sigma_a$	128,76 ± 0,61	134,01 ± 0,33
	$\bar{b} \pm \sigma_b$	130,98 ± 1,47	144,60 ± 1,06

The results obtained in Tables 4.14 and 4.15 also show decreased standard deviations for calibrated images acquired with different mobile devices when compared to those of images acquired with different mobile devices before calibration.

4.2.3 Computation time

The normal use case of the developed system involves creating and applying a profile. While this system takes 50s to create the profile and 35s to apply the profile when the algorithm is ran on a computer, when the system was implemented in mobile devices, the time consumption increased.

Table 4.16 shows the time required for both profile creation and profile application processes in the three mobile devices. The difference between profile creation process and profile application process resides essentially in the TRC coefficients: whereas in the profile creation process the algorithm applies computationally demanding pixel to pixel operations, in the profile applicaton process an array indexing operation is performed through LUT, which in this system constitutes a saving in terms of processing time of 50%.

Table 4.16: Computation time across the mobile devices.

Mobile device	Δt profile creation (min)	Δt profile application (min)
Samsung S6	1	0,5
Nexus 5x	2	1
HTC One M8	3	1,5

This increase made the process slow and constituted a problem in the skin lesion images acquisition and for mobile devices like HTC, which take three times as long to apply the whole process as compared to Samsung S6, it might make be a concern for implementation in mobile teledermatology applications.

5

Conclusions and Future Work

This project's objective was to develop a computer vision based system to calibrate mobile acquired skin lesion images. As so, an algorithm was developed in C++, with resource to OpenCV library. However, so that the system would calibrate mobile acquired images the system had to be implemented in the android environment, with resource to NDK and OpenCVSDK, and therefore, the objective of developing a system for application in a mobile environment was fulfilled.

The developed system includes a color profile creation process and a profile application process. In the former the image of a color chart is captured and a relationship between the colors of the patches in the captured image and the internal reference colors is estimated. After the estimation the system creates a profile, and embeds the relationship in it. The latter constitutes the inverse operations as those of the profile creation process. For the development of such algorithm, several computer vision techniques were applied, like the automatic detection of the color chart and its patches, the patches color extraction and th color model creation and application itself. Thus, the objective of developing a computer vision based system was also successful.

The performance of the system was evaluated in two sets experiments. Experiment 1 consisted in the evaluation of the system's performance under various known light conditions, whereas the second experiment was performed for arbitrary light conditions. Each of the experiments was evaluated in terms of the system's ability to approximate acquired colors to the reference colors, ground truth comparison, and the system's adaptability to calibrate skin lesion images, skin lesion comparison.

Table 5.1 shows the performances achieved in the ground truth comparison, for Experiment 1. In turn, Table 5.2 shows results obtained in the literature for similar experiments with the objective of comparing the performances obtained with the results in the literature.

Table 5.1: mSkinColorCalib color differences obtained under various color temperatures.

	6500K	4000K	3000K	2800K	2200K
ΔE_{ab} mSkinColorCalib S6	8,30	8,25	8,39	9,10	9,45
ΔE_{ab} mSkinColorCalib 5X	9,05	9,05	9,73	8,68	9,77
ΔE_{ab} mSkinColorCalib HTC	7,98	8,28	8,48	7,75	9,73

Table 5.2: Color differences obtained in [15] and [58] under various color temperatures.

	6500K	4150K	3100K	2856K	2300K
ΔE_{ab} [58]	4,27	6,40	7,25	7,12	10,70
ΔE_{ab} [15]	5,82	6,91	9,01	8,51	14,70

Even though the color temperatures were not exactly the same as the reported in [15,58] and the lighting conditions in our system were more adverse, some conclusions can be made. As it is, the system presents better results than those reported in the literature for color temperatures of 2800K and 2200K. Moreover, for color temperatures of 3000K the results are almost equivalent to those reported in the literature. However, for color temperatures of $\approx$ 4000K and 6500K the developed system performs worse. This lower performances might be explained by the fact that, in [58] and [15], the charts were illuminated by SpectraLight III [55] and are therefore equally illuminated as opposed to the set-up of this system which was evaluated under a lamp which might cause a non uniform lighting of the chart's surface. The comparison of mSkinColorCalib results between the three different mobile devices suggest HTC One M8 to perform better when compared to Samsung S6 and Nexus 5x.

The results of the ground truth comparison for Experiment 2 showed better performances as expected given the uniformity of lighting conditions. Table 5.3 shows the comparison between values obtained and those reported in the literature.

Table 5.3: Color differences obtained in [57] and [60] under arbitrary light conditions.

	ΔE_{ab}
[57] System	6,21
[60] System	$\simeq 5$
mSkinColorCalib S6	6,37
mSkinColorCalib 5X	6,15
mSkinColorCalib HTC	5,84

This comparison suggests that the developed system can approximate acquired col-

ors to the reference colors with performances comparable to those of the literature for each of the mobile devices. Thus, the objective of developing a system that had the ability to approximate the color acquired by a camera phone to the ground truth colors was also successful.

The skin lesion comparison in Experiment 1 was evaluated through the average standard deviations of the average colors captured between different mobile phones under different light conditions. The results suggest that the system decreases the amount of color variation of images acquired under different mobile devices and under different lighting conditions. Moreover, results also suggest that the L channel is the one with the greatest oscillations between images acquired with different mobile devices and/or illumination conditions, and that the system is capable of smoothing this variability making the mean values more homogeneous. Thus, the results suggest this system improves the color values when acquisition parameters, such as mobile device or light conditions, are different. The skin lesion comparison in Experiment 2 showed similar results for the average standard deviations between mobile devices, under arbitrary light conditions, which indicates the system can be used in its normal use conditions.

However, the system faced difficulties because of the non-uniformity of the lighting conditions over the skin lesion which caused some calibrated images to have areas with information loss due to the appearance of white color in skin areas. Although the results suggest the adaptability of this system to calibrate skin lesion images, the aforementioned errors in some calibrated images and the fact that only 10 skin lesion images in each set of experiments were tested, do not allow the assertion with certainty of this adaptability.

Moreover, the developed system faced a computation time problem which may constitute a problem in the feasibility of this system's implementation in mobile teledermatology applications.

In conclusion, the overall objectives of the current project were achieved. Nevertheless, for future work some improvements may be considered. This system's main difficulties are the fact that it is computationally demanding and non-automatic, given the fact that to calibrate a specific scene an image of a color chart must be captured first and only afterwards the scene can be corrected. In a recent study [65] color constancy is casted as an illumination classification problem through deep learning, which would make the system more automatic and practical. However, deep learning is also computationally demanding. Thus, a suggestion is made to study the variance between several profiles created by each mobile device in each

specific light in order to understand if there is any kind of pattern that can be applied as a definitive model for a particular mobile phone and a certain type of light which would solve both time and practicability issued.

Bibliography

[1] M. Lens and M. Dawes, "Global perspectives of contemporary epidemiological trends of cutaneous malignant melanoma," *British Journal of Dermatology*, vol. 150, no. 2, pp. 179–185, 2004.

[2] W. H. Organization, "Skin cancers." `http://www.who.int/uv/faq/skincancer/en/`, 2016. Accessed: 2017-2-20.

[3] L. A. Torre, F. Bray, R. L. Siegel, J. Ferlay, J. Lortet-Tieulent, and A. Jemal, "Global cancer statistics, 2012," *CA: a cancer journal for clinicians*, vol. 65, no. 2, pp. 87–108, 2015.

[4] M. E. Celebi, H. A. Kingravi, B. Uddin, H. Iyatomi, Y. A. Aslandogan, W. V. Stoecker, and R. H. Moss, "A methodological approach to the classification of dermoscopy images," *Computerized Medical Imaging and Graphics*, vol. 31, pp. 362 – 373, 2007.

[5] S. N. de Saúde, "Relatório anual sobre o acesso a cuidados de saúde nos estabelecimentos do sns e entidades convencionadas (2015)." `http://www.acss.min-saude.pt/wp-content/uploads/2016/11/RA_Acesso_2015.pdf`. Accessed: 2017-2-20.

[6] S. C. Foundation, "Skin cancer facts and statistics." `http://www.skincancer.org/skin-cancer-information/skin-cancer-facts#men/women`. Accessed: 2017-2-20.

[7] K. D. H. S. J. J. L. J. e. Longo DL, Fauci AS, *Harrisson's Principles of Internal Medicine*. New York: NY: McGraw-Hill, 18e ed., 2012.

[8] L. Rosado, M. J. M. Vasconcelos, R. Castro, and J. M. R. Tavares, *From Dermoscopy to Mobile Teledermatology*. CRC Press, 2015.

[9] R. Wootton and J. Craig, *Introduction to Telemedicine*. Royal Society of Medicine Press, 1999.

[10] C.-H. Hsieh, H.-H. Tsai, J.-W. Yin, C.-Y. Chen, J. C.-S. Yang, and S.-F. Jeng, "Teleconsultation with the mobile camera-phone in digital soft-tissue injury: A feasibility study," *Plastic and Reconstructive Surgery*, vol. 114, no. 7, 2004.

[11] F. Verhoeven, L. v. Gemert-Pijnen, K. Dijkstra, N. Nijland, E. Seydel, and M. Steehouder, "The contribution of teleconsultation and videoconferencing to diabetes care: A systematic literature review," *Journal of Medical Internet Research (JMIR)*, vol. 9, 2007.

[12] S. R. Aziz and V. B. Ziccardi, "Telemedicine using smartphones for oral and maxillofacial surgery consultation, communication, and treatment planning," *Journal of Oral and Maxillofacial Surgery*, vol. 67, no. 11, pp. 2505 – 2509, 2009.

[13] E. R. Leavitt, S. Kessler, S. Pun, T. Gill, L. A. Escobedo, M. Cockburn, A. Sutton, and A. B. Crew, "Teledermatology as a tool to improve access to care for medically underserved populations: A retrospective descriptive study," *Journal of the American Academy of Dermatology*, vol. 75, no. 6, pp. 1259–1261, 2016.

[14] G. Burg, *Telemedicine and Teledermatology*. Current problems in dermatology, Karger, 2003.

[15] S.-H. Lee, S.-W. Um, and J.-S. Choi, *Color Correction System Using a Color Compensation Chart for the Images from Digital Camera*, pp. 258–269. Berlin, Heidelberg: Springer Berlin Heidelberg, 2006.

[16] M. J. M. Vasconcelos, L. Rosado, and M. Ferreira, *Principal Axes-Based Asymmetry Assessment Methodology for Skin Lesion Image Analysis*, pp. 21–31. Cham: Springer International Publishing, 2014.

[17] R. J. Friedman, D. S. Rigel, and A. W. Kopf, "Early detection of malignant melanoma: The role of physician examination and self-examination of the skin," *CA: A Cancer Journal for Clinicians*, vol. 35, no. 3, pp. 130–151, 1985.

[18] N. R. Abbasi, H. M. Shaw, D. S. Rigel, R. J. Friedman, W. H. McCarthy, I. Osman, A. W. Kopf, and D. Polsky, "Early diagnosis of cutaneous melanoma: revisiting the abcd criteria," *Jama*, vol. 292, no. 22, pp. 2771–2776, 2004.

[19] P. G. Cavalcanti, *Automated prescreening of melanocytic skin lesions using standard camera images*. PhD thesis, Rio Grande do Sul, Brasil, 2013.

[20] J. Grob and J. Bonerandi, "The 'ugly duckling'sign: identification of the common characteristics of nevi in an individual as a basis for melanoma screening," *Archives of dermatology*, vol. 134, no. 1, pp. 103–104, 1998.

[21] R. P. Braun, H. S. Rabinovitz, M. Oliviero, A. W. Kopf, and J.-H. Saurat, "Dermoscopy of pigmented skin lesions," *Journal of the American Academy of Dermatology*, vol. 52, no. 1, pp. 109 – 121, 2005.

[22] H. Pehamberger, A. Steiner, and K. Wolff, "In vivo epiluminescence microscopy of pigmented skin lesions. i. pattern analysis of pigmented skin lesions," *Journal of the American Academy of Dermatology*, vol. 17, no. 4, pp. 571 – 583, 1987.

[23] M. Vestergaard, P. Macaskill, P. Holt, and S. Menzies, "Dermoscopy compared with naked eye examination for the diagnosis of primary melanoma: a meta-analysis of studies performed in a clinical setting," *British Journal of Dermatology*, vol. 159, no. 3, pp. 669–676, 2008.

[24] R. P. Braun, M. Oliviero, I. Kolm, L. E. French, A. A. Marghoob, and H. Rabinovitz, "Dermoscopy: what's new?," *Clinics in Dermatology*, vol. 27, no. 1, pp. 26 – 34, 2009. Melanoma and Pigmented Lesions, Part 1.

[25] *Dermoscopy of pigmented skin lesions. An atlas based on the consensus net Meeting on dermoscopy (2000)*. Edra, 2001.

[26] G. Argenziano, H. Soyer, S. Chimenti, R. Talamini, R. Corona, F. Sera, M. Binder, L. Cerroni, G. D. Rosa, G. Ferrara, R. Hofmann-Wellenhof, M. Landthaler, S. W. Menzies, H. Pehamberger, D. Piccolo, H. S. Rabinovitz, R. Schiffner, S. Staibano, W. Stolz, I. Bartenjev, A. Blum, R. Braun, H. Cabo, P. Carli, V. D. Giorgi, M. G. Fleming, J. M. Grichnik, C. M. Grin, A. C. Halpern, R. Johr, B. Katz, R. O. Kenet, H. Kittler, J. Kreusch, J. Malvehy, G. Mazzocchetti, M. Oliviero, F. Özdemir, K. Peris, R. Perotti, A. Perusquia, M. A. Pizzichetta, S. Puig, B. Rao, P. Rubegni, T. Saida, M. Scalvenzi, S. Seidenari, I. Stanganelli, M. Tanaka, K. Westerhoff, I. H. Wolf, O. Braun-Falco, H. Kerl, T. Nishikawa, K. Wolff, and A. W. Kopf, "Dermoscopy of pigmented skin lesions: Results of a consensus meeting via the internet," *Journal of the American Academy of Dermatology*, vol. 48, no. 5, pp. 679 – 693, 2003.

[27] A. Sáez, B. Acha, and C. Serrano, *Pattern Analysis in Dermoscopic Images*, pp. 23–48. Berlin, Heidelberg: Springer Berlin Heidelberg, 2014.

[28] R. Garnavi, M. Aldeen, and J. Bailey, "Classification of melanoma lesions using wavelet-based texture analysis," in *2010 International Conference on Digital*

Image Computing: Techniques and Applications, pp. 75–81, 2010.

[29] E. Comission, "ehealth action plan 2012-2020: Innovative healthcare for the 21st century." `https://ec.europa.eu/digital-single-market/en/news/ehealth-action-plan-2012-2020-innovative-healthcare-21st-century`. Accessed: 2017-803.

[30] U. Leiter, T. Eigentler, and C. Garbe, *Epidemiology of Skin Cancer*, pp. 120–140. New York, NY: Springer New York, 2014.

[31] D. A. Perednia and N. A. Brown, "Teledermatology: one application of telemedicine.," *Bulletin of the Medical Library Association*, vol. 83, no. 1, pp. 42–47, 1995.

[32] J. D. Whited, "Teledermatology," *Medical Clinics of North America*, vol. 99, no. 6, pp. 1365 – 1379, 2015. Dermatology.

[33] Y. S. Levin and E. M. Warshaw, "Teledermatology: A review of reliability and accuracy of diagnosis and management," *Dermatologic Clinics*, vol. 27, no. 2, pp. 163–176.

[34] S. C, F. A, J. M, S. H, and W. JA, "Cost-effectiveness of store-and-forward teledermatology: A systematic review," *JAMA Dermatology*, vol. 152, no. 6, pp. 702–708, 2016.

[35] M. Campagna, F. Naka, and J. Lu, "Teledermatology: An updated overview of clinical applications and reimbursement policies," *International Journal of Women's Dermatology*, 2017.

[36] H. S. Pak, S. K. Datta, C. A. Triplett, J. H. Lindquist, S. C. Grambow, and J. D. Whited, "Cost minimization analysis of a store-and-forward teledermatology consult system," *TELEMEDICINE and e-HEALTH*, vol. 15, no. 2, pp. 160–165, 2009.

[37] S. M. Landow, A. Mateus, K. Korgavkar, D. Nightingale, and M. A. Weinstock, "Teledermatology: Key factors associated with reducing face-to-face dermatology visits," *Journal of the American Academy of Dermatology*, vol. 71, no. 3, pp. 570 – 576, 2014.

[38] M. Loane, S. Bloomer, R. Corbett, D. Eedy, N. Hicks, H. Lotery, C. Mathews, J. Paisley, K. Steele, and R. Wootton, "A comparison of real-time and store-and-forward teledermatology: a cost–benefit study," *British Journal of Dermatology*, vol. 143, no. 6, pp. 1241–1247, 2000.

[39] A. Fogel and K. Sarin, "Fogel al, sarin ky. a survey of direct-to-consumer teledermatology services available to us patients: Explosive growth, opportunities, and controversy. journal of telemedicine and telecare. 2016 jan 4. [epub ahead of print]," 2016.

[40] A. Badano, C. Revie, A. Casertano, W.-C. Cheng, P. Green, T. Kimpe, E. Krupinski, C. Sisson, S. Skrøvseth, D. Treanor, P. Boynton, D. Clunie, M. J. Flynn, T. Heki, S. Hewitt, H. Homma, A. Masia, T. Matsui, B. Nagy, M. Nishibori, J. Penczek, T. Schopf, Y. Yagi, and H. Yokoi, "Consistency and standardization of color in medical imaging: a consensus report," *Journal of Digital Imaging*, vol. 28, no. 1, pp. 41–52, 2015.

[41] R. C. Gonzalez and R. E. Woods, *Digital Image Processing*. Boston, MA, USA: Addison-Wesley Longman Publishing Co., Inc., 2nd ed., 2001.

[42] C. Poynton, "Poynton's color faq," *Electronic Preprint*, 1995.

[43] T. E. of Encyclopædia Britannica, "candela (cd)." `https://www.britannica.com/topic/candela`, 2011. Accessed: 2017-3-12.

[44] C. Poynton *Proceedings of the SMPTE Advanced Television and Electronic Imaging Conference*.

[45] M. Tkalcic and J. F. Tasic, "Colour spaces: perceptual, historical and applicational background," in *The IEEE Region 8 EUROCON 2003. Computer as a Tool.*, vol. 1, pp. 304–308 vol.1, 2003.

[46] I. Specification, "1: 2004-10 (profile version 4.2. 0.0)," *International Color Consortium*, 2004.

[47] W. Mokrzycki and M. Tatol, "Colour difference - a survey," *Machine Graphic & Vision*, vol. 8, 2012.

[48] C. I. de L'Éclairage, *International Lighting Vocabulary*. Vienna, Austria: Central Bureau of the Commission Internationale de L'Éclairage, 1987.

[49] S. McHugh, *Understanding Photography: Core Concepts and Techniques with Digital Image Capture*. Cambridge in Colour, 2016.

[50] D. Präkel, *The Visual Dictionary of Photography*. AVA Academia, Bloomsbury Academic, 2010.

[51] D. P. Curtin, *The textbook of digital photography*. Marblehead, Mass.: Short-Courses.com, 2011.

[52] D. Wueller, "Proposal for a standard procedure to test mobile phone cameras," *Proc. SPIE*, vol. 6069, pp. 60690P–60690P–13, 2006.

[53] C. S. McCamy, H. Marcus, J. Davidson, *et al.*, "A color-rendition chart," *J. App. Photog. Eng*, vol. 2, no. 3, pp. 95–99, 1976.

[54] Y. Yagi, "Color standardization and optimization in whole slide imaging," *Diagnostic pathology*, vol. 6, no. 1, p. S15, 2011.

[55] xRite Inc., "Colorchecker digital sg: X-rite photo and video," tech. rep., 4300 44th St SE, Grand Rapids Michigan 495 12 US, 2017.

[56] I. Engineering, "Image quality charts." `https://www.image-engineering.de/`, 2017. Accessed: 2017-3-22.

[57] Y. V. Haeghen, J. M. A. D. Naeyaert, I. Lemahieu, and W. Philips, "An imaging system with calibrated color image acquisition for use in dermatology," *IEEE transactions on medical imaging*, vol. 19, no. 7, pp. 722–730, 2000.

[58] S. H. Lee, S. W. Um, and J. S. Choi, "Design and implementation of color reproduction system for images captured by digital camera," in *2008 Digest of Technical Papers - International Conference on Consumer Electronics*, pp. 1–2, 2008.

[59] S.-H. Lee and J.-S. Choi, "Design and implementation of color correction system for images captured by digital camera," *IEEE Transactions on consumer electronics*, vol. 54, no. 2, 2008.

[60] J. Marguier, N. Bhatti, H. Baker, M. Harville, and S. Süsstrunk, "Color correction of uncalibrated images for the classification of human skin color," in *Proceedings of the 15th IS&T/SID Color Imaging Conference*, (Albuquerque, NM), pp. 331–335, 2007.

[61] P. Jackman, D.-W. Sun, and G. Elmasry, "Robust colour calibration of an imaging system using a colour space transform and advanced regression modelling," *Meat science*, vol. 91, no. 4, p. 402—407, 2012.

[62] R. Gong, Q. Wang, X. Shao, and J. Liu, "A color calibration method between different digital cameras," *Optik - International Journal for Light and Electron Optics*, vol. 127, no. 6, pp. 3281 – 3285, 2016.

[63] R. Charrière, M. Hébert, A. Trémeau, and N. Destouches, "Color calibration of an rgb camera mounted in front of a microscope with strong color distortion," *Appl. Opt.*, vol. 52, no. 21, pp. 5262–5271.

[64] A. Artusi and A. Wilkie, "Novel color printer characterization model," *Journal of electronic imaging*, vol. 12, no. 3, pp. 448–458, 2003.

[65] S. W. Oh and S. J. Kim, "Approaching the computational color constancy as a classification problem through deep learning," *Pattern Recognition*, vol. 61, pp. 405–416, 2017.

[66] V. Cheung, S. Westland, D. Connah, and C. Ripamonti, "A comparative study of the characterisation of colour cameras by means of neural networks and polynomial transforms," *Coloration technology*, vol. 120, no. 1, pp. 19–25, 2004.

[67] H. J. Chien, C. C. Chuang, C. Y. Chen, and R. Klette, "When to use what feature? sift, surf, orb, or a-kaze features for monocular visual odometry," in *2016 International Conference on Image and Vision Computing New Zealand (IVCNZ)*, pp. 1–6, 2016.

[68] H. Palus and A. Kordecki, "Automatic detection of colour charts in images," vol. 90, 2014.

[69] W. K. Pratt, "Digital image processing: Piks scientific inside/william k. pratt.–ny," 2007.

[70] W. Burger, M. J. Burge, M. J. Burge, and M. J. Burge, *Principles of digital image processing*. Springer, 2009.

[71] W. I. D. Mining, "Data mining: Concepts and techniques," *Morgan Kaufinann*, 2006.

[72] M. Hassaballah, A. A. Abdelmgeid, and H. A. Alshazly, "Image features detection, description and matching," in *Image Feature Detectors and Descriptors*, pp. 11–45, Springer, 2016.

[73] D. G. Lowe, "Distinctive image features from scale-invariant keypoints," *International journal of computer vision*, vol. 60, no. 2, pp. 91–110, 2004.

[74] H. Bay, A. Ess, T. Tuytelaars, and L. Van Gool, "Speeded-up robust features (surf)," *Computer vision and image understanding*, vol. 110, no. 3, pp. 346–359, 2008.

[75] Z. Pusztai and L. Hajder, "Quantitative comparison of feature matchers implemented in opencv3," 2016.

[76] P. F. Alcantarilla, A. Bartoli, and A. J. Davison, "Kaze features," in *European Conference on Computer Vision*, pp. 214–227, Springer, 2012.

[77] A. B. Pablo Alcantarilla (Georgia Institute of Technolog), Jesus Nuevo (TrueVision Solutions AU), "Fast explicit diffusion for accelerated features in nonlinear scale spaces," in *Proceedings of the British Machine Vision Conference*, BMVA Press, 2013.

[78] O. Andersson and S. Reyna Marquez, "A comparison of object detection algorithms using unmanipulated testing images: Comparing sift, kaze, akaze and orb," 2016.

[79] G. Bradski and A. Kaehler, *Learning OpenCV: Computer vision with the OpenCV library.* " O'Reilly Media, Inc.", 2008.

[80] E. J. Giorgianni and T. E. Madden, *Digital Color Management: Encoding Solutions.* Boston, MA, USA: Addison-Wesley Longman Publishing Co., Inc., 1998.

[81] M. Brill, "How the cie 1931 color-matching functions were derived from wright-guild data," vol. 23, 1998.

Appendices

A

Appendix I

A.1 Linear transformation from CIE RGB to CIE XYZ

The linear transformation from CIE RGB to a new system CIE XYZ is represented as follows [80, 81]:

$$\begin{bmatrix} X \\ Y \\ Z \end{bmatrix} = T \begin{bmatrix} R \\ G \\ B \end{bmatrix}, \begin{bmatrix} \bar{x}(\lambda) \\ \bar{y}(\lambda) \\ \bar{z}(\lambda) \end{bmatrix} = T \begin{bmatrix} \bar{r}(\lambda) \\ \bar{g}(\lambda) \\ \bar{b}(\lambda) \end{bmatrix} \tag{A.1}$$

where T is a 3 x 3 matrix:

$$T = \begin{bmatrix} b_{11} & b_{12} & b_{13} \\ b_{21} & b_{22} & b_{23} \\ b_{31} & b_{32} & b_{33} \end{bmatrix} \tag{A.2}$$

Finding the matrix T can be done by finding the coefficients a_{ij} such that [81]:

$$\begin{bmatrix} R \\ G \\ B \end{bmatrix} = \begin{bmatrix} a_{11} & a_{12} & a_{13} \\ a_{21} & a_{22} & a_{23} \\ a_{31} & a_{32} & a_{33} \end{bmatrix} \begin{bmatrix} X \\ Y \\ Z \end{bmatrix} = T^{-1} \begin{bmatrix} X \\ Y \\ Z \end{bmatrix} \tag{A.3}$$

In CIE RGB the unit coordinate vectors X, Y, Z are the vectors [81]:

$$\begin{bmatrix} R_x \\ G_x \\ B_x \end{bmatrix} = T^{-1} \begin{bmatrix} 1 \\ 0 \\ 0 \end{bmatrix} = \begin{bmatrix} a_{11} \\ a_{21} \\ a_{31} \end{bmatrix}$$

$$\begin{bmatrix} R_y \\ G_y \\ B_y \end{bmatrix} = T^{-1} \begin{bmatrix} 0 \\ 1 \\ 0 \end{bmatrix} = \begin{bmatrix} a_{12} \\ a_{22} \\ a_{32} \end{bmatrix} \tag{A.4}$$

$$\begin{bmatrix} R_z \\ G_z \\ B_z \end{bmatrix} = T^{-1} \begin{bmatrix} 0 \\ 0 \\ 1 \end{bmatrix} = \begin{bmatrix} a_{13} \\ a_{23} \\ a_{33} \end{bmatrix}$$

Once these vectors are defined, the transformation from CIE RGB to CIE XYZ is specified. Three linear equations are retrieved from A.4 [81]:

$$a_{11} + a_{12} + a_{13} = 1$$

$$a_{21} + a_{22} + a_{23} = 1 \tag{A.5}$$

$$a_{31} + a_{32} + a_{33} = 1$$

To complete the solution for all the nine values of a_{ij}, it will suffice to find six additional linear equations. This can be done by projecting RGB space into the chromacity plane and identifying the X, Y, Z coordinates unit vectors as cardinal points in this plane [81].

The transformation of tristimulus space (R, G, B) to chromaticity space (r,g) is a combination of two projective transformations in sequence as depicted in Figure A.1 . The first is a central projection of (R, G, B) to the (1, 1, 1) plane with focal point at the origin. The projected points lie on the plane R + G + B = 1, and are given

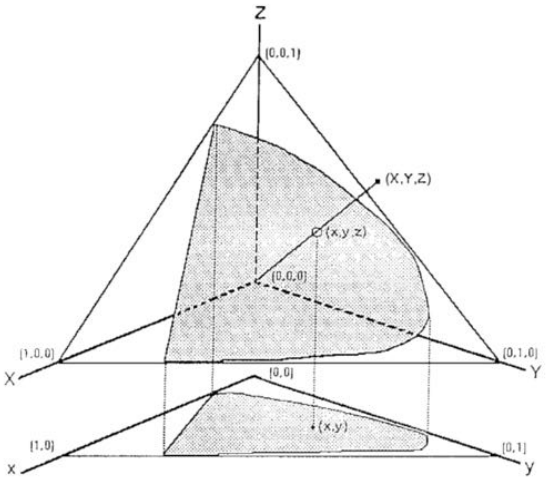

Figure A.1: Location of the chromacity plane in XYZ color space [81].

by the coordinates [81]:

$$r = \frac{R}{R+G+B}$$

$$g = \frac{G}{R+G+B} \tag{A.6}$$

$$b = \frac{B}{R+G+B}$$

Nonetheless, the points in the central projection are still in tristimulus coordinates. Yet, there is a constraint among them b = 1 - r – g, this two-dimensional representation is the aforementioned chromaticity diagram. Its coordinates are [81]:

$$r = \frac{R}{R+G+B}$$

$$g = \frac{G}{R+G+B} \tag{A.7}$$

Completing the solution for the a_{ij} using the relationships from the chromacity

diagram [81]:

$$r_X = \frac{a_{11}}{a_{11}+a_{21}+a_{31}}, g_X = \frac{a_{21}}{a_{11}+a_{21}+a_{31}}$$

$$r_Y = \frac{a_{12}}{a_{12}+a_{22}+a_{32}}, g_Y = \frac{a_{22}}{a_{12}+a_{22}+a_{32}} \tag{A.8}$$

$$r_Z = \frac{a_{13}}{a_{13}+a_{23}+a_{33}}, g_Z = \frac{a_{23}}{a_{13}+a_{23}+a_{33}}$$

Equations A.5 and A.8 comprise nine linear equations in the nine unknowns a_{ij}. These were the equations solved by the CIE to provide reference matrices for the conversion of CIE RGB to CIE XYZ [81].

A.2 Chromatic adaptation transformation

A chromatic adaptation matrix for a linear CAT is a combination of three separate conversions [46]:

1. conversion of source CIEXYZ tristimulus values to cone response values;
2. adjustment of the cone response values for an observer's chromatic adaptation;
3. conversion of the adjusted cone response tristimulus values back to CIEXYZ values.

The cone response values can be found through the matrix equation [46]:

$$\begin{bmatrix}\rho\\ \gamma\\ \beta\end{bmatrix} = \begin{bmatrix}0.8951 & 0.2664 & -0.1614\\ -0.7502 & 1.7135 & 0.0367\\ 0.0389 & -0.0685 & 1.0296\end{bmatrix}\begin{bmatrix}X\\ Y\\ Z\end{bmatrix} = M_{BFD}\begin{bmatrix}X\\ Y\\ Z\end{bmatrix} \tag{A.9}$$

where M_{BFD} represents the linear Bradford matrix. The chromatic adaptation (M_{adapt}) between two white points is calculated as follows:

$$M_{adapt} = M_{BFD}^{-1}\begin{bmatrix}\rho_{dst}/\rho_{src} & 0 & 0\\ 0 & \gamma_{dst}/\gamma_{src} & 0\\ 0 & 0 & \beta_{dst}/\beta_{src}\end{bmatrix} M_{BFD} \tag{A.10}$$

where:

$$\begin{bmatrix} \rho_{src} \\ \gamma_{src} \\ \beta_{src} \end{bmatrix} = M_{BFD} \begin{bmatrix} X_{WPsrc} \\ Y_{WPsrc} \\ Z_{WPsrc} \end{bmatrix} \tag{A.11}$$

$$\begin{bmatrix} \rho_{dst} \\ \gamma_{dst} \\ \beta_{dst} \end{bmatrix} = M_{BFD} \begin{bmatrix} X_{WPdst} \\ Y_{WPdst} \\ Z_{WPdst} \end{bmatrix} \tag{A.12}$$

$X_{WP_{dst}}$, $Y_{WP_{dst}}$ and $Z_{WP_{dst}}$ stand for the tristimulus values of the illuminant in the final destination viewing conditions and $X_{WP_{src}}$, $Y_{WP_{src}}$ and $Z_{WP_{src}}$ are the tristimulus values of the illuminant in the device actual viewing condition.

A.3 Transformations from CIE XYZ to CIE Luv and from CIE XYZ to CIE LAB

The transformation from CIE XYZ to CIE Luv is performed with the following equations [45]:

$$\begin{aligned} L^* &= 116 \left(\frac{Y}{Y_{WP}} \right)^{\frac{1}{3}} - 16 \\ u^* &= 13L^*(u' - u'_{WP}) \\ v^* &= 13L^*(v' - v'_{WP}) \end{aligned} \tag{A.13}$$

for $\frac{Y}{Y_{WP}} > 0.01$, otherwise the following L_* formula is used:

$$L^* = 903.3 \frac{Y}{Y_{WP}} \tag{A.14}$$

The constraints u', v', u'_{WP} and v'_{WP} are obtained from:

$$\begin{aligned} u' &= \frac{4X}{X + 15Y + 3Z} \\ u'_{WP} &= \frac{4X_{WP}}{X_{WP} + 15Y_{WP} + 3Z_{WP}} \\ v' &= \frac{9Y}{X + 15Y + 3Z} \\ v'_{WP} &= \frac{9Y_{WP}}{X_{WP} + 15Y_{WP} + 3Z_{WP}} \end{aligned} \tag{A.15}$$

As previously mentioned, the tristimulus values of X_{WP}, Y_{WP} and Z_{WP} are those of the white point. The transformation from CIE XYZ to CIE Lab is performed based on the following equations [45]:

$$\begin{aligned} L^* &= 116 \left(\frac{Y}{Y_{WP}} \right)^{\frac{1}{3}} - 16 \\ a^* &= 500 \left[\left(\frac{X}{X_{WP}} \right)^{\frac{1}{3}} - \left(\frac{Y}{Y_{WP}} \right)^{\frac{1}{3}} \right] \\ b^* &= 200 \left[\left(\frac{Y}{Y_{WP}} \right)^{\frac{1}{3}} - \left(\frac{Z}{Z_{WP}} \right)^{\frac{1}{3}} \right] \end{aligned} \tag{A.16}$$

B

Appendix II

B.1 ColorChecker Digital SG's colorimetric reference data

Table B.1: ColorChecker Digital SG's colorimetric reference data.

1	**L***	96.71	49.70	8.13	96.79	49.79	8.09	96.70	49.74	8.10	96.69	49.72	8.08	49.71	96.79
	a*	-0.62	0.12	0.15	-0.66	0.13	0.19	-0.66	0.14	0.19	-0.67	0.12	0.13	0.12	-0.67
	b*	2.06	0.68	-0.76	1.99	0.66	-0.69	1.97	0.68	-0.93	1.95	0.64	-0.81	0.62	1.97
2	**L***	8.05	33.02	19.65	84.00	32.77	63.88	45.84	38.29	51.36	68.71	85.68	23.03	42.52	49.78
	a*	0.17	52.00	20.42	-1.70	19.91	20.34	-3.74	-17.44	9.52	-35.41	10.75	33.95	63.55	0.12
	b*	-0.69	-10.30	-18.82	-8.37	22.33	19.93	-25.32	30.22	-26.98	-1.11	18.39	8.88	11.43	0.65
3	**L***	49.76	61.40	41.70	85.48	62.28	35.28	47.60	20.76	71.62	70.39	89.35	44.35	18.09	8.23
	a*	0.11	27.14	18.90	15.15	37.56	12.93	53.66	31.66	-24.77	19.37	-16.38	67.94	32.61	0.18
	b*	0.72	-18.42	-37.42	0.79	68.87	-51.17	22.15	-28.04	64.10	79.73	6.41	50.62	-5.90	-0.82
4	**L***	96.72	30.54	20.25	84.56	19.92	52.75	36.88	81.43	48.75	47.42	84.59	60.91	40.66	96.73
	a*	-0.63	50.39	0.26	-19.74	25.07	-44.12	65.72	2.41	57.24	-30.91	5.21	36.55	65.54	-0.67
	b*	2.06	-41.79	-36.44	-1.13	-61.05	38.68	41.63	88.98	-14.45	-32.27	-5.87	4.15	31.98	1.99
5	**L***	8.17	49.56	60.13	85.26	96.78	79.65	65.22	49.71	34.85	15.43	83.63	62.20	53.13	49.80
	a*	0.15	-13.90	-17.88	13.37	-0.66	-0.08	-0.27	0.12	-0.21	-0.24	-12.47	37.45	68.44	0.11
	b*	-0.65	-49.65	-32.08	7.95	2.01	0.62	0.16	0.69	0.73	-0.25	-8.89	18.18	49.57	0.67
6	**L***	49.68	60.62	19.75	84.38	8.07	30.32	39.55	60.04	75.36	88.85	70.60	63.33	82.08	8.18
	a*	0.14	-29.91	-17.79	-11.97	0.12	-0.10	-0.37	0.09	0.35	-0.59	-0.24	51.30	23.39	0.15
	b*	0.74	-27.54	-22.37	27.16	-0.93	0.22	-0.09	0.05	0.26	0.25	0.07	81.88	87.24	-0.84
7	**L***	96.60	20.13	60.43	62.35	77.37	63.46	44.49	67.60	45.14	64.00	45.14	73.74	82.50	96.73
	a*	-0.62	-24.81	-5.12	29.94	20.28	13.53	16.06	14.47	26.38	25.0	-0.04	-11.45	5.29	-0.65
	b*	2.11	-7.50	-32.79	36.89	24.27	26.37	26.79	17.12	41.24	27.14	0.86	85.07	96.68	2.01
8	**L***	7.99	60.32	50.46	64.17	74.01	64.44	64.97	64.75	36.20	66.65	20.33	62.35	71.90	49.75
	a*	0.21	-40.29	-47.90	21.34	29.00	14.31	15.89	17.30	16.70	22.21	0.40	1.96	-17.32	0.13
	b*	-0.75	-13.25	-11.56	19.36	25.80	17.63	16.79	18.88	27.06	28.81	-0.21	57.52	77.72	0.67
9	**L***	49.67	19.62	60.53	50.48	20.33	60.05	60.77	51.26	61.65	62.05	62.33	72.77	21.95	8.11
	a*	0.15	1.77	-40.75	-53.21	-23.98	-44.00	-30.19	-50.65	-54.33	16.45	-14.54	-29.09	13.41	0.15
	b*	0.73	11.99	19.37	12.65	7.20	7.27	40.76	43.80	46.18	51.74	54.58	71.26	16.36	-0.90
10	**L***	96.51	49.68	8.09	96.57	49.72	8.08	96.71	49.76	7.97	96.71	49.74	8.13	49.74	96.55
	a*	-0.63	0.15	0.19	-0.64	0.14	0.18	-0.64	0.14	0.14	-0.64	0.14	0.15	0.12	-0.64
	b*	2.11	0.78	-0.69	2.00	0.71	-0.78	2.01	0.71	-0.80	2.02	0.69	-0.86	0.69	2.02
		A	B	C	D	E	F	G	H	I	J	K	L	M	N

C

Appendix III

C.1 Skin lesions acquired in Experiment 1

Table C.1: Lesion 03.

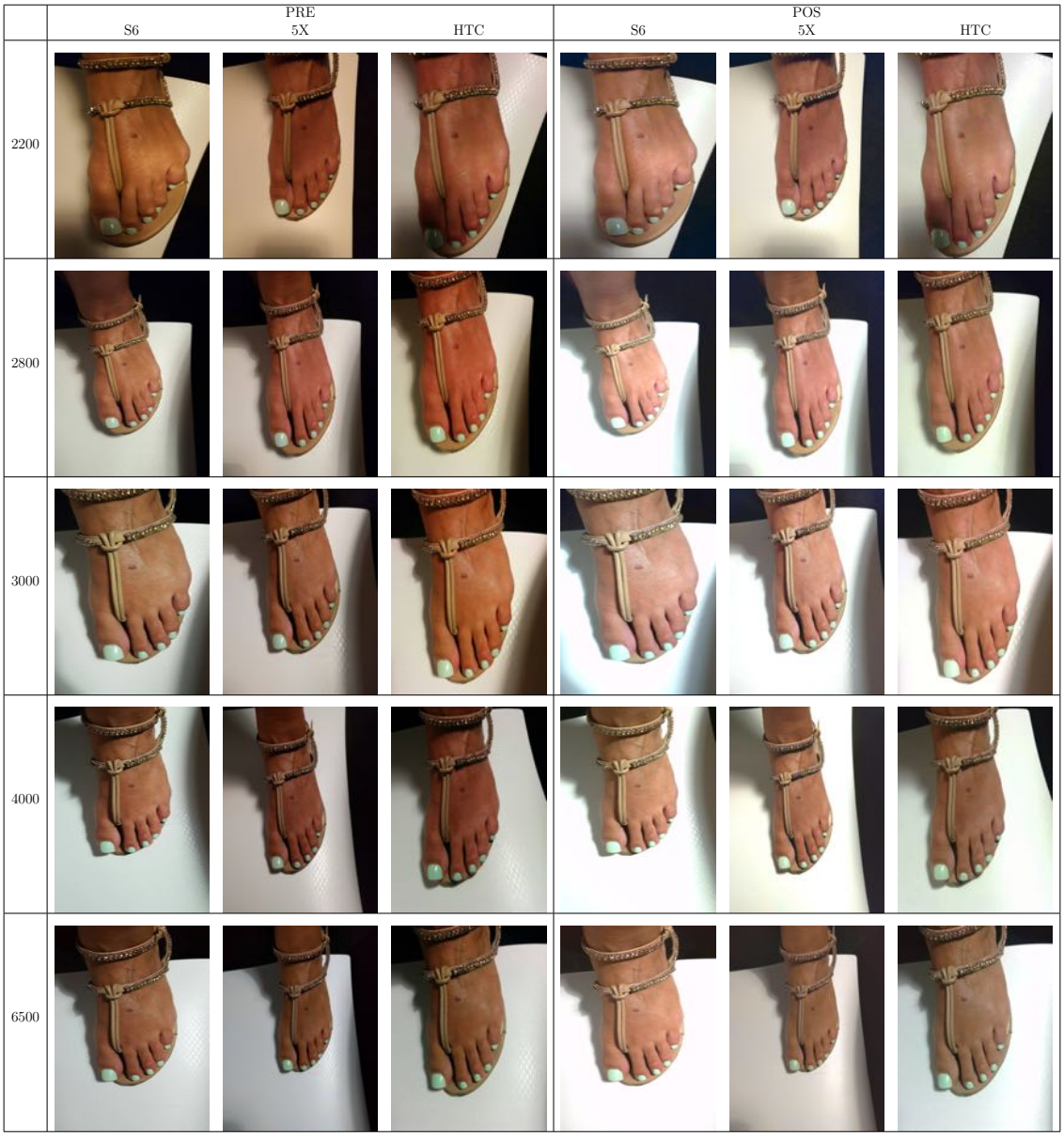

Table C.2: Evaluation of Lesion 03 in Situation 3.

		PRE	POS
Lesion	$\bar{L} \pm \sigma_L$	49.28±3.51	78.22±2.26
	$\bar{a} \pm \sigma_a$	144.96±1.12	144.39±0.66
	$\bar{b} \pm \sigma_b$	143.76±1.08	142.00±0.73
Skin	$\bar{L} \pm \sigma_L$	110.86±7.29	159.50±3.45
	$\bar{a} \pm \sigma_a$	152.07±1.65	147.43±1.55
	$\bar{b} \pm \sigma_b$	157.06±1.86	50.59±0.65

Table C.3: Lesion 04.

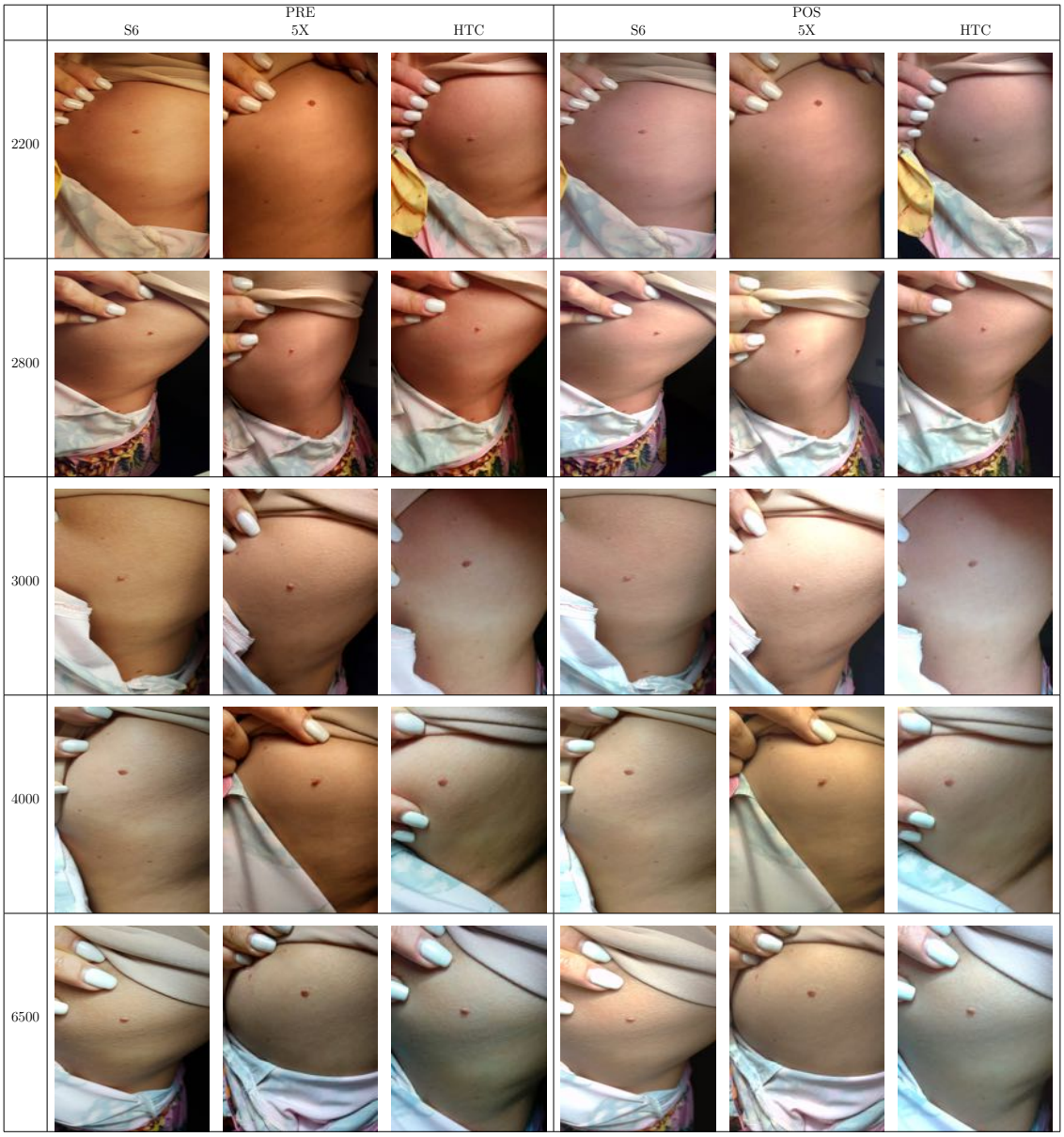

Table C.4: Evaluation of Lesion 04 in Situation 3.

		PRE	POS
Lesion	$\bar{L} \pm \sigma_L$	83,38±3,41	98,30±1,99
	$\bar{a} \pm \sigma_a$	147,20±1,61	142,31±1,20
	$\bar{b} \pm \sigma_b$	148,25±1,49	140,80±1,14
Skin	$\bar{L} \pm \sigma_L$	160,36±4,26	181,90±1,74
	$\bar{a} \pm \sigma_a$	141,07±2,46	138,53±1,72
	$\bar{b} \pm \sigma_b$	151,83±2,55	143,86±1,92

Table C.5: Lesion 05.

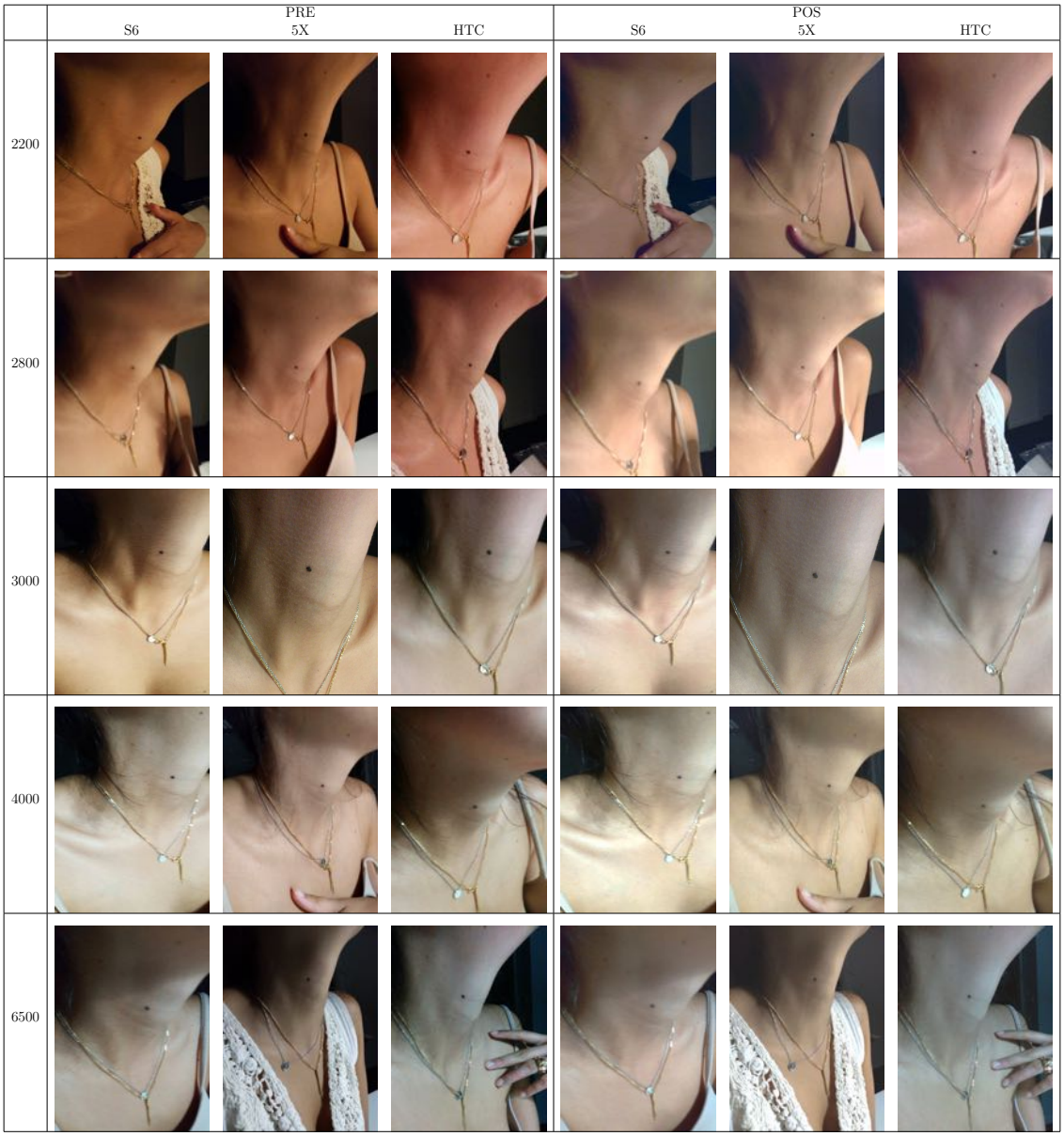

Table C.6: Evaluation of Lesion 05 in Situation 3.

		PRE	POS
Lesion	$\bar{L} \pm \sigma_L$	41,02±4,44	71,19±2,53
	$\bar{a} \pm \sigma_a$	134,62±1,55	132,42±1,17
	$\bar{b} \pm \sigma_b$	134,83±1,70	132,23±1,14
Skin	$\bar{L} \pm \sigma_L$	145,10±4,26	152,11±3,73
	$\bar{a} \pm \sigma_a$	138,05±2,46	134,24±1,14
	$\bar{b} \pm \sigma_b$	145,53±2,55	139,01±1,32

Table C.7: Lesion 06.

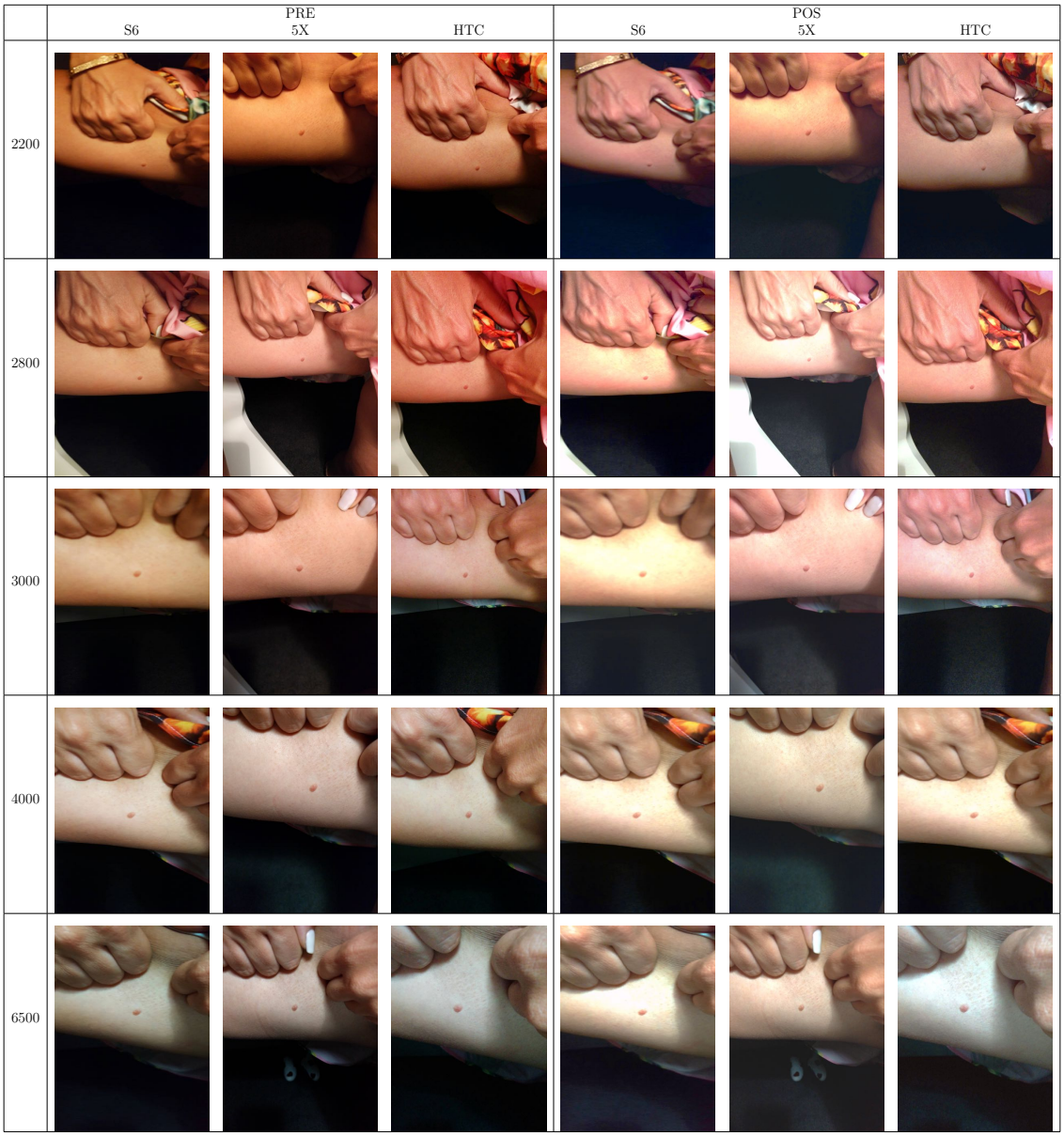

Table C.8: Evaluation of Lesion 06 in Situation 3.

		PRE	POS
Lesion	$\bar{L} \pm \sigma_L$	107,09±3,41	127,24±4,86
	$\bar{a} \pm \sigma_a$	146,28±1,94	144,92±1,6
	$\bar{b} \pm \sigma_b$	146,96±2,13	141,91±1,19
Skin	$\bar{L} \pm \sigma_L$	171,31±3,35	195,64±5,09
	$\bar{a} \pm \sigma_a$	142,04±2,71	138,52±2,12
	$\bar{b} \pm \sigma_b$	149,17±3,26	143,64±1,69

Table C.9: Lesion 07.

Table C.10: Evaluation of Lesion 07 in Situation 3.

		PRE	POS
Lesion	$\bar{L} \pm \sigma_L$	78,98±4,6	98,63±3,27
	$\bar{a} \pm \sigma_a$	143,31±1,71	139,44±1,05
	$\bar{b} \pm \sigma_b$	147,14±1,76	141,56±1,22
Skin	$\bar{L} \pm \sigma_L$	155,99±7,18	180±6,05
	$\bar{a} \pm \sigma_a$	142,28±2,43	139,39±1,96
	$\bar{b} \pm \sigma_b$	153,77±3,02	147,96±1,61

Table C.11: Lesion 08.

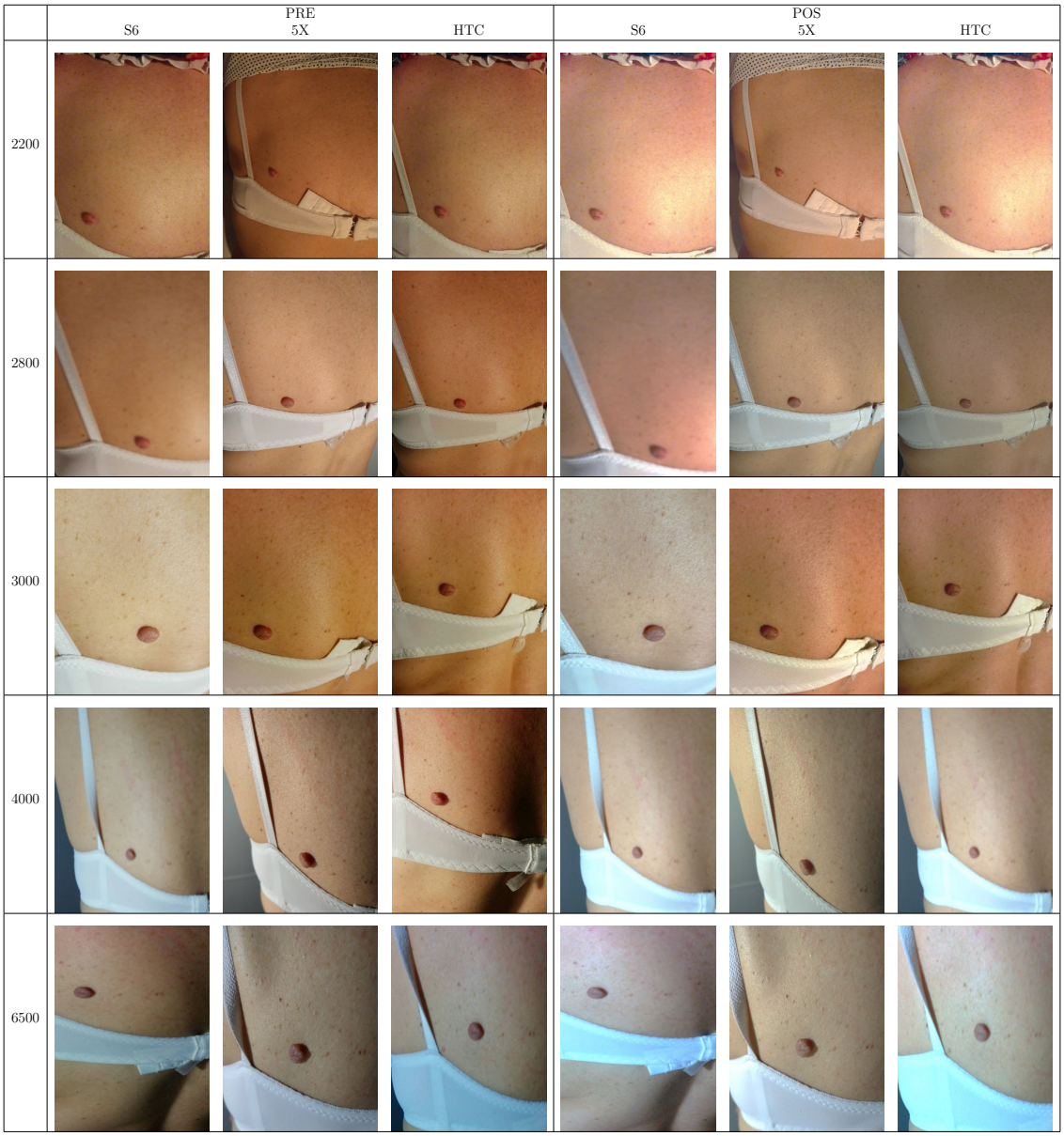

Table C.12: Evaluation of Lesion 08 in Situation 3.

		PRE	POS
Lesion	$\bar{L} \pm \sigma_L$	65,74±4,51	83,28±4,32
	$\bar{a} \pm \sigma_a$	144,25±1,35	140,06±1,1
	$\bar{b} \pm \sigma_b$	143,45±1,57	138,73±1,36
Skin	$\bar{L} \pm \sigma_L$	133,59±6,09	152,82±3,89
	$\bar{a} \pm \sigma_a$	139,12±1,84	136,39±1,62
	$\bar{b} \pm \sigma_b$	152,16±2,4	145,01±2

Table C.13: Lesion 09.

Table C.14: Evaluation of Lesion 09 in Situation 3.

		PRE	POS
Lesion	$\bar{L} \pm \sigma_L$	74,22±3,61	88,55±3,51
	$\bar{a} \pm \sigma_a$	146,47±1,45	142,28±1,2
	$\bar{b} \pm \sigma_b$	147,57±2,25	144,82±2,24
Skin	$\bar{L} \pm \sigma_L$	136,75±4,81	149,2±4,01
	$\bar{a} \pm \sigma_a$	138,62±2,02	134,96±1,78
	$\bar{b} \pm \sigma_b$	151,88±3,47	143,44±2,84

Table C.15: Lesion 09.

Table C.16: Evaluation of Lesion 10 in Situation 3.

		PRE	POS
Lesion	$\bar{L} \pm \sigma_L$	63,2±3,77	85,55±3,11
	$\bar{a} \pm \sigma_a$	144,29±1,38	141,34±1,26
	$\bar{b} \pm \sigma_b$	146,13±1,93	142,23±1,48
Skin	$\bar{L} \pm \sigma_L$	161,09±5,33	186,31±4,77
	$\bar{a} \pm \sigma_a$	137,53±2,07	136,69±1,9
	$\bar{b} \pm \sigma_b$	152,59±3,19	149,17±2,27

D

Appendix IV

D.1 Skin Lesions acquired in Experiment 2

Table D.1: Lesion 13.

	S6	5X	HTC
PRE			
POS			

Table D.2: Evaluation of Lesion 13 in Situation 1.

		PRE	POS
Lesion	$\bar{L} \pm \sigma_L$	74,28±12,78	93,42±10,42
	$\bar{a} \pm \sigma_a$	144,64±0,98	139,95±0,95
	$\bar{b} \pm \sigma_b$	152,1±0,88	144,13±0,52
Skin	$\bar{L} \pm \sigma_L$	119,12±13,2	163,13±8,02
	$\bar{a} \pm \sigma_a$	137,04±1,45	135,99±1,24
	$\bar{b} \pm \sigma_b$	148,99±3,19	143,67±2,87

Table D.3: Lesion 14.

	S6	5X	HTC
PRE			
POS		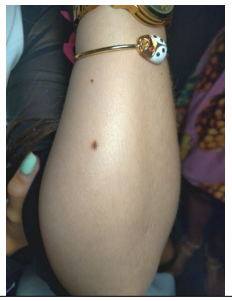	

Table D.4: Evaluation of lesion 14 in Situation 1.

		PRE	POS
Lesion	$\bar{L} \pm \sigma_L$	69,47±12,73	82,35±10,24
	$\bar{a} \pm \sigma_a$	140,05±1,48	135,27±0,26
	$\bar{b} \pm \sigma_b$	143,64±4,76	138,77±0,53
Skin	$\bar{L} \pm \sigma_L$	119,12±9,31	192,86±8,52
	$\bar{a} \pm \sigma_a$	137,04±2,37	128,92±0,72
	$\bar{b} \pm \sigma_b$	148,99±2,49	143,8±1,72

Table D.5: Lesion 15.

	S6	5X	HTC
PRE	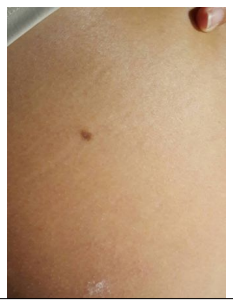	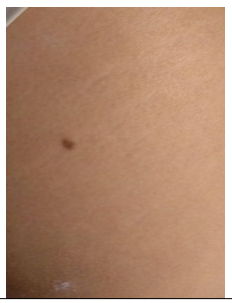	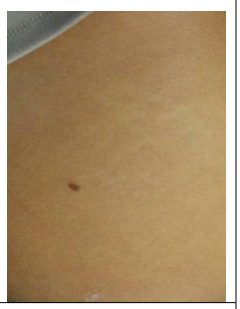
POS	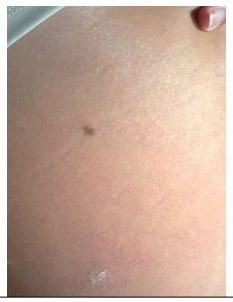	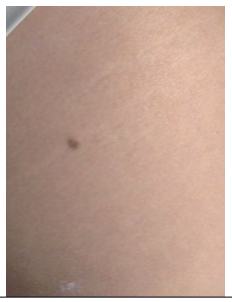	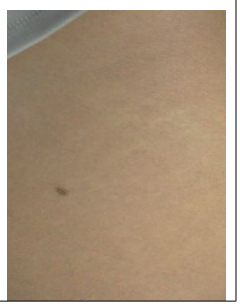

Table D.6: Evaluation of Lesion 15 in Situation 1.

		PRE	POS
Lesion	$\bar{L} \pm \sigma_L$	69,49±4,28	82,49±0,85
	$\bar{a} \pm \sigma_a$	138,64±1,28	134,32±1,08
	$\bar{b} \pm \sigma_b$	146,34±1,05	137,59±0,87
Skin	$\bar{L} \pm \sigma_L$	119,12±7,74	187,08±7,38
	$\bar{a} \pm \sigma_a$	137,04±2,22	136,72±1,5
	$\bar{b} \pm \sigma_b$	148,99±2,31	145,1±1,88

Table D.7: Lesion 16.

	S6	5X	HTC
PRE			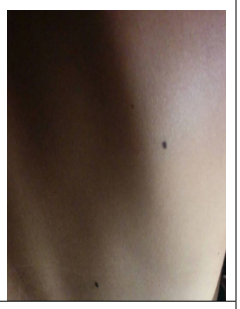
POS		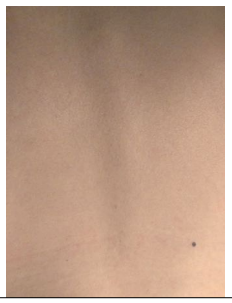	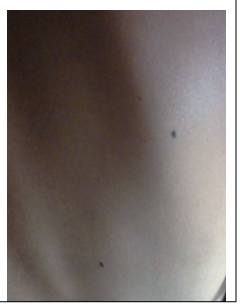

Table D.8: Evaluation of Lesion 16 in Situation 1.

		PRE	POS
Lesion	$\bar{L} \pm \sigma_L$	55,5±16,93	86,36±14,07
	$\bar{a} \pm \sigma_a$	134,12±2,8	132,03±1,75
	$\bar{b} \pm \sigma_b$	138,13±3,13	133,29±1,42
Skin	$\bar{L} \pm \sigma_L$	119,12±5,08	144,46±3,89
	$\bar{a} \pm \sigma_a$	135,64±2,97	133,47±2,73
	$\bar{b} \pm \sigma_b$	148,99±6,06	139,08±4,63

Table D.9: Lesion 17.

	S6	5X	HTC
PRE	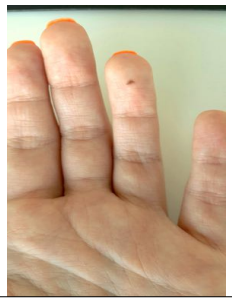		
POS	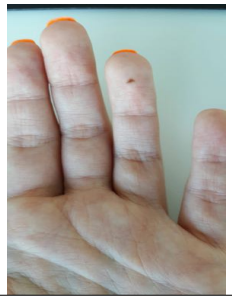	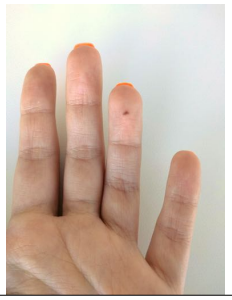	

Table D.10: Evaluation of Lesion 17 in Situation 1.

		PRE	POS
Lesion	$\bar{L} \pm \sigma_L$	75,29±12,65	87,98±3,63
	$\bar{a} \pm \sigma_a$	141,4±2,55	141,6±2,14
	$\bar{b} \pm \sigma_b$	142,59±6,54	136,4±2,96
Skin	$\bar{L} \pm \sigma_L$	119,12±6,77	169,18±4,86
	$\bar{a} \pm \sigma_a$	140,24±2,83	135,69±2,37
	$\bar{b} \pm \sigma_b$	148,99±7,95	141,98±6,94

Table D.11: Lesion 18.

	S6	5X	HTC
PRE	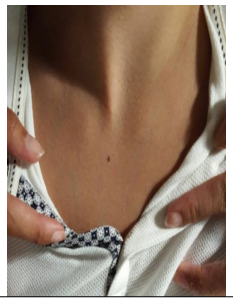	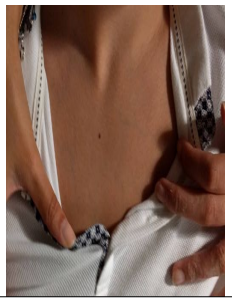	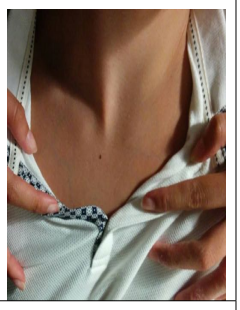
POS	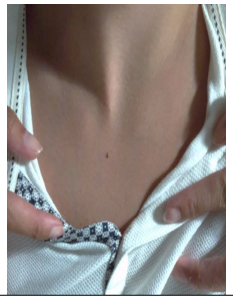	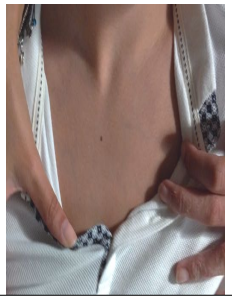	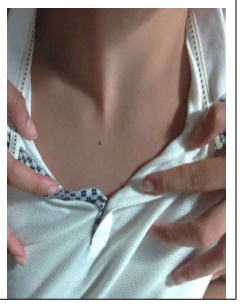

Table D.12: Evaluation of Lesion 18 in Situation 1.

		PRE	POS
Lesion	$\bar{L} \pm \sigma_L$	58,82±2,73	91,15±1,84
	$\bar{a} \pm \sigma_a$	144,17±0,96	137,55±0,96
	$b \pm \sigma_b$	145,18±0,16	144,82±0,54
Skin	$\bar{L} \pm \sigma_L$	119,12±5,49	135,61±2,71
	$\bar{a} \pm \sigma_a$	139,61±1,55	135,25±1,21
	$\bar{b} \pm \sigma_b$	148,99±0,58	145,18±1,23

Table D.13: Lesion 19.

	S6	5X	HTC
PRE			
POS			

Table D.14: Evaluation of Lesion 19 in Situation 1.

		PRE	POS
Lesion	$\bar{L} \pm \sigma_L$	95,99±6,68	123,66±4,65
	$\bar{a} \pm \sigma_a$	155,17±3,84	149,38±1,91
	$\bar{b} \pm \sigma_b$	147,77±3,65	144,77±1,35
Skin	$\bar{L} \pm \sigma_L$	119,12±6,81	211,2±4,31
	$\bar{a} \pm \sigma_a$	138,27±2,97	131,5±2,23
	$\bar{b} \pm \sigma_b$	148,99±4,13	146,91±3,34

Table D.15: Lesion 20.

	S6	5X	HTC
PRE			
POS			

Table D.16: Evaluation of Lesion 20 in Situation 1.

		PRE	POS
Lesion	$\bar{L} \pm \sigma_L$	61,13±2,59	74,17±2,1
	$\bar{a} \pm \sigma_a$	140,44±1,18	136,76±2,22
	$\bar{b} \pm \sigma_b$	142,07±2,17	135,64±2,33
Skin	$\bar{L} \pm \sigma_L$	191,83±6,44	210,54±4,07
	$\bar{a} \pm \sigma_a$	134,02±2,69	133,55±2,77
	$\bar{b} \pm \sigma_b$	145,52±5,16	139,13±4,48